Development and Characterization of Advanced Mid-Infrared Solid State Lasers

by

Hamit Kalaycıoğlu

A Thesis Submitted to the
Graduate School of Sciences and Engineering
in Partial Fulfillment of the Requirements for
the Degree of

Doctor of Philosophy
in
Electrical and Electronics Engineering

Koç University

September 2008

Koç University

Graduate School of Sciences and Engineering

This is to certify that I have examined this copy of a doctor of philosophy thesis by

Hamit Kalaycıoğlu

and have found that it is complete and satisfactory in all respects,
and that any and all revisions required by the final
examining committee have been made.

Committee Members:

_____

Alphan Sennaroğlu, Ph. D. (Advisor)

_____

Alper Demir, Ph. D.

_____

Alper Kiraz, Ph. D.

_____

Hakan Ürey, Ph. D.

_____

Özgür Müstecaplıoğlu, Ph. D.

Date: _____

ABSTRACT

This thesis investigates the experimental development of advanced solid-state lasers operating in the 2-μm region which have potential applications in medical surgery, remote sensing, and pumping of other mid-infrared solid-state lasers. In particular, lasing characteristics and spectroscopic properties of thulium-doped crystals and glasses in the near- and mid-infrared have been studied.

The first part of the thesis focuses on two experiments aimed at improving the continuous-wave (cw) operation of the thulium-doped $YAlO_3$ (Tm:YAP or Tm:YAlO) lasers. In the first experiment, the effect of doping (thulium or Tm^{3+}) concentration on diode-end-pumped laser operation was investigated. Three crystals with different Tm^{3+} concentrations of 1.5, 3 and 4 % were tested and best power efficiency was obtained with the 1.5% Tm:YAP crystal. Main conclusion of this work is that the cross relaxation effect, which enhances two-micron laser emission and weakens the competing 1.6-micron emission, is already effective with 1.5 % doping level based on the fluorescence data and rate equation analysis. In the second experiment, low-threshold operation of a cw Tm:YAP laser was experimentally demonstrated under Ti:sapphire pumping. In the experiments, a 4% Tm:YAP crystal was used inside a resonator with tight focusing geometry and lasing threshold powers as low as 10 mW have been obtained when double pumping was employed. As an application of the cw Tm:YAP laser, fiber-coupled version of the diode-pumped system was further built on a mobile platform and used in collaboration with a biomedical group from Bogazici University to evaluate its potential in tissue welding. The preliminary results investigating the interaction of laser radiation with tissues indicate that lower intensities (around 15 W/cm^2) are suitable for welding while higher intensities lead to coagulation and ablation.

Next, spectroscopic studies of two thulium-doped hosts were performed to investigate their lasing potential in the 2-μm region. These were Tm^{3+}:LuAG, a laser-active thulium-

doped garnet and Tm_2O_3:(0.85)TeO_2-(0.15)WO_3, a thulium-doped telluride-based glass which was prepared at İstanbul Technical University. For the Tm^{3+}:LuAG crystal, it was observed that the 1470-nm ($^3H_4 \rightarrow {}^3F_4$) emission vanished for 5% Tm^{3+} concentration due to cross relaxation while its strength was 60% of the 1800-nm ($^3F_4 \rightarrow {}^3H_6$) emission for the 0.5% Tm^{3+} concentration. We determined an emission cross section of 1.2±0.2 x 10^{-21} cm^2 at 2023 nm, the free running wavelength for this crystal. For the Tm_2O_3:(0.85)TeO_2-(0.15)WO3 glass, the fluorescence spectra of the 0.25 mol% and 1.0 mol% samples and the calculated emission cross sections (3.73 ± 0.1 x 10^{-21} cm^2 at 1460 nm and 6.57 ± 0.07 x 10^{-21} cm^2 at 1808 nm) indicate that this glass is a potentially important candidate for mid-infrared emission systems, with the 0.25 mol% Tm_2O_3 doping concentration being suitable for fiber-optic amplifiers operating around 1.5 μm and 1.0 mol% suitable for laser systems near 2.0 μm. However, to date, lasing trials in thulium-doped samples have not been successful possibly due to excessive passive losses or reabsorption in these samples.

To further test the lasing potential of the TeO_2-WO_3 glass as a laser host, we experimented with neodymium-doped samples and successfully demonstrated lasing at 1065 nm. This was the first demonstration of lasing in this novel telluride glass host. By using the 0.5 mol% sample, we obtained 11 μJ of output energy with a slope efficiency of 12% by using 114 μJ of pump energy. Hence, our studies have shown that TeO_2-WO_3 is a new, telluride-based laser glass host which can be used in the development of efficient bulk glass or fiber lasers in the infrared.

ÖZET

Bu tez 2 μm dalga boyu civarında çalışan ileri düzeyli katıhal lazerlerinin deneysel olarak geliştirilmesi amacı ile yapılan araştırma çalışmalarını içermektedir. Bu lazerlerin önemi, cerrahi, mesafe ölçümleri, atmosferik görüntüleme, ve orta kızılaltı dalgaboylarında çalışan lazer ve optik parametrik osilatörlerin pompalanmasını kapsayan birçok uygulamalarının bulunmasından ileri gelmektedir. Tez çalışmaları, özellikle, yakın ve orta kızılaltı bölgede ışınım yayan tulyum katkılı kristal ve cam lazerlerinin geliştirilmesi ve incelenmesi, ve tulyum katkılı kristal ve camların spektroskopilerinin incelenmesi üzerine yoğunlaşmıştır.

Tezin ilk kısmı sürekli-dalga tulyum katkılı $YAlO_3$ (Tm:YAP veya Tm:YAlO) lazerinin geliştirilmesi amaçlı iki deneysel çalışma üzerine odaklanmıştır. İlk çalışmada kristal içersindeki tulyum iyon yoğunluğunun sürekli-dalga diyod pompalı lazer performası üzerindeki etkisi tetkik edilmiştir. Bu amaçla %1.5, %3, ve %4 oranında tulyum katkılı üç değişik YAP kristali kullanılmış ve en iyi verim %1.5 katkılı örnek ile elde edilmiştir. Bu çalışmanın en belirgin sonucu iki-mikron dalgaboyundaki lazer verimini arttıran çapraz sönüm etkisinin %1.5 katkılı örnekte bile etkili olduğunun tespitidir. İkinci çalışmada, düşük pompa eşik gücüyle çalışan ve Ti:safir lazeri ile pompalanan sürekli-dalga Tm:YAP lazeri geliştirilmiştir. Deneylerde, %4 tulyum katkılı YAP kristali ve sıkı odaklama içeren optik kovuk tasarımı ile çift pompalama uygulanarak 10 mW pompa eşik gücü elde edilmiştir. Ayrıca, diyod pompalı sürekli dalga Tm:YAP lazeri, Boğaziçi Üniversitesi biomedikal bölümünden bir grup ile ortak proje kapsamında, lazer doku kaynağı potansiyelini tespit etmek hedefi ile, hareket ettirilebilir bir platform üzerine kurulu ve optik lif çıkışlı bir yapıya dönüştürülmüştür. Bu proje kapsamında lazer ışınımının dokularla etkileşimini inceleyen deneylerin ön sonuçları, test edilen ışınım yoğunluklarının düşük (15 W/cm^2 civarındaki) değerlerinin doku kaynağı için, daha yüksek değerlerinin ise doku yakma ve buharlaştırma uygulamaları için uygun olduğunu göstermektedir.

Daha sonraki çalışmalarda tulyum katkılı iki farklı malzemenin 2 μm dalga boyu civarında lazer ışınımı yayma potansiyeli spektroskopik inceleme yöntemi ile araştırılmıştır. Bu malzemeler bilinen bir lazer kristali olan Tm^{3+}:LuAG ve tulyum katkılı telür bazlı Tm_2O_3:(0.85)TeO_2-(0.15)WO_3 camıdır. Cam örnekleri İstanbul Teknik Üniversitesinde yerel imkanlarla üretilmiş olup bu açıdan özel önem taşımaktadırlar. Yapılan ilk çalışmada, Tm^{3+}:LuAG kristalinde, 1470-nm merkezli ($^3H_4 \rightarrow {}^3F_4$) ışıma bandının, %5 Tm^{3+} katkılı örnekte çapraz sönüm mekanizması sonucunda tamamen yok olduğu, halbuki %0.5 katkılı örnekte 1800-nm merkezli ($^3F_4 \rightarrow {}^3H_6$) ışıma bandının %60'ı büyüklüğünde olduğu gözlenmiştir. Bu çalışmada ayrıca Tm^{3+}:LuAG kristalinin serbest lazer çalışma dalgaboyu olan 2023 nm'deki ışınım ara kesiti 1.2±0.2 x 10^{-21} cm^2 olarak belirlenmiştir. İkinci çalışmada ise Tm_2O_3:(0.85)TeO_2-(0.15)WO_3 camının, ışınım tayflarına ve hesaplanan ışınım ara kesitlerine (1460 nm'de 3.73 ± 0.1 x 10^{-21} cm^2 ve 1808 nm'de 6.57 ± 0.07 x 10^{-21} cm^2) dayanarak, 0.25 mol% Tm_2O_3 katkı oranı ile 1.5 μm civarında çalışan fiber-optik yükselticiler, 1.0 mol% Tm_2O_3 katkı oranı ile ise de 2.0 μm civarında çalışan lazer sistemleri için güçlü bir aday olma potansiyeli taşıdığı sonucuna varılmıştır. Ancak, bugüne değin yapılmış olan denemelerde tulyum katkılı cam örneklerden lazer ışınımı elde edilememiştir. Bunun sebebinin örneklerdeki pasif kayıp seviyesinin yüksek olması muhtemeldir.

Tulyum katkılı örnekleri ile lazer denemelerinin başarısız olması üzerine, TeO_2-WO_3 camının lazer ışınım potansiyeli neodymium katkılanarak ölçülmek istenmiş ve neodymium katkılı örnekler ile 1065 nm'de lazer ışınımı elde edilmiştir. Böylece özgün bir telür bazlı camdan (Nd_2O_3:(0.8)TeO_2-(0.2)WO_3) lazer ışınımı ilk kez elde edilmiştir. Deneylerde 0.5 mol% katkılı bir örnek 114 μJ pompa enerjisi ile uyarılarak %12 verim eğrisi ve 11 μJ çıkış enerjisi elde edilmiştir. Sonuç olarak çalışmalarımız TeO_2-WO_3 camının kütle ve lif yapısında verimli cam lazerler geliştirmeye elverişli olduğunu ortaya koymuştur.

ACKNOWLEDGEMENTS

First of all, I would like to thank my advisor Dr. Alphan Sennaroğlu for valuable supervision and support during my Ph. D. study and for giving me the opportunity to work at Laser Research Laboratory. Then, I like to express my appreciation for the technical support of Adnan Kurt with the experimental equipment and his willingness to be available for help whenever I looked for him throughout my research work. I also want to thank him for his friendship and support, especially in some hard times. Next, I want to mention Ümit Demirbaş and Hüseyin Çankaya who has been friendly and helpful since my first day in the laboratory. I have benefited a lot from technical discussions with them and their support. Next, I wish to express my appreciation for the friendly, sincere and respectful attitude of my coworkers Reyhane Kılcı, Natali Çizmeciyan, Ahmet Koray Özdamar and Serhat Tozburun.

I like to thank Dr. Alper Demir, Dr. Alper Kiraz, Dr. Hakan Ürey and Dr. Özgür Müstecaplıoğlu for taking place in my thesis committee and for their support throughout my study at Koç University.

I would like thank Koç University for making such a research facilty as the Laser Research Laboratory available and TÜBİTAK for supporting research activities. I would like to thank İTÜ for the research facilities that have been used in some of the research work included in the thesis.

Last, but not least of all, I wish to express my gratefulness to my wife and my parents who supported me all the way during my quest for a Ph. D. degree. Especially, I want to mention my wife's sacrificial efforts in taking meticulous care of our two boys who were born during my Ph. D. study so that my research work would not be held back.

TABLE OF CONTENTS

LIST OF TABLES

LIST OF FIGURES

NOMENCLATURE

g	laser gain
σ_L	emission cross section
ΔN	population inversion
ΔN_{th}	threshold population inversion
n_2	population of active ions in the upper laser level
n_1	population of active ions in the lower laser level,
g_1, g_2	degeneracy coefficients
I	intensity
l	length of the gain medium
α	differential loss coefficient
R_1, R_2	mirror reflectivities inside a laser cavity
P_{th}	threshold pump power
v_p	frequency of the pump radiation
v_L	lasing frequency
w_L	laser mode waist (spot) size
w_p	pump beam waist (spot) size
T	output coupler transmission
L	round-trip passive cavity loss
N	doping (active ion) coefficient
τ	fluorescence lifetime
τ_r	radiative lifetime
τ_n	noradiative lifetime
η_a	fraction of pump power absorbed by the gain medium
α_p	absorption coefficient at pump wavelength

σ_a	absorption cross section
η_s	slope efficiency
$A(i,j)$	spontaneous emission (radiative transition or decay)rate (probability) from excited state i to terminal level j
$W(i,j)$	nonradiative transition rate from excited state i to terminal level j
β_{ij}	branching ratio
η	luminescence quantum efficiency
J	total angular momentum value
f_{ai}	fraction of the population of a multiplet a residing in a Stark level i
E_{ai}	energy of level i inside multiplet a
Z_a	partition for the multiplet a
k	Boltzman constant
f_2	fraction of the manifold population that occupy the upper laser level
f_1	fraction of the manifold population that occupy the lower laser level
F	fractional inversion
R_p	pumping rate
w_{ij}	total decay rate from the i^{th} to the j^{th} manifold
w_{ij}^{nr}	nonradiative decay rate from the i^{th} to the j^{th} manifold
n_i	population of the i^{th} level
M^2	m square parameter for a laser beam
$w(z)$	spot size of the laser beam as a function of propagation distance z
$(\Sigma_\mu)_{exp}$	experimental integrated absorption coefficient
$(\Sigma_\mu)_{calc}$	calculated integrated absorption coefficient
$\mu(\lambda)$	absorption coefficient at the wavelength λ
$\bar{\lambda}$	mean wavelength of the absorption band or bands for overlapping cases
n	refractive index

c	speed of light
h	Planck's constant
J	total angular momentum quantum number of the ground state
N_o	rare-earth ion (Tm^{3+} in our case) concentration
$U^{(t)}$	doubly reduced matrix elements of the unit tensor operator of rank t
Ω_t	Judd-Ofelt intensity parameters
e	electronic charge
E_{zl}	energy difference between lowest Stark level of upper multiplet and lowest Stark level of lower multiplet called the zero line energy
$I(\lambda)$	normalized fluorescence intensity at wavelength λ
N(t)	excited ion density
$\Pi(t)$	deviation of decay of excited ions from intrinsic decay
N_A	acceptor ion concentration
x	normalized time variable
D	diffusion coefficient
C	interaction parameter
R_o	critical distance parameter
E_{th}	threshold pump energy
τ_p	pump pulsewidth

Chapter 1

INTRODUCTION

A laser, where the name stands for “Light Amplification by Stimulated Emission of Radiation”, typically requires a gain medium inside a stable resonator cavity consisting of highly reflecting mirrors. The gain medium excited by a pump source provides optical amplification via stimulated emission and the resulting radiation resonates inside the cavity. Radiation is extracted from a laser with the help of a partially transmitting mirror called the output coupler. The general classification of lasers is made according to the gain medium. Those which have a crystal or glass as the gain medium are called solid-state lasers. In this class of lasers, the crystal or glass which is called the host is doped with an active ion (a rare-earth or transition-metal ion, for example). In fact, the first demonstration of lasing was done by Maiman[1] in 1960 with a solid-state ruby laser which had a sapphire crystal doped with chromium ions as the gain medium. Lasers are further categorized according to the wavelength of operation and among the various wavelength ranges the mid-infrared (mid-ir) region covers the 2-5 μm (micron) range. This thesis will be mainly based on the research work done on thulium-doped mid-infrared solid-state laser systems operating in the 1.9-2.1 μm wavelength range. Mid-infrared systems emitting around 2 μm have been gaining importance due to a growing number of applications in medical surgery, atmospheric sensing and range finding, as well as pumping of other mid-infrared solid-state lasers or optical parametric oscillators (OPO).

The organization of the thesis will be such that a background on thulium-doped solid state laser systems will be given in Chapter 2. This background will include a review of laser gain mechanisms and dynamics relevant to the continuous-wave laser, energy structure, spectroscopy and lasing characteristics of thulium-doped systems, and an extensive overview of two-micron lasers and their applications. The following chapter will include the study of continuous-wave (CW) operation of thulium-doped $YAlO_3$ (Tm:YAP or Tm:YAlO) laser. Two experiments will be discussed in this section; influence of doping concentration on the performance of diode-pumped laser operation and low-threshold operation of Tm:YAP laser pumped by a Ti:sapphire laser. The subject of Chapter 4 is a joint project with a biomedical group from Bogazici University to develop a surgical system based on Tm:YAP laser. Spectroscopic characterization of laser materials will be described in the next chapter with two specific examples; a thulium-doped garnet LuAG (Tm:LuAG crystal) and thulium-doped telluride-based glass Tm_2O_3:(0.85)TeO_2-(0.15)WO_3. Finally, Chapter 6 will cover lasing trials with telluride-based glasses and laser action in neodymium-doped telluride glass.

Chapter 2

BACKGROUND

2.0 Introduction

This chapter is intended to introduce the reader to two-micron solid-state lasers and their applications, and to provide a background for the following chapters. Following three sections (2.1, 2.2, 2.3) of this chapter give a general description of continuous-wave (CW) lasers discussing gain mechanism, threshold and CW operation, respectively. The next three sections introduce the thulium-doped systems by describing the energy structure, spectroscopy and lasing characteristics of these systems. The introduction of thulium systems is followed by a substantial review on two-micron lasers in a historical perspective in Section 2.7. Finally, Section 2.8 covers the applications of two-micron solid-state lasers in three subsections: medical applications, remote sensing and pumping of other solid-state lasers.

2.1 Gain Mechanism in Lasers

In a laser gain medium, optical amplification takes place as a directional photon propagating inside the resonator cavity is incident on the gain medium which has been excited by the pump source, and causes other directional photons to be emitted. These new photons will contribute to and increase the radiation propagating inside the cavity. This process is called optical amplification by stimulated emission of radiation. Meanwhile, other photons are also emitted spontaneously from the excited gain medium with random propagation directions which do not contribute to the laser radiation but are wasted away,

and this is called spontaneous emission. Optical amplification (gain) is provided by active elements in the gain medium which are ionized dopant atoms inside a host crystal or glass in the case of solid state lasers. The radiative and nonradiative transitions of valence electrons in active ions generate the laser activity. The remaining discussion in this chapter will be in the context of solid state lasers.

Lasers can be divided into two main categories based on their gain mechanisms: three-level and four-level. A simplified energy diagram of a three-level system is shown in Fig. 2.1 where the lower laser level and ground level are the same. When an active ion in the gain medium is excited from the ground state to the pump level in such a system, this ion decays rapidly (and generally nonradiatively) to the upper laser level. Laser transition takes place from this level to the lower laser level (ground level) with the emission of a photon. In a four-level system (see Fig. 2.2), on the other hand, the lower laser level and ground level are separate and the lower laser level is vacated rapidly via nonradiative decay. So the ion population in the lower laser level will always be nearly zero in four-level systems, while in three-level mechanisms there will always be active ions in the ground state populating simultaneously the lower laser level. Clearly, three-level systems require more intense pumping to generate population inversion (state of having more active elements in the upper laser level than the lower laser level) and thereby, are less efficient compared to four-level systems.

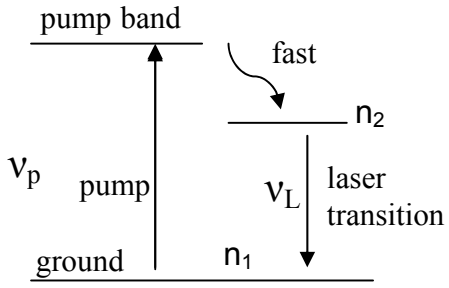

Fig 2.1. Three-level gain system.

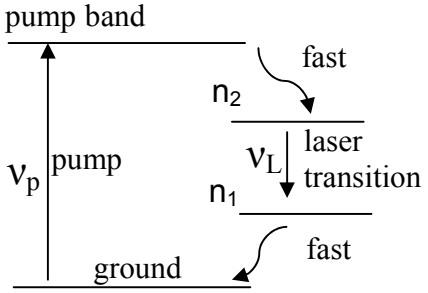

Fig 2.2. Four-level gain system.

The gain coefficient of an active medium can be calculated from

$$g = \sigma_L \Delta N \tag{2.1}$$

where σ_L is the stimulated emission cross section, the material parameter indicating the strength of the laser transition, $\Delta N = n_2 - (g_2/g_1)n_1$ *is* the population inversion, n_2 and n_1 being the population of active ions in the upper and lower laser level, respectively, and g_2, g_1 are the degeneracy factors. Stimulated emission entering the gain medium is amplified exponentially according to $I(z) = I(0)e^{gz}$ where z is the distance that the radiation propagates inside the medium The total amplification in one round-trip inside the laser cavity then equals e^{2gl}, l being the length of the gain medium along which the radiation (generated by stimulated emission) propagates. The round-trip gain has to equal round-trip resonator loss for lasing to occur. Lasing initiates when radiation inside the cavity resonates and remains constant after one round trip so that it does not decay away. For this the resonator cavity has to be stabilized also, meaning that laser intensity propagating inside the cavity in the form of a Gaussian beam will resonate and not leak out. The state at which lasing starts is called threshold, and the gain coefficient at lasing threshold is called threshold gain. The condition for threshold in a two-mirror cavity is given by

$$e^{2gl} = e^{2\alpha l}\,(1/(R_1R_2)) \tag{2.2}$$

where the right hand term represents total loss inside cavity. In (2.2) α is the differential loss coefficient of the cavity accounting for all loss except transmissions of mirrors, and R_1 and R_2 are the mirror reflectivities.

2.2 Threshold

To reach lasing threshold, the laser has to be pumped with sufficient power so that threshold gain is obtained which means that threshold population inversion ΔN_{th} has to be achieved (see Eq. (2.1)) since emission cross section σ_L is a characteristic of the gain medium. Population inversion is a function of the pumping rate, that is the rate at which active elements in the gain medium are excited from the ground state to the pump level and so to the upper laser level since decay to this level from the pump level is very fast. Since pumping rate is directly related to the pump power, using rate equations for populations of energy levels involved in the laser activity and equations for Gaussian beam propagation, the incident threshold pump power for three and four-level[2] systems can be derived as

$$P_{th} = \frac{\pi h \nu_p (w_L^2 + w_p^2)(T + L + 2N\sigma_L)}{4\tau\eta_a\sigma_L} \qquad \text{(three-level)} \qquad (2.3)$$

$$P_{th} = \frac{\pi h \nu_p (w_L^2 + w_p^2)(T + L)}{4\eta_a\tau\sigma_L} \qquad \text{(four-level).} \qquad (2.4)$$

In Eqs.(2.3) and (2.4), several important laser parameters are employed: ν_p is the frequency of the pump radiation, w_L and w_p are beam waist spot sizes of laser mode and pump, respectively, T is the output coupler transmission, L is the round-trip passive cavity loss, N is the active ion (dopant) concentration in the gain medium, η_a is the fraction of pump power absorbed by the gain medium. η_a further equals $1 - \exp(-\alpha_p l)$ where $\alpha_p = N\sigma_a$ is the absorption coefficient at pump wavelength and σ_a is the absorption cross section at the pump wavelength, τ is the fluorescence lifetime of the upper laser level (see Section 2.5). Normally, the pump beam is focused inside the gain medium and the cavity mode waist (focus) is made to coincide with the pump waist (focus) as much as possible so that efficient pumping of the gain medium and transfer of energy to the laser mode can take place.

At a first look at the above equations for threshold, one can see that tight focusing of the pump, smaller laser mode spot size, lower loss inside cavity, higher absorption of pump and larger emission cross section are factors that lower the threshold pump power which is desired for practical and efficient systems. Also the three-level equation has the extra term $2N\sigma_L$ which represents reabsorbtion, the absorption of photons (emitted from the upper laser level) by the ground state ions. Since the pumping in three-level systems has to overcome reabsorption, these systems require higher threshold pump powers and are less efficient compared to four-level systems.

2.3 Continuous-Wave (CW) Operation

In cw operation, as the pump power is increased above threshold, more active ions are excited to the upper laser level increasing the gain which is instantaneously saturated down to the threshold level by the increasing stimulated emission. Remember that at the threshold gain level, resonating laser intensity inside the cavity remains constant after one round-trip. Hence the gain stabilizes at the threshold level instantaneously at each pump level while laser intensity (or equivalently laser power) inside cavity stabilizes at a higher level. This is called gain saturation and the unsaturated gain is called small signal gain. If gain saturation did not take place, resonating power inside would blow up and cw laser operation would not be possible. The process can be visualized with the help of Fig. 2.3 where gain saturation is described using a simplified gain versus frequency profile for a homogeneous medium where all active ions have identical gain profiles. The straight lines represent stabile modes of the laser cavity, and lasing occurs at the frequency ν_L where the maximum region of the gain intersects a cavity mode.

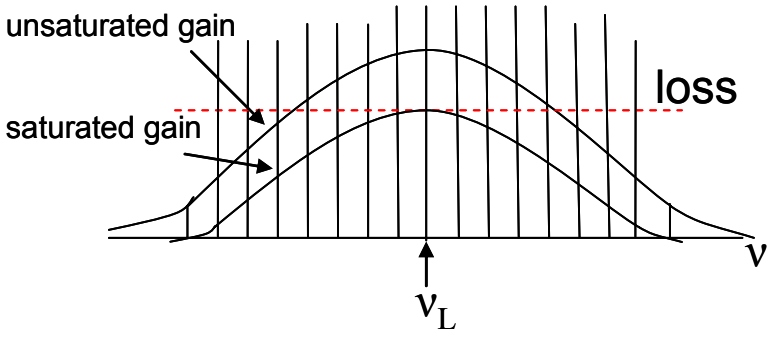

Fig. 2.3 Saturation effect in a homogeneous gain medium

On the other hand, at the output of the laser a small portion of the internally circulating power is extracted through a partially transmitting mirror (output coupler or OC). As the pump power is increased above threshold, output power of laser increases linearly with a slope η_s called the slope efficiency (also called differential efficiency by some)as shown in Fig. 2.4.

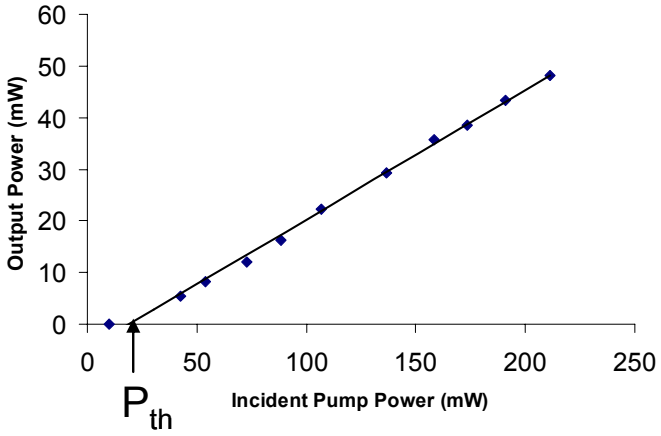

Fig. 2.4 Typical power efficiency curve for a cw laser

The slope efficiency for a four-level system is given by

$$\eta_s = (T/(T+L))\ (\nu_L/\nu_p)(\eta_a). \quad (2.5)$$

In Eq. (2.5) ν_L/ν_p is called the quantum efficiency. (1- ν_L/ν_p) is known as the quantum defect. Quantum defect is a limitation on the efficiency of the system exerted by the lasing-pumping transition scheme utilized to obtain lasing. According to Eq. (2.5), efficiency will increase at first when output coupler transmission T is increased from zero, the extent of the increase depending on the relative size of L with respect to T, but reach an optimum level where it will begin decreasing when T is increased further. Also increasing T will cause the threshold pump power to increase. So in designing a laser cavity, T is usually chosen by taking into account its effect on both threshold and efficiency. In general, threshold pump power and slope efficiency are two main performance parameters of cw lasers and lowering the threshold and improving the efficiency are two main driving forces of laser research.

2.4 Energy Structure of Thulium-Doped Systems

Thulium is one of the rare-earth atoms used as a doping impurity in host crystals (or glasses) to form gain media for solid state lasers. These rare-earth atoms (Nd, Er, Ho, Tm, Yb, etc.) are also called trivalent lanthanides since they form 3^+ ions inside the host. Due to the isolation by outer electron shells and weak effect of crystal field, energy structures of the trivalent rare earth ions do not change significantly from host to host. Thus they can be accurately approximated by the trivalent rare earth ions in aqueous or gaseous solutions. Thulium(Tm) in ionic form replaces one of the 3^+ ions inside the host. Thulium atom, with atomic number 69, has the following atomic configuration[3]

$$1s^2 2s^2 2p^6 3s^2 3p^6 4s^2 3d^{10} 4p^6 5s^2 4d^{10} 5p^6 6s^2 4f^{13}.$$

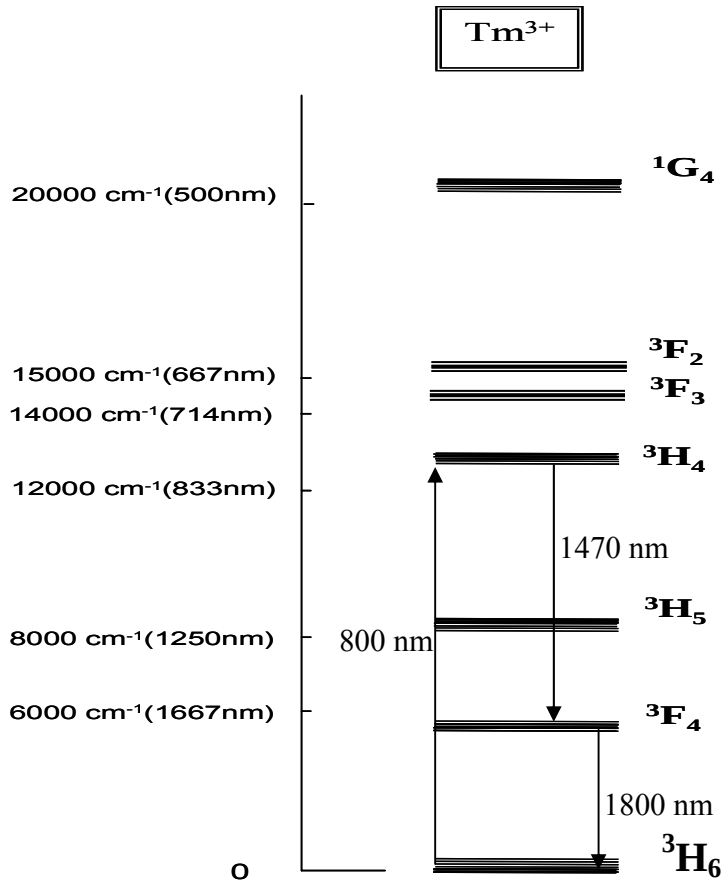

Fig. 2.5. Energy level diagram of 4f shell of Tm^{3+} ion.

Trivalent Tm^{3+} ion is formed as two 6s electrons and one 4f electron form bonds with atoms of the host molecules. Twelve electrons remain in the 4f shell of trivalent thulium ion. The transitions of 4f electrons among energy levels of partially filled 4f shell bring about the fluorescence spectrum in the 700-2300 nm range. The energy diagram of the Tm^{3+} ion relevant to this spectroscopic range is shown in Fig. 2.5. It should be noted that

the name of the $^3H_4$ and $^3F_4$ levels are reversed in some references such as[4-6], but in this thesis the notation accepted most commonly in laser research[7, 8] will be used. The splitting of the energy levels of the 4f shell shown in Fig. 2.5 is dominated by coulomb forces and spin-orbit interactions between 4f electrons which are not influenced by the host since 4f states are isolated to a good extent by the 5s and 5p shells which are full. These energy separations are represented by the 2000-10000 cm^{-1} gaps among the thick bars in the diagram. Each of the levels depicted by thick bars is associated with an electronic energy level of the thulium atom with total angular momentum value J which is represented by the subscript in the name of each level. For example the J value for $^3H_6$ level is six. For a value of J, 2J+1energy levels are allowed. The effect of the host occurs in the fine splitting of these 2J+1 levels. So the thick bars in the diagram contain several closely separated lines. This is called the Stark effect and occurs due to the lattice vibrations. This effect splits an electronic energy level with a certain J value into 2J+1 vibronic energy states called Stark levels. These levels are separated nearly equally with energy gaps on the order of 100 cm^{-1}. A set of closely split Stark levels born from the same electronic level designated by a J value as the subscript is called a manifold or a multiplet such as the $^3F_4$ multiplet.

2.5 Spectroscopy of Thulium-Doped Systems

Spectroscopic characteristics of Tm-doped solid state materials are the outcome of the radiative and nonradiative processes which take place in and among Tm^{3+} ions which are the active elements inside the crystal. When the ions are excited to a higher energy level by absorbing light photons, they decay afterwards to their ground state via radiative and nonradiative relaxation mechanisms. Transitions between electronic states and transitions between vibronic states that are assisted by phonons, both of which emit photons, constitute radiative relaxation mechanisms. On the other hand, transitions that involve phonon

emission, energy migration and/or energy transfer via ion-ion or ion-crystal lattice interactions make up nonradiative relaxation processes. The lifetime of an energy state (excited state life time or fluorescence lifetime) indicates the spontaneous decay rate of that state via radiative and nonradiative mechanisms after excitation. In equation form, the fluorescence lifetime (or just the lifetime) of an excited state i is given by

$$\frac{1}{\tau_i} = \frac{1}{\tau_{ir}} + \frac{1}{\tau_{in}} \tag{2.6}$$

where τ_{ir} and τ_{in} represent radiative and nonradiative lifetimes of state i respectively. The radiative and nonradiative lifetimes of an excited state i in return are

$$\frac{1}{\tau_{ir}} = \sum_j A(i,j), \tag{2.7}$$

$$\frac{1}{\tau_{in}} = \sum_j W(i,j) \tag{2.8}$$

where *A(i,j)* and *W(i,j)* denote the spontaneous emission rate (probability) and nonradiative transition rate (probability), respectively, from excited state i to terminal level j and the summation is over all terminal states. The branching ratio, also called the fluorescence branching ratio, indicates the strength of a decay from an excited state i to a certain terminal level j and is stated as

$$\beta_{ij} = \frac{A(i,j)}{\sum_j A(i,j)} = \tau_{ir} A(i,j). \tag{2.9}$$

The luminescence quantum efficiency for an excited state given by the ratio of fluorescence lifetime to radiative lifetime as

$$\eta = \frac{\tau}{\tau_r} \tag{2.10}$$

indicates the strength of radiative emission in the decay of that state.

In the case of rare earth ions such as Tm^{3+} inside a host, the Stark levels inside the upper and lower manifolds are so closely located so that only the average lifetimes (decay rates) for a multiplet can be measured. The spontaneous emission rate from a Stark level *i* inside a multiplet a to all components j of another multiplet b is

$$A(i,b) = \sum_j A(i,j). \tag{2.11}$$

If it is assumed that equal populations reside in each level i inside multiplet a, then the measured rate *A(a,b)* will be the average of the multiplet given by

$$A(a,b) = \frac{1}{2J+1}\sum_i A(i,b) \tag{2.12}$$

as *J* is the total angular momentum value associated with the multiplet and 2J+1 are the energy levels inside it.

2.6 Lasing Characteristics of Thulium-Doped Systems

The transitions that underlie the lasing and fluorescence activities in thulium-doped systems covered in this thesis involve mainly $^3H_6$ multiplet as the ground level, $^3F_4$

multiplet as the upper laser level for the 2-micron radiation (1.8-μm emission band), and $^3H_4$ as the pump level which is also the upper level for the 1.5-μm emission band (see Fig. 2.5). Exciting a thulium-doped gain medium at 0.8 μm generates two important radiative emissions: one band centered around 1.5 μm holds a potential for developing fiber-optic amplifiers in telecommunication systems, while the second band centered around 1.8 μm, which produces the two-micron laser radiation, is suitable for developing lasers for medical applications as well as atmospheric and chemical sensing. Note that the lower level for the 1.5-μm transition is the $^3F_4$ multiplet which is at the same time the upper level of 1.8-μm transition.

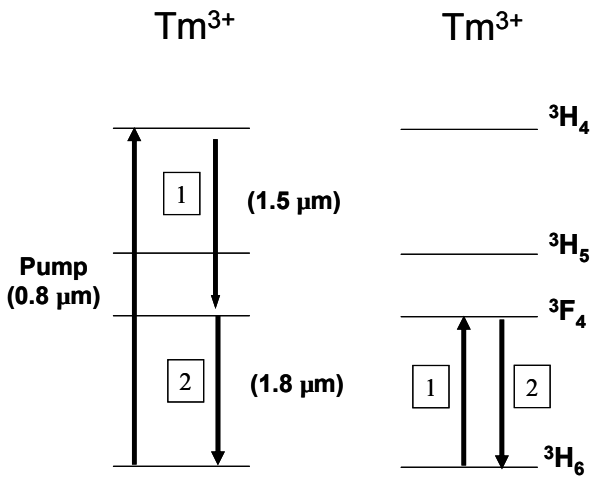

Fig. 2.6 The interaction between two nearby Tm^{3+} ions via cross-relaxation.

An important characteristic of thulium-doped systems is the cross relaxation process which is a self quenching effect of the 1.5- μm emission that boosts the efficiency of the 1.8-μm emission. Cross relaxation process becomes effective with increasing concentration of Tm^{3+} ions inside the host. As shown in Fig. 2.6, in this process two nearby ions interact nonradiatively, and one of them that has been excited to the $^3H_4$ level decays nonradiatively

down to the $^3F_4$ level, promoting the other ion in the ground state to the $^3F_4$ level. Thus, two ions are excited to the $^3F_4$ level with one pump photon enhancing the efficiency of the 1.8-μm emission. This is an important effect that has to be taken into account in designing thulium lasers, and especially for those operating at two-micron, doping concentration is made high enough to quench the 1.5-μm emission in favor of the laser emission.

Another important aspect of the Tm-doped systems is the quasi-three level gain mechanism of the 1.8-μm emission band which generates the lasing around 2 μm. The quasi-three level mechanism is an outcome of the close separation in energy of the ground and lower laser level which are Stark levels both located in the $^3F_4$ manifold. The proximity between the lower laser level and the ground level results in a significant population of Tm^{3+} ions occupying the lower laser level as predicted by the Boltzman distribution. The nonradiative relaxation rates of Stark levels inside a multiplet are much faster than other transition mechanisms in laser crystals. Hence these closely located levels inside a multiplet come into thermal equilibrium very quickly. Accordingly, the fraction of the population of a multiplet a residing in a Stark level i can be approximated by the Boltzman distribution

$$f_{ai} = \frac{\exp(-E_{ai}/kT)}{Z_a} \tag{2.13}$$

where E_{ai} is the energy of level i and Z_a is the partition for the multiplet a given by

$$Z_a = \sum_{i=1}^{m} \exp(-E_{ai}/kT) \tag{2.14}$$

m being the total number of Stark levels inside the multiplet a. Then, in a quasi-three level laser system the population inversion is given by[9]

$$\Delta N = f_2 n_2 - f_1 n_1 \tag{2.15}$$

where n_2 and n_1 are the populations of the multiplets ($^3F_4$ and $^3H_6$ in the case of Tm^{3+}) containing the upper and lower laser levels, respectively, and f_2 and f_1 are the fractions of the manifold populations that occupy the upper and lower laser levels, respectively. Lasing occurs when the population of ions residing in the upper laser level exceeds those of in the lower laser level with a certain threshold difference. The fractional inversion F equals the fraction of ground-state ($^3H_6$) ions that needs to be raised to the excited state ($^3F_4$) so that equal populations reside in the upper and lower laser levels. The change in F with temperature gives an indication of the threshold pump power variation with temperature. The fractional inversion occurs when

$$f_2 n_2 = f_1 n_1 . \tag{2.16}$$

Since laser operation of concern here is around room temperature, it is safe to assume that

$$n_1 + n_2 = N, \tag{2.17}$$

meaning only the ground state and excited state are populated. Then the fractional inversion F denoting the fraction of total ion population that needs to be excited to the $^3F_4$ state equals

$$F = \left(\frac{n_2}{N} \right) = \frac{f_1}{f_1 + f_2} . \tag{2.18}$$

The pump threshold formula for a quasi-three level laser is similar to the three-level system[7, 10, 11]

$$P_{th} = \frac{\pi h \nu_p (w_L^2 + w_p^2)(T + L + 2Nlf_1\sigma_L)}{4\tau\eta_a f_2 \sigma_L} \tag{2.19}$$

except for the addition of f_1 and f_2. As it is clear from (2.15) and (2.19), the close splitting between the lower laser and ground level is a disadvantage in quasi-three level systems which require intense pumping to obtain population inversion and to counteract reabsorption represented by $2Nlf_1\sigma_L$. In such systems, cryogenic cooling would be one way to reduce the lower laser level population (or f_1) and increase the lasing efficiency. The threshold pump power can be related to the threshold inversion

$$\Delta N_{th} = \left(f_2 n_2 - f_1 n_1\right)_{th} \tag{2.20}$$

using the rate equation for the intracavity laser power P which is identical for all of four, three and quasi-three level lasers

$$\frac{dP}{dt} = \frac{-P}{\tau_c} + \frac{2gP}{T_R} \tag{2.21}$$

where τ_c given by

$$\tau_c = \frac{2l_c}{c\left(L + T + 2Nlf_1\sigma_L\right)} \tag{2.22}$$

is the cavity lifetime equal to cavity round-trip time $T_R=(2l_c/c)$ divided by total loss, l_c is the effective cavity length and g is the single pass fractional gain defined by Eqn. (2.1). Using steady state approximation $\frac{dP}{dt}=0$ and P≈0 at threshold, it can easily be shown that

$$\Delta N_{th} = \frac{L + T + 2Nlf_1\sigma_L}{2\sigma_L l} \tag{2.23}$$

noting that *l* equals crystal(gain medium) length. Substituting $L + T + 2Nlf_1\sigma_L = 2\sigma_L l\Delta N_{th}$ in (2.19) the threshold inversion ΔN_{th} can be related to threshold pump power P_{th} as

$$\Delta N_{th} = \left[\frac{\pi h\nu_p l(w_L^2 + w_p^2)}{2\tau\eta_a f_2}\right]^{-1} P_{th} \quad . \tag{2.24}$$

2.7 A Historical Review of Solid State Lasers Operating Around 2 μm

The mid-infrared (mid-IR) solid state lasers that utilize crystals doped with active ions can be classified into four main groups based on the dopant ion[12]: transition-metals (Ni^{2+}, Co^{2+}, Cr^{2+}, Fe^{2+},..) rare earth or lanthanides (Tm^{3+}, Ho^{3+}, Er^{3+},..), actinides(U^{3+}), and F-centers. Among them, lasers based on rare earth ions Tm^{3+} and Ho^{3+} (trivalent holmium ion) are main sources of two-micron radiation. In thulium-doped (Tm-doped or Tm^{3+}-doped or Tm-based or Tm or thulium) systems $^3F_4 \rightarrow {}^3H_6$ transition produces lasing in the 1.9-2.02 μm range and in holmium-doped (Ho-doped or Ho^{3+}-doped or Ho-based or Ho or holmium) systems $^5I_7 \rightarrow {}^5I_8$ transition generates lasing in the 1.95-2.15 μm range.

Due to the quasi-three level nature of holmium and thulium lasers, these systems require intense pumping to populate the upper laser level. For the case of Ho-based lasers, two different pumping mechanisms have been used to populate the upper laser level $^5I_7$ at 1.9 μm. One (see Fig. 2.7) is the co-doping of the crystal host with Tm^{3+} ion as a sensitizer

in addition to Ho^{3+} ion (active ion or activator) and the other is the pumping directly with other laser sources operating around 1.94 μm, mainly Tm-based ones. Lasers using the first

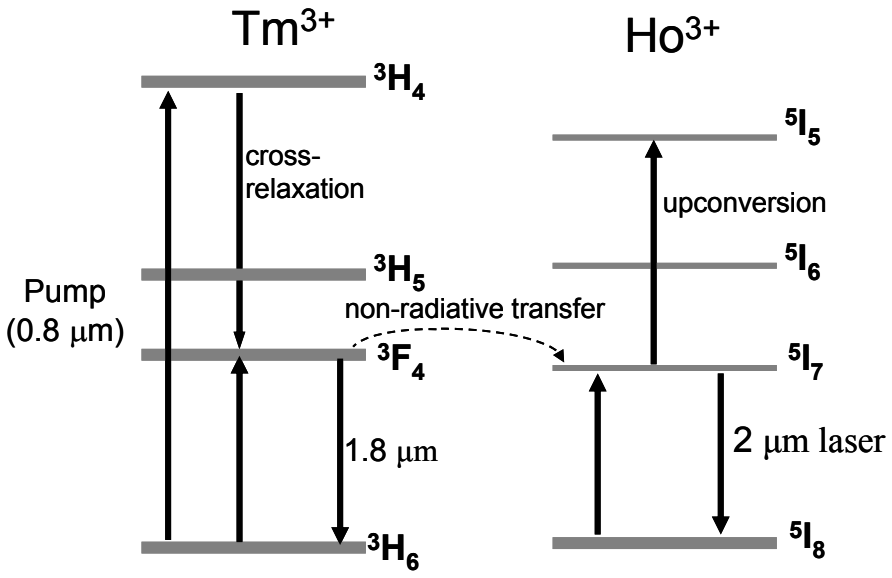

Fig. 2.7 Energy diagram of sensitized holmium laser[13].

pumping scheme will be called sensitized Ho lasers and those using the second scheme will be called in-band pumped Ho lasers in this thesis in parallel with the common terminology in the literature. Both cases involve energy transfer from the $^3F_4$ level of Tm^{3+} ion to the $^5I_7$ level of Ho^{3+} level, except that, co-doping involves a spontaneous nonradiative mechanism, while pumping with 1.9 micron lasers are based on radiative energy transfer via stimulated emission. In the sensitization scheme shown in Fig. 2.7., the cross relaxation (see Section 2.6) between Tm^{3+} ions enhances the energy transfer to the Ho^{3+} ions by populating the $^3F_4$ level but the upconversion processes from the $^5I_7$ level of Ho^{3+} ions significantly impair the efficiency. An upconversion process describes a transition from the upper laser level to a higher energy level fuelled by decay to a lower level matching in energy. In each of the two effective upconversion mechanisms in sensitized Ho lasers, the $^5I_7 \rightarrow {}^5I_5$ upward transition removes a Ho^{3+} ion from the upper laser level which is matched by a downward $^3F_4 \rightarrow {}^3H_6$

transition in Tm^{3+} in one and $^5I_7 \rightarrow {}^5I_8$ transition in Ho^{3+} in the other. Although in-band pumped Ho lasers are basically free of the unfavourable upconversion effects, earlier holmium lasers used the sensitization scheme since pump lasers were not available or practical. On the other hand, the pumping system in thulium lasers is the excitation of the $^3H_4$ level with radiation in the 780-800 nm range, varying according to the host. Earlier systems were pumped with flashlamps in pulsed mode before laser diodes at the required excitation wavelengths became available as intense and stabile pump sources. Due to the wide spectral range of radiation from the flashlamps, additional co-doping with trivalent chromium (Cr^{3+}) and/or erbium (Er^{3+}) ions, which have broad absorption bands, was utilized to enhance pump absorption in both Tm and sensitized Ho lasers. In 60s and early 70s, first demonstrations of pulsed lasing in sensitized Ho^{3+} and Tm^{3+}- doped crystal hosts $CaWO_4$ (calcium tungstate)[14, 15], yttrium aluminum garnet (YAG)[16], yttrium aluminum oxide (YAlO or YAP)[5, 17], yttrium gallium garnet (YGG) and yttrium iron garnet (YIG)[18] employed cryogenic cooling (down to liquid nitrogen temperature of 77 K) of the gain medium. This was done to decrease the lower laser level population and thus reduce reabsorption. Soon after the first demonstrations, researchers achieved room-temperature pulsed laser operation in sensitized Ho-doped yttrium lithium fluoride (YLF) and yttrium aluminum garnet (YAG)[19]. In later years, researchers obtained room-temperature flashlamp-pumped lasing in other Ho-doped garnets yttrium scandium gallium garnet(YSGG), gadolinium scandium aluminum garnet (GSAG), yttrium scandium aluminum garnet (YSAG), and lutetium aluminum garnet (LuAG) sensitized with Tm^{3+} and Cr^{3+}[20, 21].

A critical issue with the lasers using sensitizing mechanism in the gain medium was optimizing the concentration of the sensitizer and activator ions for best performance. In Ho-based lasers, higher concentration of Tm^{3+} ions was used to enhance population of the $^3F_4$ state through inter-ionic transfer mechanisms such as cross relaxation (see Section 2.6) and lower concentration of the activator Ho^{3+} to limit reabsorption. But there was a limit to

the increase of the Tm^{3+} concentration since it intensified the loss due to upconversion. Also, in both Ho and Tm lasers the concentration of the sensitizer (Er^{3+}, Cr^{3+}) for facilitating absorption required optimizing to improve performance through a balance between increased absorption and losses. As a matter of fact, following the early demonstrations of lasing, studies to optimize the dopant (activator) and co-dopant (sensitizer) concentrations resulted in enhanced performance of flashlamp-pumped Cr,Tm,Ho:YAG (sensitized Ho:YAG)[22-24] and Cr,Tm:YAG (sensitized Tm:YAG)[25-29] lasers.

The performance of two-micron lasers was significantly boosted with the introduction of continuous-wave (cw) laser diodes as pump sources operating in the 780-800 nm range in the second half of 80s. The narrow and intense spectral output of the laser diodes matching the pump wavelength of the Tm^{3+} ion increased the pumping efficiency greatly in thulium-sensitized holmium and thulium lasers, as opposed to the wide spectral distribution of the flashlamp radiation which provided poor pumping efficiency. Specifically, GaAlAs laser diodes, which have temperature-tunable operating wavelengths, match the pump transitions of Tm^{3+} ion in various hosts(785 nm in YAG, 790 nm in YLF, 795 nm in YAlO, 788 nm in LuAG, etc.). While with room-temperature flashlamp-pumped Ho[22, 24]- and Tm[26]- YAG lasers highest slope efficiencies in the 3-5% range and lowest threshold energies in the 10-50 Joule range could be achieved, with diode-laser pumping, efficiencies as high as 30% and thresholds below 5 mW were obtained in early room-temperature sensitized Ho-doped YAG[30] and YLF[31], and Tm-doped YAG[32] lasers. Early demonstrations of diode-pumped cw two-micron lasers were cryogenically-cooled Er,Tm,Ho:YAG[33], cryogenically-cooled and room-temperature Er,Tm,Ho:YLF[31, 34] lasers, and room-temperature Tm,Ho:YAG[30, 35, 36] and Tm:YAG[32, 37] lasers. Soon after these early results, q-switched operation in Tm:YAG[38, 39], Tm,Ho:YAG[38], Tm,Ho:YLF[40], slope efficiency of 49% in Tm:YAG[39], and output powers above 500 mW in Tm:YAG[39] and Tm,Ho:YLF[40]

lasers were obtained with diode-pumping. Further, high average-power diode-pumped operation in the 5-14 W output range was achieved in quasi-cw (long pulse) and q-switched Tm:YAG[41] and thulium-sensitized Ho:YAG[41-43] lasers in the first half of 90s. Following YAG and YLF, diode-pumped lasing performance also in other thulium sensitized Ho-doped crystal hosts such as YAlO[8], lutetium lithium fluoride ($LiLuF_4$ or LuLF)[44], and Tm-doped LuAG[45, 46], YAlO[8, 47, 48], YVO_4 (vanadate)[49], and $GdVO_4$ (gadolinium vanadate)[50] was studied. More recently, Tm-doped fluoride LuLF[51] and double-tungstates $NaGd(WO_4)_2$[52] and $KLu(WO_4)_2$[53] have been added to the list of diode-pumped room-temperature lasers operating around 2 μm.

Efficient operations of thulium and sensitized holmium lasers were demonstrated also with pumping by other lasers which have the advantage of narrow spectral output as the laser diodes and higher coherence as a superior aspect. On the other hand, stability, small size and lower cost are the superior aspects of laser diodes. Hence lasers such as Cr:GSAG[54], Ti:sapphire[55], alexandrite laser[56] have been used to simulate diode lasers. Examples to the cw two-micron lasers pumped by other lasers are: chromium-thulium-sensitized Ho:YSGG and Ho:YSAG pumped by a krypton laser[57], thulium-sensitized Ho:YLF pumped by an Alexandrite laser[56], Tm sensitized Ho:LuAG pumped by a $Co:MgF_2$ laser[58], Tm:LuAG pumped by a $Co:MgF_2$ laser[59], Tm:YAG pumped by a Nd:YAG laser[60], Tm:YAG[61], Tm:YSGG[61], $Tm:YVO_4$[49, 62], Tm:YAlO[7], $Tm:GdVO_4$[63, 64], $Tm:CaF_2$[65], $Tm:KGd(WO_4)_2$[66], $Tm:NaGd(WO_4)_2$[52], $Tm:KY(WO_4)_2$[67], $NaLu(WO_4)_2$[68] and thulium-sensitized Ho:LuAG[55, 69] pumped by a Ti:sapphire laser. Also a pulsed thulium-sensitized Ho:YAG pumped by a flashlamp-pumped Cr:GSAG laser was demonstrated[54]. Further, researchers have obtained mode-locking in a Tm:YAG[70] laser pumped by Ti:sapphire, and Cr,Tm:YAG and Cr,Tm,Ho:YAG lasers pumped by a krypton laser[71].

In-band pumped holmium lasers have the advantage of much weaker detrimental upconversion effects compared to sensitized Ho lasers, but had to wait for thulium lasers to

become available as pump sources. First two demonstrations in 92 were both Ho:YAG lasers pumped by 2.01-μm Tm:YAG in intracavity configuration where the gain mediums of the pump and output laser share the same resonator cavity[72, 73]. In one of these cases, the Tm:YAG was pumped by a cw Ti:Sapphire at 785 nm and the slope efficiency with respect to the absorbed 785-nm power was 42%[73]. The other one was a lower efficiency system pumped by a flashlamp-pumped Cr,Tm:YAG laser[72]. Then the Ho:YAG laser was also pumped by diode lasers operating at 1.9-μm[74], though with less efficiency compared to the previous case owing to the deficiency of the diodes at this wavelength. In another demonstration of a cw Ho:YAG laser intracavity pumped by diode-pumped Tm:YAG laser, 2.1-W output power was obtained with both gain and pump medium maintained at 10 ^{o}C[75]. In addition, Tm:YLF laser with output around 1.9 μm has been used in intracavity pumping configurations and up to 14 W of cw power has been demonstrated with Ho:YAG lasers[76-78]. Ho:YAG lasers has been also pumped resonantly (or externally as opposed to intracavity) by Tm:YAlO (free running wavelength varying in the 1.94-1.99 μm according to resonator loss) and Tm:YLF (free running wavelength around 1.9 μm) lasers which match the in-band pumping wavelength closely. As an example, a 1.8 W Ho:YAG laser was demonstrated with cw diode end-pumped 8.8 W Tm:YAlO as pump laser[79]. In cw experiments using in-band pumping by Tm:YLF laser, up to 38 W output power and 60 % efficiency with respect to incident power has been obtained[80, 81]. In addition, 50 mJ of Q-switched energy was achieved with a Ho:YAG resonantly pumped by a diode-pumped Tm:YLF laser[82].

Efforts to obtain higher power operation have continued with diode-pumped two-micron lasers. In the case of thulium sensitized holmium lasers, Tm,Ho:YLF laser has been generally preferred for high power research[83-87], since it was shown that upconversion effect is significantly weaker in Tm,Ho:YLF than Tm,Ho:YAG[88]. In these experiments, Q-switched pulse energy of 600 mJ has been demonstrated with Tm,Ho:YLF laser[87]. Further, pulse energy of 1 J was obtained in another Tm,Ho-doped LuLF[89]. There has

also been a considerable progress in power scaling experiments with Tm-based lasers. Researchers have gradually advanced the cw output to 120 W in Tm:YAG[90-92] and 50 W in Tm:YAlO[93-96] and 36 W in Tm:YLF[80, 94, 95] lasers with diode-pumped operation.

Finally, tunability of two-micron lasers has been demonstrated in several works. Some of the noteworthy examples are flashlamp-pumped Cr^{3+}-sensitized Tm^{3+}-doped garnets YAG (1.94-2.09 μm), YSGG (1.94-2.05 μm) and GSGG (1.92-2.04 μm)[28], Ti:sapphire-pumped cw Tm:YAG (1.87-2.16 μm)[61], Tm:YSGG (1.85-2.14 μm)[61], Tm:$KLu(WO_4)_2$ (1.80-1.99 μm)[53], Tm:CaF_2 (1.84-1.97 μm), Tm:$KGd(WO_4)_2$ (1.79-2.04μm)[66], Tm:$NaGd(WO_4)_2$ (1.81-2.03 μm)[52], Tm:YAP (1.84-1.99 μm)[97], diode-pumped cw Tm:$LiLuF_4$ (1.82-2.06 μm)[51] and Tm:YAP (1.90-2.03 μm)[98].

2.8 Applications of Two-Micron Lasers

In this section, applications of two-micron lasers will be reviewed in three parts: medical applications, remote sensing and pumping of solid state lasers. Most emphasis will be given to medical applications since two micron lasers (specifically holmium lasers) have been in extensive use in surgical applications and thulium lasers have recently been introduced as promising alternatives to Ho-based lasers. Also the coverage on medical applications will build a background for the biomedical project discussed in Chapter 4. Hence, an extensive subsection will be devoted to the two-micron lasers in medical applications. However, only a review on laser tissue welding (fusion) will be left out on purpose, to be included in the introductory section of Chapter 4. A second subsection will cover atmospheric and chemical sensing, and a third one will briefly mention pumping of solid state lasers.

2.8.1 Medical Applications

The first thing to note about two-micron laser radiation is that it falls in the eyesafe wavelength range which covers the spectrum of wavelengths longer than 1.4 μm. In the

eyesafe range, the liquid water inside cornea and vitreous humor of the eye absorbs the incident radiation to an extent that protects the retina[13]. Further, water has an absorption peak at 1.94 μm (see Fig. 2.8 taken from[99]) which makes two-micron lasers especially important for medical applications.

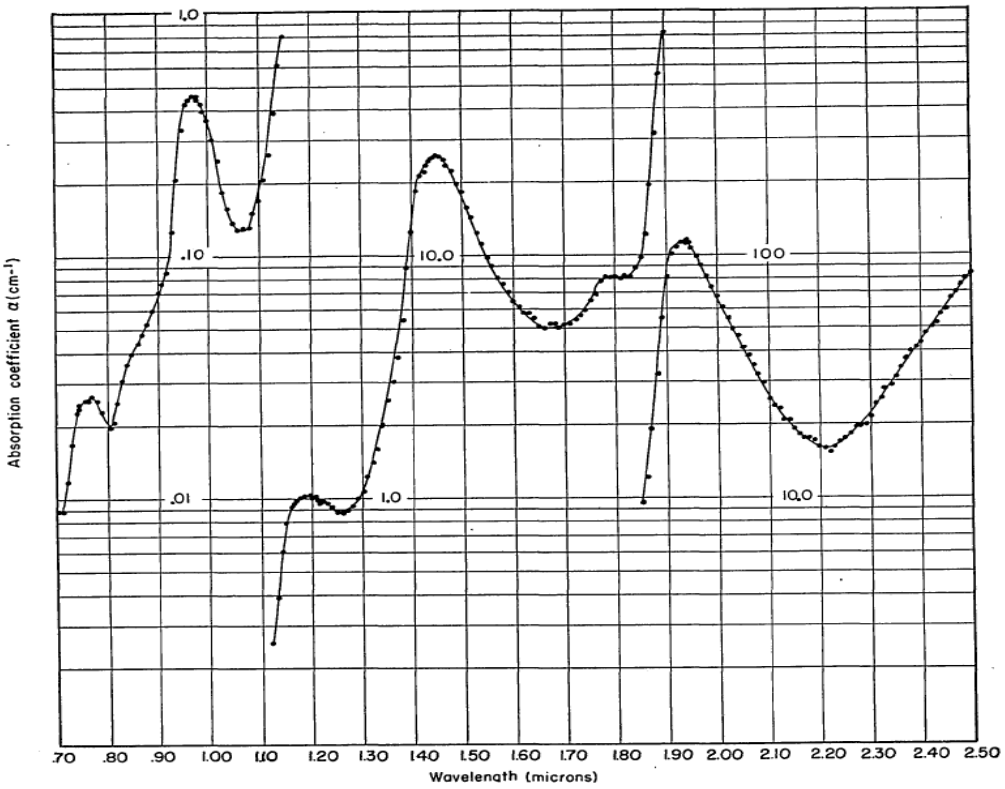

Fig. 2.8 Absorption spectrum of water in the 0.7-2.5 μm range[99].

Visible and infra-red laser radiation interacts with tissues mainly through absorption which is facilitated by chromophores (parts of molecules responsible for absorption of light). In the human body major chromophores are melanin, hemoglobin (blood), and water[100, 101]. Laser-tissue interactions in medical applications can be divided into two groups based on the level of absorption; low penetration at a wavelength where absorption

is high and deep penetration at a wavelength where absorption is low[101]. As examples for the low penetration cases, KTP (frequency-doubled Nd:YAG) emitting green light at 532 nm exploits high absorption by hemoglobin, and CO_2 laser (10.6 μm), Er:YAG laser (2.94 μm) and two-micron lasers utilize the high absorption by water. On the other hand, Nd:YAG laser (1.064 μm) and diode lasers (808-980 nm range) are examples for the deep penetration effect due to the low absorption of water.

In the mid-IR range, medical applications utilize thermal effects in tissues due to the absorption of laser radiation by the water content in the tissues. According to the intensity of the laser radiation and exposure time of the tissue, the following thermal effects occur in order of increasing tissue temperature: protein denaturing, coagulation (thermally killing pathological tissues without harming the healthy ones), necrosis (death of cells), collagen denaturing, desiccation (extreme drying), carbonization (burning), ablation (vaporization)[100]. Soft tissue (skin, prostate, cornea, etc.) ablation, a means for cutting and removing tissues, is a major application of lasers used in medical surgery. Ablation with mid-infrared lasers occur as confined steam bubbles form upon the heating up of tissue cells and these bubbles explode by tearing apart the tissues as temperature increases further[100]. In this surgical method, precise cutting and removal of the targeted tissues, minimal damage to the tissues surrounding the targeted area and very good hemostasis (termination of bleeding) are critical requirements. Ho-based lasers operating in the 2.1-2.15 μm range (mostly in the pulsed mode) have gained wide acceptance as tools for soft tissue ablation in various fields of medicine as a result of good confinement of the radiation facilitated by high absorption of water and excellent hemostasis. Although, CO_2 and erbium lasers are also effective tools for ablation, the commercially available low-OH silica fibers for transmitting 2-μm radiation with low loss favor Ho-based lasers in terms of compatibility with endoscopes[102]. Lasers that fulfill the requirements for soft tissue ablation (mentioned above) and fibers that transmit laser radiation in endoscopic channels with low loss are critical for minimally invasive (laparoscopic) surgery where the tube of

an endoscope is inserted into the body through a small incision (2-3 cm). In minimally invasive surgery, it has been established that holmium lasers produce rapid and precise tissue removal (ablation) and high degree of hemostasis compared to poorer ablating precision of Nd:YAG and often unstable surface hemostasis of CO_2 lasers[100, 101, 103]. For these reasons, Ho-based (especially Ho:YAG) lasers are widely used in urology for treatment of benign prostate hyperplasia (enlargement of the prostate), lithotripsy (breaking the stones in the kidney, ureter or bladder into small pieces), removal of bladder tumors and cutting (incision) of bladder-ureter strictures (narrowing of channels)[104]. To be more specific, in endourology (endoscopic urology), holmium laser prostatectomy (surgical removal of all or part of the prostate gland), going through the steps of bladder neck incision and resection (removal of a part) of the prostate (HoLRP), has evolved into enucleation (removal) of the prostate (HoLEP)[105, 106]. Researchers have shown HoLEP to be at least as effective as the standart technique of transurethral resection of the prostate (TURP)[107] and even to have some advantages over it[105]. Another example in endoeurology, holmium laser lithotripsy (stone treatment, stone fragmentation) has proven itself as a safe and effective method[108] which involves mainly thermal ablation (evaporation) leading to chemical decomposition of urinary stones[109, 110].

Although, presently holmium (Ho:YAG to be specific) lasers have the widest usage among lasers in urology, there are also some limitations related with their usage such that they still cause some damage to the surroundings of the targeted area in spite of the confined effect which, on the other side, limits the size of the target for ablation[111]. Further to the limitations of holmium lasers, which commonly operate in pulsed mode in medical applications, is that cw radiation is more suitable for soft tissue surgery as it provides a better control of tissue heating, higher degree of hemostasis, more precise and smoother incision[100, 101, 111, 112]. Also in lithotripsy with holmium laser, it can take very long in cases of large stones and there is a safety matter that should be taken into account in the case of stones of uric acid[111].

In addition to urology, percutaneous discectomy (removal of the leaking part of the vertebral disk, which is pressing on the spinal cord or nerves and causing pain, via a tube inserted through the skin) in neurosurgery, arthroscopic surgery (the examination and/or treatment of a damage inside a joint by a minimally invasive surgery), laser thermo keratoplasty (a refractive procedure to make the central cornea steeper) in ophthalmology, angioplasty (opening up of obstructed blood vessels) in cardiovascular surgery, are examples of surgical applications where holmium lasers have been put into clinical use[100].

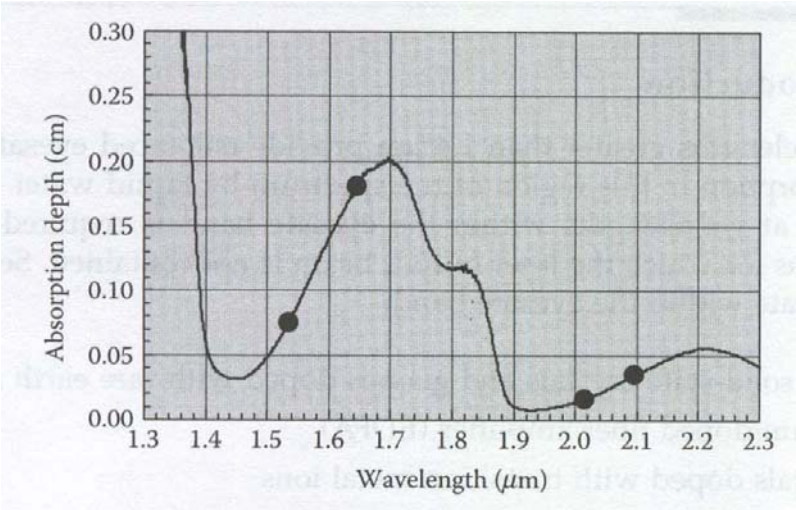

Fig. 2.9 Absorption depth of water in the 1.3-2.3 μm wavelength range[13].

Thulium based lasers operate in the 1.9-2.0 μm wavelength range where the absorption of water is even higher than the holmium based lasers because of the absorption peak in the 1.92-1.94 μm slot(see Fig. 2.9). To be more specific, the absorption depths of water (length at which 90% of incident radiation is absorbed) at output wavelengths of particular two-micron lasers are 0.35 mm at 2.097 μm of Ho:YAG, 0.16 mm at 2.015 μm of Tm:YAG, and 0.09 mm at 1.94 μm of Tm:YAlO laser[7, 13]. Considerably smaller

absorption depth results in a better confinement of radiation which means reduced damage to the surroundings of the targeted tissues and more precise cutting performance[113, 114]. Consequently, Tm-based lasers, which are in the clinical testing stage yet, are emerging as alternatives to Ho-based lasers in medical applications. Since laser diode pumped thulium lasers can be either operated in cw or pulsed mode in comparison to flash-lamp pumped pulsed holmium lasers in medical applications, most suitable mode of operation for the particular application can be chosen. Actually, superior or at least equivalent results compared to lasers currently in use (e.g. Ho:YAG, KTP) have been achieved in several clinical studies of soft tissue surgery with cw or pulsed thulium lasers[102, 112-116]. In earliest one of these studies[102], ablation by pulsed Ho:YAG and Tm:YAG lasers was tested in vitro on fresh chicken liver and guinea pig skin, the performance of the lasers was reported to be similar. In a later work by N. M. Fried, a 40 W Tm-fiber laser at 1.94 μm was used in cw mode to vaporize animal prostate tissue and in pulsed mode to cut animal ureter and bladder-neck tissues[113]. He concluded that the fiber laser operated more efficiently and cut tissues more precisely than Ho laser, but for clinical use, higher cw power for fast vaporization and shorter pulses for more precise incision of bladder-ureter strictures[113] were required. Subsequently, N. M. Fried and K. E. Murray demonstrated rapid vaporization and coagulation of dead prostate tissues from a dog with a higher power (110-W) cw thulium-fiber laser at 1.91 μm[116]. In another study, T. Bach et al used a two-micron cw Tm:YAG laser for simultaneous vaporization and resection (vaporesection) of the prostate (equivalent of HoLRP) to treat benign prostatic hyperplasia in 54 patients with a one-year follow-up[112]. The results indicated that the treatment was safe and effective[112]. Further, in a bladder neck incision (cutting) experiment with a cw 70 W Tm:YAG laser, Bach et al showed that the 2-micron laser provided smoother cutting than pulsed Ho:YAG, in a safe and quick manner[114]. In a very recently reported clinical study[115], G. Wendt-Nordahl et al systematically evaluated a cw thulium laser operating at 2.013 μm (Tm:YAG), testing tissue ablation and hemostasis on dead pig kidney at

different power levels of 30, 50, 60 and 70 W. In this work, the results were compared to ablation by 80-W KTP laser and TURP, the techniques accepted as standards in clinical use. The researchers concluded that the thulium laser removed tissues at a 1.5 times higher rate than KTP laser but at a significantly lower rate than TURP, and hemostasis level was similar to KTP with much lower bleeding compared to TURP[115].

2.8.2 Remote Sensing Applications

Lidar, which is the acronym for "Light Detection and Ranging", is the general name for remote sensing and range finding systems using lasers. Lidar (sometimes also called laser radar or Ladar) technology is based on detection of laser signals which are either absorbed or reflected or scattered by targets. Different techniques such as laser range finding, Doppler lidar, differential absorption lidar (DIAL) and differential scattering lidar (DISC) have been developed according to the specific application[117, 118]. Laser range finding involves measuring the distance of a target from the time it takes for a laser pulse launched on the target to be reflected back at the emitter. Doppler lidar technique has been developed for wind speed measurement or wind profiling based on the detection of Doppler shift in the backscattered laser signal from the aerosols in the atmosphere[118, 119]. This technique is used in sensing wind sheers (wind gradients) facing aircrafts which is very critical for pilots to prevent plane crashes[119]. DIAL and DISC systems are used for detection and monitoring of gasses, vapors and aerosols (suspended solid or liquid droplets in air) in the atmosphere or a specific environment[117]. For example, these systems are used for monitoring water vapor[120] and CO_2 concentration (an indicator of global warming) in the atmosphere which is vital for weather and climate studies. A DIAL system requires laser emission at minimum two wavelengths per targeted gas (or vapor, etc.), one absorbed and the other transmitted by the target[117]. These wavelengths should preferably be located in a transmission window free of absorption by constituents in the environment

other than the targeted gas or gasses. DISC technique, on the other hand, is based on differentiation of the target gas by scattering of different wavelengths from the target[117].

Eye-safe operating wavelength in a high transmission window of the atmosphere dominated by the absorption lines of water vapor, CO_2 and NO_2, compactness, reliability and long lifetime, have made two-micron solid state lasers attractive for ground-, aircraft-, and space-based lidars [12, 13, 56, 58, 118, 121-124]. Remote sensing applications further require lasers of high efficiency (to provide the power necessary for atmospheric measuremnts and the high pulse energy required for a space based Doppler lidar)[58, 85], long pulse (for a high resolution of the velocity of a target)[39, 125] and pulse repetition frequency of at least 10 Hz[83]. Such requirements have motivated the research to advance the two-micron lasers. As potential highly efficient coherent two-micron emitters, Ho:YAG (2.09 μm)[119, 123-126], Ho:LuAG (2.01 μm)[58, 127], Ho:YLF (2.06 μm)[56, 83], Ho:YSGG (2.09, 2.1 μm)[122] lasers have been developed and investigated for LIDAR systems. In addition, Tm:YAG[39, 45] and Tm:LuAG[45, 127] lasers have been considered for remote sensing applications and it has been indicated that the free running output of Tm:LuAG at 2.023 μm is in a higher and hence preferred atmospheric transmision window compared to 2.015 μm of Tm:YAG or 2.6-2.1 μm of Ho-doped lasers. Further, examples of commercially developed systems can be given such that a Doppler lidar based on a pulsed laser operating at 2.02 μm for sensing wind speed and producing a map of the wind field, and another one based on a Q-switched Ho:YAG laser for sensitive vibration measurement have been built by Coherent Technologies, Inc.(CTI)[118]. CTI has also been working on high-efficiency Ho:YAG and high power Tm:YAlO lasers for LIDAR applications[118].

2.8.3 Pumping of Other Solid-State Lasers

Two-micron lasers, especially Tm-doped systems, are also efficient pump sources for other mid-ir solid-state lasers and optical parametric oscillators (OPOs). First of all, the output wavelength range (1.94-1.98 μm) of free-running Tm:YAlO laser falls inside the

absorption range (1.5-2.5 μm)[128] of the widely tunable (1.88-3.1 μm)[129] and highly efficient mid-ir source Cr^{2+}:ZnSe laser. As a matter of fact, efficient operation of Cr^{2+}:ZnSe laser coherently pumped by Tm:YAlO laser has been demonstrated in several cases[117, 128, 130]. Second, as it was also discussed above in the review of two-micron lasers (Section 2.7) thulium-doped lasers are used as efficient in-band pump sources for Ho:YAG lasers[73, 75-82, 118, 131] which are important for medical and sensing applications. To recapitulate beriefly, cw Ho:YAG lasers intracavity pumped by Tm:YAG lasers[73, 75], cw and Q-switched Ho:YAG lasers end-pumped by Tm:YAlO[79, 118] lasers have been demonstrated. Also, recently there has been a lot of interest in Ho:YAG lasers pumped by cw diode-pumped Tm:YLF lasers operating at 1.91 μm, in end-pumped configuration[79-81, 131], intracavity end-pumped[76] and intra-cavity side-pumped[77, 78] geometries. Third and finally, researchers have demonstrated efficient mid-ir OPOs based on $ZnGeP_2$ (ZGP) crystal generating 3-5 μm radiation pumped by Q-switched Ho:YAG[131, 132] and Tm:YAlO[94, 133] lasers. In addition very recently, a mid-ir ZGP OPO pumped by Q-switched Tm:YAG[134] laser and mid-ir orientation-patterned GaAs (OP-GaAs) OPO pumped by a Q-switched Ho:YAG[135] laser have been presented.

Chapter 3

STUDY OF CW Tm^{3+}:$YAlO_3$ LASERS

3.1 Introduction

Tm^{3+}: $YAlO_3$ (Tm:YAP or Tm:YAlO) laser is an efficient source of two-micron radiation with a free-running output in the 1.94 -1.99 μm range which overlaps with the absorption peak of water (see Fig. 2.8 and 2.9). As discussed in the previous chapter (Section 2.8a), absorption by water in the tissues is mainly responsible for the thermal effects that occur during the interaction of infrared radiation with biological tissues, hence this laser holds an important potential for medical surgery. The high water absorption at 1.94 μm and tunability in the 1.9-2 μm range also make this laser attractive for applications in spectroscopy as well as atmospheric/chemical sensing (see Section 2.8b). It is further a useful pump source for solid-state lasers such as Ho:YAG[79, 118], Cr^{2+}:ZnSe[128, 136] (also see Section 2.8c) .

In the Tm^{3+}: $YAlO_3$ laser crystal, Tm^{3+} ions replace Y^{3+} ions in the crystal host yttrium orthoaluminate (YAP or YAlO). Similar to the YAG host, the YAP crystal has the advantages of high mechanical strength and large heat conductivity (0.11 W/cm-K in YAP vs. 0.13 W/cm-K in YAG)[137], which allow high-power operation with reduced risk of fracture. Additional favorable features of this system include the availability of high-power pump diodes that overlap with the absorption band of the crystal near 800 nm, enhanced pumping efficiency through cross relaxation, broad tunability around 2μm, and polarized laser emission due to the biaxial nature of the YAP host. To date, extensive studies have been carried out to investigate the spectroscopic and lasing properties of Tm:YAP. In

spectroscopic studies, the absorption and emission spectra were analyzed to determine the energy-level structure [138], oscillator strengths, emission cross sections, non-radiative decay rates, the luminescence quantum efficiencies and upcoversion[4, 6, 139, 140]. In lasing experiments, flashlamp-pumped[5, 6], continuous-wave (cw) Ti:sapphire-pumped[7] diode-pumped[8, 47, 48, 93, 94, 141-144], stabilized cw[145] and Q-switched[96] operations have been demonstrated with Tm:YAP gain media. In cw operation, output powers of as high as 50 W[96] and tunability in the 1.9-2.3 μm range have been reported[98, 144]. Further, researchers have performed modeling studies of Tm:YAP lasers in cw diode-pumped diode-pumped configuration[143], and analysis and experimental investigation of Tm:YAP microlasers [146, 147].

In this chapter, two experimental studies on CW Tm:YAP lasers will be covered: influence of doping concentration on the power performance of diode-pumped laser operation[148] and low-threshold operation of the laser pumped by a Titanium:sapphire-laser[97].

3.2 Influence of Doping Concentration on the Performance of Diode-Pumped CW Tm^{3+}:$YAlO_3$ Lasers

One of the crucial factors that affect the power performance of Tm:YAP lasers is the doping concentration. Varying the active-ion concentration can change the strength of cross relaxation, reabsorption losses, and non-radiative decay rates. Cross relaxation process produces two photons near 1800 nm for one pump photon (arrows marked 2 in Fig. 2.6) and increases the power efficiency of the laser. Thulium ions need to be in close proximity in order to increase the strength of cross relaxation, which means that the doping concentration should be relatively high. In most of the previous studies, samples with a thulium concentration of 3-4 % have been used to increase the pumping efficiency via cross relaxation. While cross relaxation contributes positively to output efficiency by boosting the upper laser level population, higher doping concentrations (for the same

crystal length) lead to more reabsorption due to the quasi-three-level nature of the Tm:YAP medium and faster non-radiative decay resulting from energy migration between thulium ions. In both cases, higher inversion threshold is required to achieve transparency. One therefore expects that an optimum doping concentration exists that maximizes the efficiency of the laser. It is important to note that the optimum concentration will also depend on the laser geometry used, in particular, on whether the crystal is single-end-pumped or excited from both ends, the latter enabling low lasing thresholds even in the presence of reabsorption. In earlier studies, Kintz investigated the effect ion concentration of the power performance of 2-μm Tm:YAG lasers [149]. However, to the best our knowledge, no such study has been carried out with Tm:YAP lasers.

In this study, we considered continuous-wave, diode single-end-pumped Tm:YAP lasers operating in the low- to medium-power range and investigated the influence of the thulium ion concentration on the laser power performance[148]. Three samples with 1.5%, 3%, and 4% Tm^{3+} concentration were examined at 18^0C. Lifetime and fluorescence measurements were also performed to assess the effect of concentration on the strength of cross relaxation and non-radiative effects. Our results showed that the best cw power performance was obtained with the sample having 1.5% Tm^{3+} concentration. By using 9.5 W of incident pump power at 797 nm, a maximum of 1430 mW of output power was obtained with a 2% output coupler. The laser performance of the samples degraded monotonically with increasing thulium concentration due to increases in reabsorption losses, non-radiative decay, and internal heating. Spectroscopic measurements and rate-equation analysis further suggested that cross relaxation should already be effective in samples with 1.5% Tm^{3+} ion concentration. The average value of the effective gain cross section at 1.94 μm was determined to be $4.2x10^{-21}$ cm^2 in good agreement with previous results[7, 150].

3.2.1 Experiment

In the laser experiments, we used three different Tm:YAP crystals with 1.5%, 3%, and 4% Tm^{3+} concentration. The crystals were commercially purchased (1.5% Tm:YAP crystal from Crytur, Inc., and 3% and 4% Tm:YAP crystals from Scientific Materials, Inc.). The dimensions, corresponding thulium ion concentration in cm^{-3}, total absorption (η_a), and the small-signal pump absorption coefficient (α_p) at 797 nm of each sample are given in Table 3.1. The thulium ion concentrations were determined by assuming a density of 5.35 gm/cm^3 for YAP [151]. All the crystals were normal cut and both faces had anti-reflection coatings at 1940 nm. The pump as well as the laser beams propagated along the crystal a-axis.

Table 3.1

Properties of the Tm:YAP crystals used in the laser experiments

Tm^{3+} Conc.		Dimensions*	Total Absorption η_a	Absorption Coeff. α_p
(at. %)	(10^{20} cm^{-3})	(mm)		(cm^{-1})
1.5	2.95	Cylindirical 5x4	0.56	2.06
3	5.90	Cubic 4x4x2	0.57	4.24
4	7.86	Cubic 4x4x2	0.64	5.17

*Last dimension gives the length of the crystal.

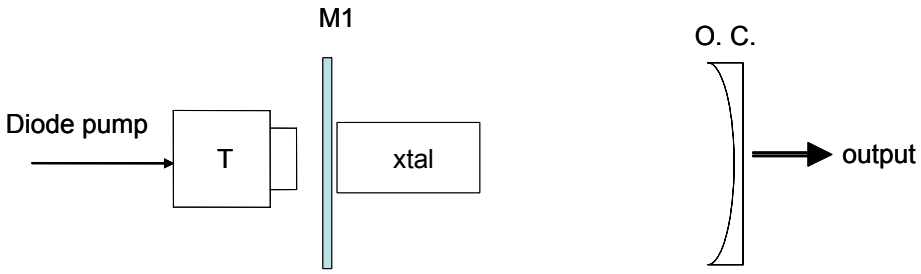

Fig. 3.1. Schematic of the laser setup.

The schematic of the experimental setup is shown in Fig. 3.1. The resonator consisted of a flat input mirror (M1) and a curved output coupler (OC) with a radius of 10 cm. M1 was highly reflective around 1.94 μm and highly transmitting at 795 nm. The Tm:YAP crystals (xtal) which were positioned near M1, were wrapped in indium foil and held between copper holders maintained at 18 ^{0}C. Output couplers with 2% and 6% transmission were used in the power measurements. The resonator length was 7.5 cm, giving an estimated 160-μm beamwaist inside the crystal. The Tm:YAP resonator was end-pumped with a fiber-coupled diode array operating at a wavelength of 797 nm. An imaging telescope (T) was used to focus the pump beam into the crystal. By using the knife-edge technique, the measured beamwaist and the M^2 of the pump were determined to be 382μm and 319, respectively. The Tm:YAP samples were characterized up to a maximum incident pump power of 9.5 W. For each crystal-output coupler combination, the output wavelength of the laser was also measured with a 0.25 m monochromator.

The three laser samples and a fourth Tm:YAP crystal with 5% Tm^{3+} concentration (absorption coefficient= 5.89 cm^{-1}, Crytur, Inc.) were used in the spectroscopic studies. Lasing characterization was not attempted with the 5% Tm:YAP sample due to the presence of internal fractures inside the crystal. In fluorescence measurements, samples were excited with a cw diode laser at 785 nm. The excitation beam propagated along the a-

axis of the crystals. The intensity of the 785-nm pump was 1.65 W/cm^2, much smaller than the 380-kW/cm^2 saturation intensity for the $^3H_6$-$^3H_4$ transition (absorption cross section= $6.7x10^{-21}$, and approximate lifetime=100 μs), indicating that intensity-dependent effects were negligible in the fluorescence spectra. The emitted fluorescence was filtered through a 0.5 m Czerny-Turner-type monochromator and the relative intensities of the 1470-nm ($^3H_4$->$^3F_4$ transition) and 1800-nm ($^3F_4$->$^3H_6$ transition) bands were measured with a PbS detector and a lock-in amplifier to evaluate the strength of cross relaxation. The fluorescence spectra were not corrected for the spectroscopic system response. The estimated change in the system responsivity between 1470 and 1900 nm (due to the wavelength dependence of the PbS detector and the diffraction gratings) was less than 15%. Due to the biaxial nature of the YAP crystal, the emission spectra of Tm^{3+} are in fact polarization-dependent. In our experiments, only the unpolarized emission spectra were measured to provide a qualitative comparison of the relative band intensities at different concentrations. In lifetime measurements, samples were excited with a 790-nm pulsed Ti:sapphire laser generating 70-ns pulses. The lifetimes of the $^3H_4$ and $^3F_4$ levels were measured by operating the Ti:sapphire laser at repetition rates of 100 and 1000 Hz, respectively. As an example, Fig. 3.2 shows the time-dependent fluorescence decay (the constant background was subtracted) from the $^3F_4$ state for the 3% Tm:YAP sample. Exponential fit to the tail of the decay curve gave a best-fit value of 4.66 msec for the lifetime. In this case, the excitation pulse energy (220 μJ) was adjusted to be much smaller than the saturation energy of 74 mJ for the $^3H_6$-$^3H_4$ transition (absorption cross section= $6.7x10^{-21}$ cm^2 and pump radius= 250 μm) to minimize intensity-dependent effects in lifetime measurements.

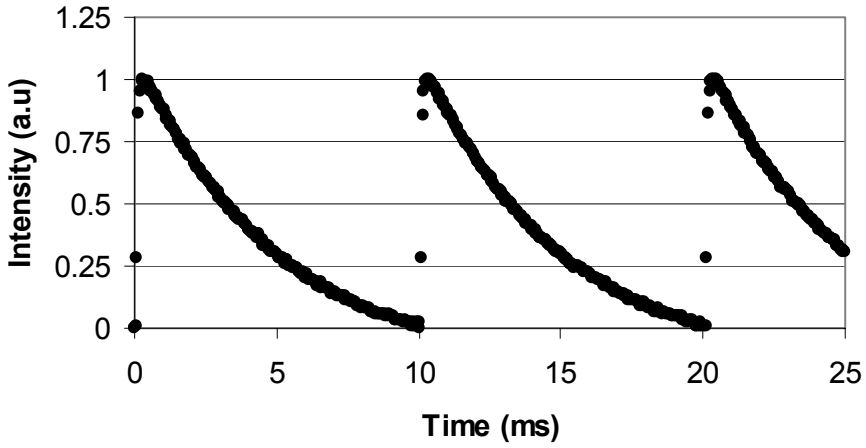

Fig. 3.2. Fluorescence decay curve of the $^3F_4$ state for the 3% Tm:YAP sample.

3.2.2 Results and Discussion

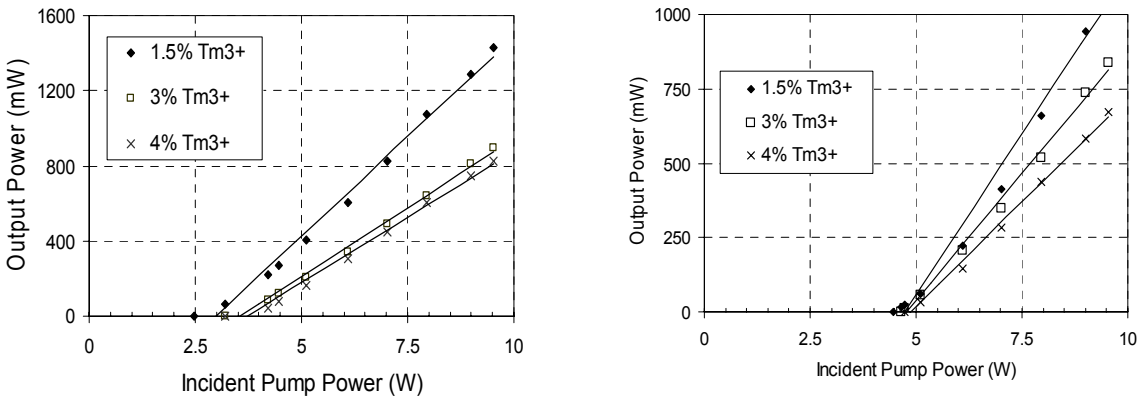

Fig. 3.3. Efficiency curves of the Tm:YAP laser with (a) 2% and (b) 6% output coupler and with samples containing 1.5, 3, and 4% Tm^{3+} ion concentration

Figs. 3.3(a) and (b) show the measured power efficiency curves of the Tm:YAP laser for the three samples with the 2% and 6% output couplers, respectively. The best power performance was obtained by using the 1.5% Tm:YAP crystal and the 2% transmitting output coupler. In this case, a maximum of 1430 mW of output power was obtained with 9.5 W of pump, representing an optical-to-optical conversion efficiency of 15%. The measured threshold pump power and the slope efficiency with respect to incident pump power were 2.47 W and 21.1%, respectively. For both output couplers, the performance of the laser degraded with increasing thulium concentration. For example, with the 2%-transmitting output coupler, the slope efficiency decreased from 21.1% in the case of the 1.5% Tm:YAP crystal to 13.9% for the 4% Tm:YAP sample with a corresponding increase in the threshold pump power from 2.47 W to 3.60 W. Similar results were obtained with the 6% output coupler. The output wavelength of each configuration was also measured in the experiments. As was thoroughly analyzed in Ref.[7], the output wavelength of the free-running laser depends on the amount of passive loss in the resonator and jumps from 1.99 μm at low levels of loss to 1.94 μm as the loss is increased. A similar trend was observed in our experiments. For the resonator containing the 1.5% Tm:YAP crystal and the 2% output coupler, the output wavelength of the laser was measured to be 1.99 μm. All of the other crystal-output coupler combinations produced laser radiation at 1.94 μm. In the case of the 1.5% Tm:YAP sample, beam divergence measurements were also performed with the knife-edge method. At an output power of 1W, the M^2 factor of the laser output was measured to be 1.05. Lastly, we note that higher slope efficiencies were obtained in the experiments described in Refs[7, 96, 141]. . It should be possible to increase the output powers obtained in our experiments by improving the mode matching of the pump and the laser beams and by cooling the laser crystal. Also, the pump wavelength at 797 nm might be another reason for low efficiency, since the absorption peaks of Tm:YAP are very narrow and occur around 795 nm for b-polarization and 793 nm for c-polarization[7].

The power measurements suggest that cross relaxation may already be effective in the case of the 1.5% Tm:YAP sample since the slope efficiency of the laser did not increase going from 1.5% Tm:YAP to 4%Tm:YAP samples. We employed spectroscopic methods to investigate this issue further. First, a rate-equation approach was used to calculate the relative intensities of the 1470-nm and 1800-nm bands in Tm:YAP at low thulium concentrations. Second, the fluorescence spectra of the crystals used in this study were measured in the 1200-2200 nm range and compared with the calculations. The variation in the relative intensities of the 1470-nm and 1800-nm bands with concentration provides a useful measure for the strength of cross relaxation. If cross relaxation becomes dominant with increasing thulium concentration, the non-radiative decay from $^3H_4$ to $^3F_4$ level also increases, and one expects the intensity of the 1470-nm band to decrease with respect to that at 1800-nm. At low thulium concentrations, the time evolution of the population densities n_1, n_2, n_3, and n_4, in the respective manifolds $^3H_6$, $^3F_4$, $^3H_5$, and $^3H_4$, can be calculated from

$$\begin{aligned} \frac{dn_4}{dt} &= R_p - w_{41}n_4 - w_{42}n_4 - w_{43}n_4 \\ \frac{dn_3}{dt} &= w_{43}n_4 - w_{32}n_3 - w_{31}n_3 \\ \frac{dn_2}{dt} &= w_{42}n_4 + w_{32}n_3 - w_{21}n_2 \end{aligned} \quad , \tag{3.1}$$

where R_p is the pumping rate and w_{ij} is the total decay rate (including the non-radiative phonon-assisted decay rate at low thulium concentrations and the radiative decay rate A_{ij}) from the i^{th} to the j^{th} manifold. Note that

$$n_1 + n_2 + n_3 + n_4 = N \, , \tag{3.2}$$

where N is the total Tm^{3+} ion concentration. Fluorescence power at 1470 nm is due to the radiative emission of photons after the ions decay from the $^3H_4$ to the $^3F_4$ manifold and is

given by $A_{42}n_4 h\nu V$ (A_{42}= radiative decay rate from $^3H_4$ to $^3F_4$, hν is the average energy of the emitted photon, and V is the pumped volume). A similar expression can be written for the fluorescence power at 1800 nm. After solving for the population densities in steady state, the intensity ratio of the 1470-nm and 1800-nm bands is given by

$$\frac{I_{1470}}{I_{1800}} = \frac{1800}{1470}\frac{A_{42}}{A_{21}}\frac{n_4}{n_2} = \frac{1800}{1470}\frac{A_{42}}{A_{21}}\frac{w_{21}}{w_{42} + w_{43}\dfrac{w_{32}}{w_{32} + w_{31}}}. \tag{3.3}$$

Radiative decay rates and branching ratios were reported in earlier spectroscopic studies for Tm:YAP[4, 6]. The non-radiative multi-phonon decay rates w_{ij}^{nr} were calculated by using the formula[6]

$$w_{ij}^{nr} = B\exp(-\alpha E_{ij})\left\{1 + \left[\exp\left(\frac{E_p}{kT}\right) - 1\right]^{-1}\right\}^{E_{ij}/E_p}, \tag{3.4}$$

Here, k is Boltzmann's constant, T is the absolute temperature, E_{ij} is the energy difference of the manifolds i and j, and the parameters B, α, and E_p have the respective values of $6.5\text{x}10^9$ sec^{-1}, $4.7\text{x}10^{-3}$ cm, and 600 cm^{-1} for Tm:YAP[6]. I_{1470}/I_{1800} comes to 0.48, indicating that at low thulium concentrations, the intensity of the 1470-nm band is about half as large as that of the 1800-nm band. Similarly, measurements performed in other hosts also show that the intensity of the 1470-nm band can be comparable with that at 1800 nm at low doping concentrations(See for example Refs.[65, 152]). The results of our fluorescence measurements taken with the four Tm:YAP samples are shown in Figs. 3.4(a)-(d). Note that in all of the spectra shown in Fig. 3.4, the 1470-nm band is very weak compared to the 1800-nm band. Though qualitative, these fluorescence measurements suggest that even in the case of the 1.5% Tm:YAP sample, the thulium concentration may be sufficiently high for cross relaxation to occur. As a result, the non-radiative decay rate

from $^3H_4$ to $^3F_4$ level increases and the relative intensity of the 1470-nm band becomes very small. Also note that the 1470-nm band completely disappears in the case of the 5% Tm:YAP sample. However, in this case, non-radiative decay from the $^3F_4$ to $^3H_6$ level also intensifies as can be seen from the lifetime measurements in Fig. 3.5. In particular, note that the lifetime of the $^3F_4$ level shows a monotonic decrease with thulium concentration, the reduction becoming most pronounced in the case of the 5%Tm:YAP sample. There is an accompanying decrease in the lifetime of the $^3H_4$ level from 142μs to 21μs going from 1.5 to 5 % Tm^{3+} concentration due to cross relaxation. The decrease of the fluorescence

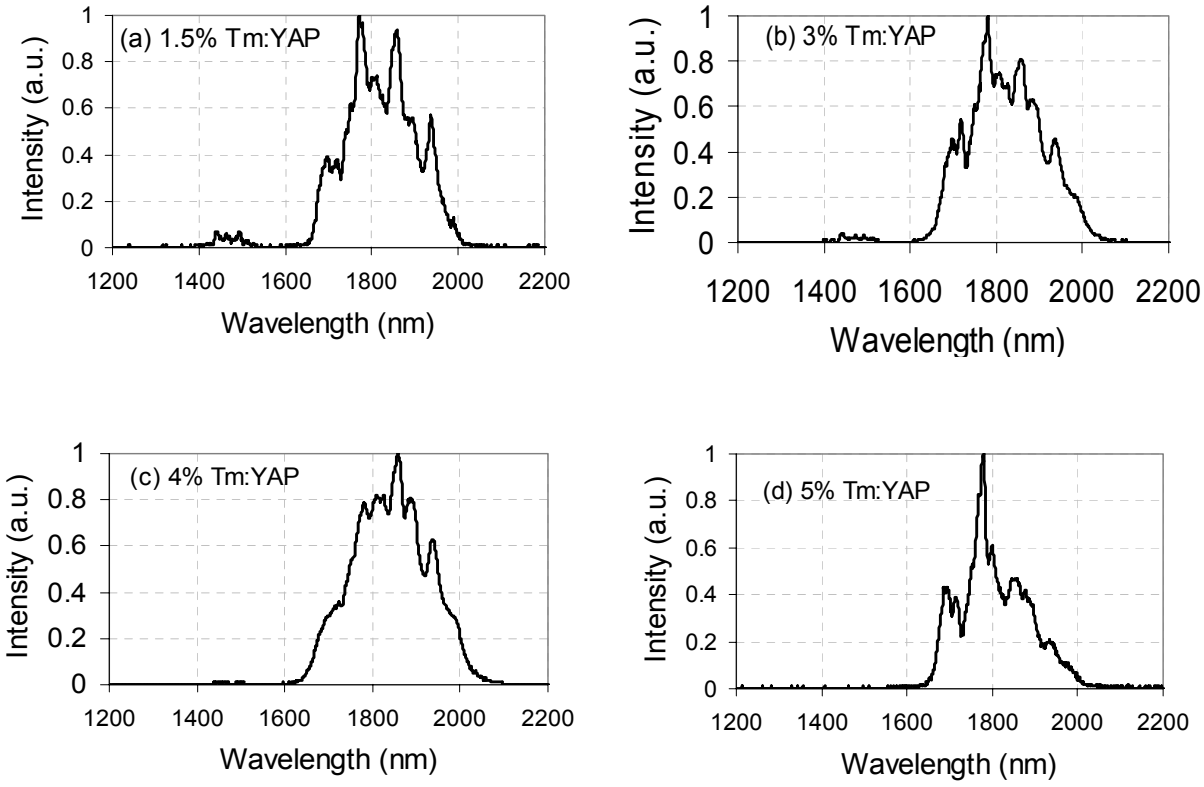

Figure 3.4. Fluorescence spectra of the Tm:YAP samples with (a) 1.5%, (b) 3%, (c) 4%, and (d) 5% Tm^{3+} ion concentration.

lifetimes with concentration may also be due to impurities. However, it is beyond the scope of this thesis to characterize the amounts and the types of impurities (if any) that may be present in the samples.

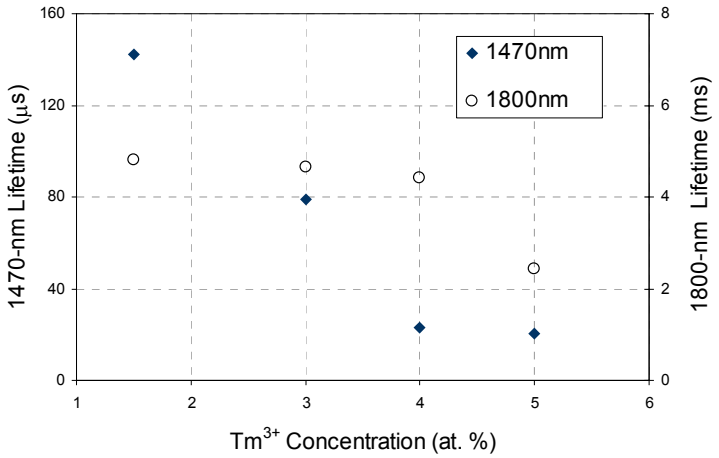

Fig. 3.5. Measured variation of the fluorescence lifetimes of the $^3F_4$ and $^3H_4$ levels as a function of thulium concentration.

The laser efficiency data were also used to determine the effective gain cross section $f_2\sigma_L$ (f_2=upper laser level occupation fraction, σ_L=gain cross section) from the measured laser efficiency data by using Eqn. (2.19) for incident threshold pump power in the case of quasi-three level lasers (see Section 2.6). First, threshold data taken with 2% and 6% output couplers were used to determine the total loss $L+2Nlf_1\sigma_L$ at 1.94 μm. Note that the threshold data for the 1.5% Tm:YAP sample were not initially used since the wavelength shifts from 1.99 to 1.94 μm, when the output coupler is changed from 2 to 6%. In the case of the 3% Tm:YAP sample, for example, the total round-trip loss of the resonator was determined to be 8.1%. By using the calculated round-trip loss factor in Eq.

(2.19), the effective emission cross section $f_2\sigma_L$ was determined to be $4.1\text{x}10^{-21}$ cm^2 at 1.94 μm for the 3% Tm:YAP sample. In these calculations, the pump and laser spot sizes were averaged over the crystal length by assuming that the beam waists are located near the center of the crystal. Also, the measured fluorescence lifetime was used for each sample. Table 3.2 summarizes the results of the laser measurements and lists the values of the threshold pump power P_{th}, slope efficiency η_s, calculated round-trip total loss $L+2Nlf_1\sigma_L$, and the effective gain cross section $f_2\sigma_L$ for different thulium concentrations and output coupler transmissions T. As can be seen from Table 3.2, the average value of the effective gain cross section at 1.94 μm came to $4.2\text{x}10^{-21}$ cm^2, in good agreement with what was reported in Refs[5, 7, 150]. In the case of the 1.5% Tm:YAP sample, the round-trip loss of the resonator was determined by comparing the threshold pump powers of the 3% and 4% Tm:YAP samples with that of the 1.5%Tm:YAP for the resonator with 6% output coupler. Using the laser data for the 6% output coupler ensures that the operating wavelength (1.94 μm) and hence the effective cross section are the same. Differences in the measured lifetime and total crystal absorption were taken into account. This yielded an average round-trip loss value of 7.7% (see Table 3.2). As expected, the total round-trip loss $L+2Nlf_1\sigma_L$ of the resonator is nearly the same (7.7% versus 8.1%) for the samples containing 1.5% and 3% Tm^{3+} concentration since the quantity $2Nlf_1\sigma_L$, which accounts for reabsorption loss, should remain unchanged when N is doubled and l is halved for the same value of $f_1\sigma_L$. The Tm:YAP sample with 4% doping concentration suffers from larger reabsorption losses compared with the 3% doped sample (see Table 3.2). Finally, the inversion threshold ΔN_{th} required to obtain lasing can be estimated from Eqn. (2.23) (see Section 2.6) By using Eq. (2.19) and the measured laser threshold data, ΔN_{th} is determined to be $1.5\text{x}10^{19}$ and $2.1\text{x}10^{19}$ cm^{-3} for the 3% Tm:YAP sample with the 2% and 6% output couplers, respectively.

Table 3.2

Measured values of the laser threshold pump power P_{th}, slope efficiency η_s, total round-trip resonator loss $L+2Nlf_1\sigma_L$, fluorescence lifetime τ of the upper laser level ($^3F_4$), and the effective gain cross section $f_2\sigma_L$ for different thulium concentrations and output coupler transmissions (T).

Tm^{3+} Conc. (at. %)	T	P_{th} (W)	η_s (%)	$L+2Nlf_1\sigma_L$ (λ=1.94μm) (%)	τ (ms)	$f_2\sigma_L$ (10^{-21} cm^2)
1.5	2%	2.47	21.1	7.7	4.82	
	6%	4.47	21.7			
3	2%	3.20	14.3	8.1	4.66	4.1
	6%	4.47	17.1			
4	2%	3.60	13.9	10.6	4.42	4.3
	6%	4.74	14.2			

In addition to the increase in reabsorption losses and non-radiative decay rates, higher internal heating is another possible factor responsible for the degradation of power performance with increasing thulium ion concentration. To assess the strength of this effect, we estimated the average axial temperature rise for the different Tm:YAP samples. In the temperature calculations, the heat equation was solved analytically in cylindrical coordinates. The heat load due to the unused pump was assumed to be constant within a cylinder whose radius is equal to the average pump spot size inside the crystal and longitudinal heat conduction was neglected [153-155]. The heat conductivity of the YAP medium was taken as 0.11 W/cm-K[151] and cross relaxation was assumed to double the quantum efficiency. Our calculations show that at the maximum pump power of 9.5 W, the average axial temperature rise is 9, 16, and 19^0C for the samples with 1.5, 3, and 4% doping concentration, respectively. This leads to an increase in the minimum fractional

inversion F (see Eq, (2.18) in Section 2.6) required to reach transparency in the quasi-three-level medium[13].

We calculated the variation of F as a function of temperature by using Boltzmann statistics and the energy level structure of Tm:YAP [138]. The results are shown in Fig. 3.6 for emission at 1.94 μm. By assuming a crystal boundary temperature of 18^0C, F is calculated to be 0.087, 0.091, and 0.093 for the temperature rise of 9, 16, and 19 ^{0}C, respectively, showing that higher internal heating will also contribute to the degradation of the power performance with increasing concentration.

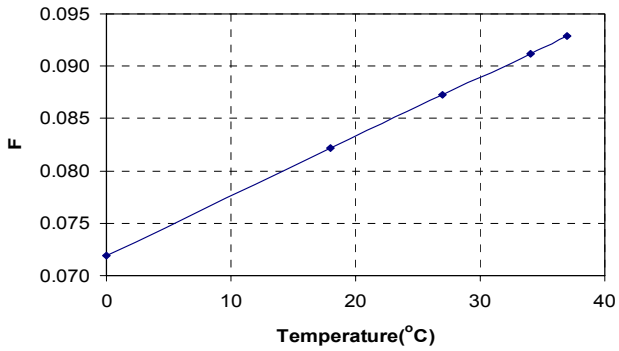

Fig. 3.6. Calculated variation of the fractional inversion F as a function of temperature.

3.2.3 Summary

We provided a detailed investigation of the cw power performance of diode single-end-pumped Tm:YAP lasers as a function of thulium ion concentration. Samples with 1.5, 3, and 4% doping concentration were pumped at 797 nm with a fiber-coupled diode laser and power efficiency measurements were made by using 2% and 6% output couplers. The best power performance was obtained with the 1.5% Tm:YAP sample with a maximum cw output power of 1430 mW at 9.5 W of incident pump power. The average gain cross-

section value of $4.2x10^{-21}$ cm^2 determined from the power efficiency measurements agrees well with the previously reported values[7, 150]. We identified increases in reabsorption losses, non-radiative decay rates, and internal heating as the major factors that cause the degradation of power performance with increasing thulium ion concentration. In this work, the laser performance of Tm:YAP crystals with more than 4% Tm^{3+} concentration was not experimentally investigated. However, spectroscopic measurements and rate-equation analysis suggest that cross relaxation may already be effective in samples with 1.5% Tm^{3+} ion concentration and that in single-end-pumped configurations, use of crystals with more than 4% doping concentration may cause degradation in laser performance due to higher reabsorption losses and faster non-radiative decay rates.

3.3 Low-threshold CW Tm:YAP laser

Development of low-threshold solid-state lasers, with the goal of making cost-effective and less power consuming systems has attracted a great deal of attention in recent years[156-162]. In order to reduce the threshold pump power, both the pump and the laser beams need to be tightly focused inside the gain medium. This further requires short crystals with lengths comparable to the confocal parameter of the pump. Furthermore, higher doping levels are typically necessary to have sufficient pump absorption over short interaction lengths. Most studies investigating low-threshold operation of solid-state lasers have so far been limited to those operating in the near infrared[158, 160].

In this study, we achieved low-threshold operation of cw Tm^{3+}:$YAlO_3$ (Tm:YAP) laser at room temperature**[97]**. Threshold pump powers in the 10 to 20 mW range were obtained by using a z-cavity, pumped by a cw Ti:sapphire laser. Two alternative cavity geometries were tested to investigate the role of mode matching. The first configuration had curved high reflectors with 5-cm radius of curvature (R), whereas the second had R=10 cm high reflectors. In each case, both single and double-pumping were used and the best performance (threshold pump power= 11 mW) was obtained with R=10 cm mirrors and

double end-pumping. The experimental results were also compared with a theoretical model that accounted for the quasi 3-level nature of the gain medium. In general, reasonable agreement was obtained between the experimental results and theoretical predictions. In the case of the configuration with R=10 cm mirrors, the performance was further improved by optimizing the polarization direction of the pump beam with a half-wave plate. The incident threshold pump power of 10 mW, obtained in this case under double pumping, is, to the best of our knowledge, the lowest threshold power reported to date for cw Tm:YAP lasers. Finally, the cw laser could be tuned over a range of 150 nm from 1842 nm to 1994 nm.

3.3.1 Experimental

Figure 3.7 shows a schematic of the z-type laser cavity consisting of the Tm:YAP crystal placed midway between two focusing curved mirrors (M1 and M2), a high end reflector (M3), and a 2% output coupler (OC). The 2-mm-long Tm:YAP crystal had a Tm^{3+} concentration of 4 at. %, 4 mm x 4 mm cross section, and was normal-cut along the a-axis. The crystal had antireflection coating for 1940 nm on both faces. The small-signal single-pass absorption of the crystal at the pump wavelength of 795 nm was measured to be around 65% for the pump polarization approximately parallel to the crystal b-axis. The crystal was wrapped with indium foil and placed inside an aluminum holder maintained at 20º C by water cooling. Two different cavity geometries were tested in the experiments. In the first case, hereafter referred to as the R=5 cm cavity, both M1 and M2 had a radius of 5 cm and the focal length of the input focusing lens (L in Fig. 3.7) was 5 cm. In the second configuration (R=10 cm cavity), R=10 cm for both M1 and M2, and the focal length of L was 10 cm. M1 and M2 further had high transmission at 800 nm and high reflectivity in the 1800-2075 nm range. The coating range of the output coupler and M3 was from 1850 to 2050 nm. Each cavity configuration was symmetric with 30-cm and 90-cm arm lengths for

the R=5 cm and R=10 cm, cavities, respectively. For double end pumping, a gold retro-reflector (M4) with a 10.5-cm radius of curvature was used.

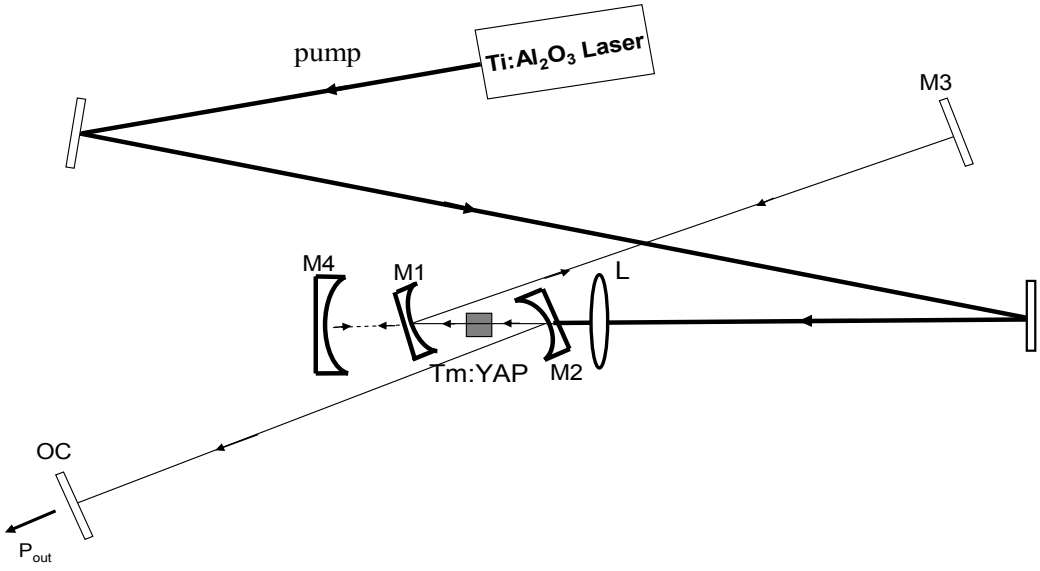

Fig. 3.7. Schematic of the continuous-wave Tm:YAP laser in z configuration.

The Tm:YAP laser was pumped at 795 nm by a cw home-built Ti:sapphire laser. The pump beam waist was measured with the knife-edge technique to be 5.2 μm and 11.9 μm for the R=5 cm and R=10 cm cavities, respectively. M^2 of the pump was 1.4 in each case. In the first part of the experiments, a comparative study of the two cavity configurations (R=10 cm and R=5 cm) was performed with the pump beam polarized parallel to the crystal b-axis. Then the polarization of the pump was optimized with a half wave plate to seek a further improvement in the best performance obtained in the first part.

The free running wavelength and tuning range of the laser were recorded with a ½-m Czerny-Turner-type monochromator. For the tuning measurement, a quartz birefringent tuning plate was inserted inside the R=10 cm laser cavity with the incident pump power set to 152 mW. With the insertion of the tuning plate, the output power of the laser decreased from 26 mW to 18 mW at the peak of the tuning curve.

3.3.2 Results and Discussion

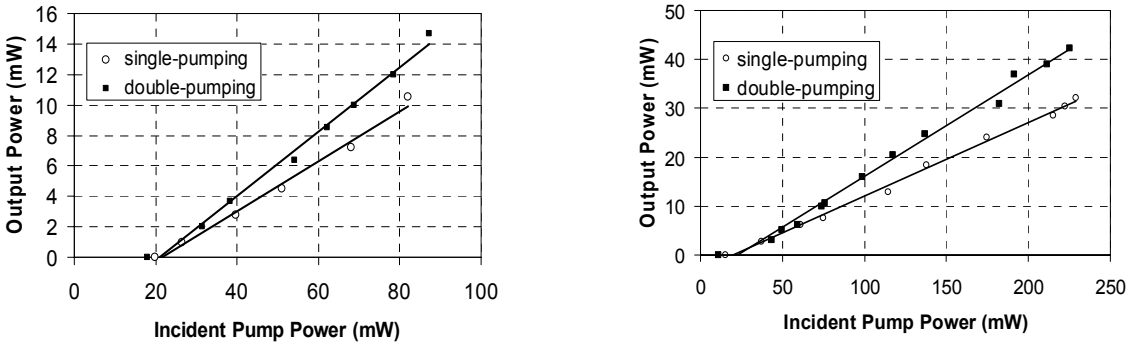

(a) (b)

Fig. 3.8. Power performance of the Tm:YAP laser for (a) R=5 cm cavity and (b) R=10 cm cavity with single and double end-pumping.

The laser operated at 1.945 μm in free-running mode and the output was polarized along the c-axis of the crystal. Figs. 3.8(a) and (b) show the power efficiency data with respect to the incident pump power for the R=5 cm and R=10 cm cavities, respectively. In each case, the pump beam was polarized approximately along the crystal b-axis. The threshold pump powers and the slope efficiencies η_s are given in Table 3.3. Clearly, the R=10 cm cavity showed superior performance with lower threshold powers in both single and double end-pumping configurations. Slope efficiencies were nearly equal for the two cases, suggesting the same amount of total resonator loss and comparable degree of mode overlap between

the pump and the resonator beams for both cavity geometries. The incident threshold pump power for the R=10 cm cavity decreased from 15 to 11 mW going from single to double pumping. A similar trend was observed for the R=5 cm cavity with relatively higher threshold powers.

Table 3.3

Summary of the continuous-wave threshold data for the R=5 cm and R=10 cm configurations[a].

	Single Pumping		Double Pumping	
Cavity Geometry	Threshold P_{th} (mW)	Slope Efficiency η_s (%)	Threshold P_{th} (mW)	Slope Efficiency η_s (%)
R= 5 cm	20	16	18	21
R=10 cm	15	15	11	21

[a] All data are in terms of incident pump power.

A comparative threshold analysis for the two cavity configurations was performed using Eqn. (2.19) for quasi three level systems (see Section 2.6). Note that, in the previous study discussed in Section 3.2 above, τ and $f_2\sigma_L$ (at 1.945 μm and for E parallel to the crystal c-axis) were determined to be 4.42 ms and 4.3 x 10^{-21} cm^2, respectively. From the analysis of the threshold data, the total round-trip resonator loss for both geometries was estimated to be 10.7%. The measured values for the pump spot size ω_p (5.2 μm and 11.9 μm for the R=5 cm and R=10 cm cavities, respectively,) were used. The double-pass absorption of the crystal was estimated from the measured single-pass absorption by assuming that the double-pumping mirror retro-reflected nearly 100% of the transmitted pump light.

Table 3.4

Parameter values used in the threshold analysis[a]

Parameter	R=5 cm cavity	R=10 cm cavity
τ (ms)	4.42	
$f_2\sigma_L$ (cm^2)	4.3×10^{-21}	
T (%)	2	
$L + 2Nlf_1\sigma_L$ (%)	10.7	
w_p (μm)[b]	21.3	14.9
w_L (μm)[b]	28	31
η_a (%) (single-pass)	0.67	0.63
η_a (%) (double-pass)	0.89	0.86
Results	**R=5 cm cavity**	**R=10 cm cavity**
P_{th} (mW) (single end-pumping)	24	24
P_{th} (mW) (double end-pumping)	18	18

[a]Calculated threshold powers are shown at the bottom. The analysis assumes that the laser is operated at the center of the stability range.
[b]Root-mean-squared values inside the crystal.

The laser mode spot size w_L was estimated from the ABCD analysis for each cavity geometry by assuming that the laser was operated near the center of the stability region. This would give the largest calculated threshold power since the beam waist is largest at the center of the stability curve. Furthermore, for a more accurate determination of the

expected threshold powers, rms spot sizes for both the pump and laser beams (w_P=21.3 μm and w_L=28 μm for the R=5 cm cavity and w_P=14.9 μm and w_L=31 μm for R=10 cm cavity) were used. By using Eq. (2.19), the incident threshold power was calculated to be nearly equal for the two cavity configurations: 24 mW for single end-pumping and 18 mW for double end-pumping. Although the R=5 cm cavity had tighter beam waist, larger diffractive spreading gave an rms spotsize comparable to that for the R=10 cm cavity. The parameters used in the threshold calculation and the results are listed in Table 3.4.

Comparing the measured and calculated threshold data, we see that experimentally achieved results for the R=10 cm cavity (15 mW for single pumping and 11 mW for double pumping) were lower than the theoretical predictions. This suggests that the laser could be fine-adjusted to an operating point somewhat away from the center of the stability region to reduce the resonator mode spot size and hence to lower the threshold. As a matter fact, setting w_L= 22 μm for the R=10 cm cavity yielded calculated thresholds of 15 mW and 11 mW for single and double pumping, respectively, predicting the measured values closely. On the other hand, for the R=5 cm cavity, the experimental threshold power (20 mW) is a little lower than the calculated one (24 mW) for single pumping, but equal to the calculated one for double pumping (18 mW). Normally, it is expected that the R=5 cm cavity can also be further optimized to lower the threshold, similar to the R=10 cm cavity. However, this was not possible in the experiments due to the high alignment sensitivity of this cavity. Note that the superior performance of the R=10 cm cavity is also indicated by the closer match between the crystal length (2 mm) and the pump confocal parameter (1.5 mm for R=10 cm cavity and 0.3 mm for R=5 cm cavity).

Fig. 3.9 shows the power efficiency curve of the double end-pumped R=10 cm cavity after the polarization direction of the pump beam was further optimized with a half wave plate. The incident threshold incrementally improved from 11 mW to 10 mW and the slope efficiency η_s increased from 21% to 25%. This enhancement in the laser performance is a consequence of the highly polarization-dependent nature of the absorption

coefficient of the Tm:YAP crystal[7]. It is shown in Figure 2 of the work by Stoneman et al. that at 795 nm, the absorption coefficient peaks sharply for pump polarization along the crystal b-axis and becomes nearly four times larger than that for the c-axis[7]. In our case, the pump beam propagates along the a-axis of the crystal with polarization approximately along b-axis and the half wave plate is used to fine-tune the polarization direction to optimize the efficiency of the Tm:YAP laser. Since $\eta_s \alpha \eta_a$ and $P_{th} \alpha \frac{1}{\eta_a}$ with all the parameters of the laser remaining fixed in such a case, a 19% increase (from 21 to 25%) in η_s would imply a 19% increase in η_a. This in turn would require a 19% reduction of the threshold from 11 to 9.5 mW, which, agrees well with our experimental result of 10 mW.

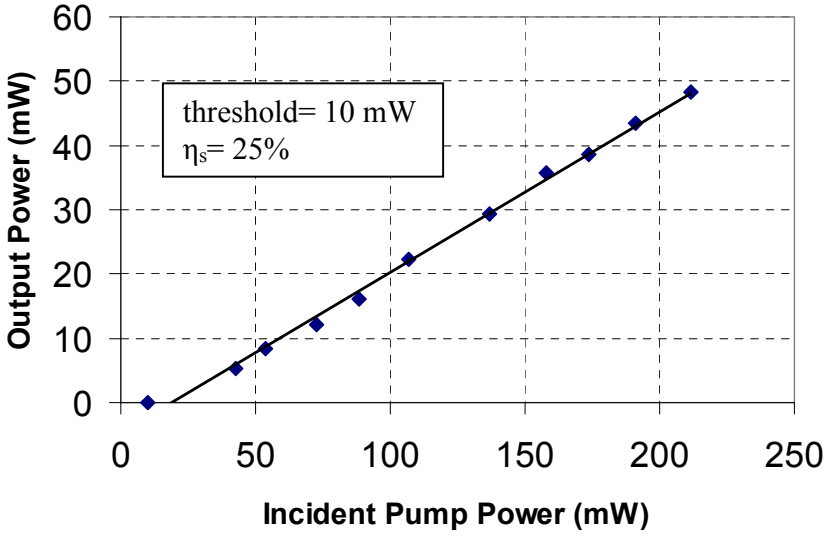

Fig. 3.9. Power performance of the Tm:YAP laser for R=10 cm cavity with double end-pumping after optimizing the pump beam polarization.

The tuning curve of the laser is shown in Fig. 3.10. The tuning range covers more than 150 nm from 1842 nm to 1994 nm which agrees reasonably well with that predicted

by the laser threshold versus wavelength curves shown in Fig. 4 of Ref. [7]. The measured tunability is also similar to that of the diode-pumped Tm:YAP lasers reported by Li et al. [98], except for a shift of about 50 nm, and Cerny et al.[144], except for the protrusion in the 1990-2035 nm range.

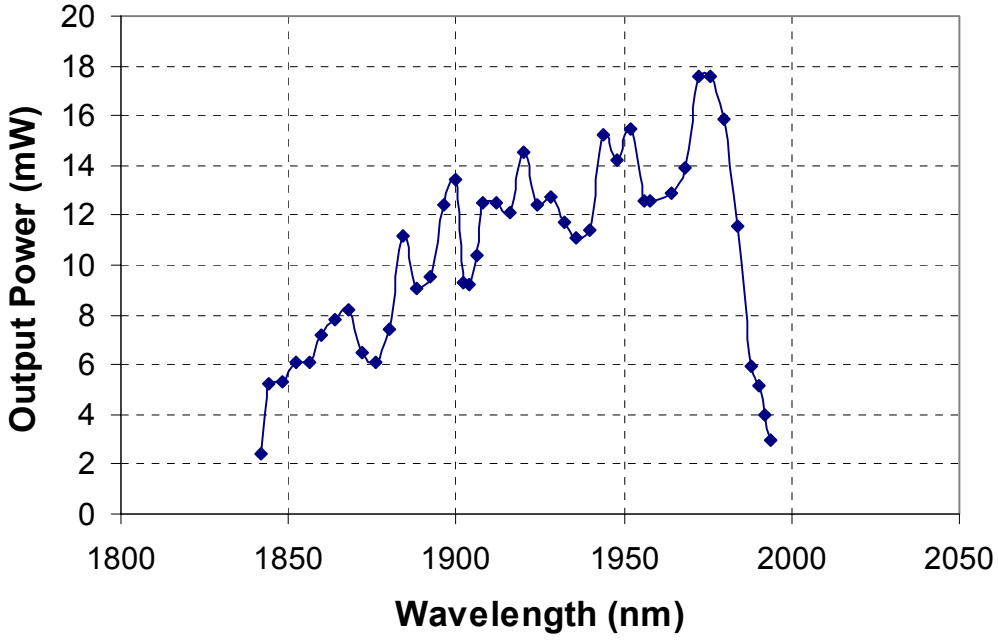

Fig. 3.10. Measured variation of the output power as a function of the emission wavelength.

3.3.3 Summary

We have described a continuous-wave Tm:YAP laser which can be operated at 1945 nm with threshold pump powers as low as 10 mW. The output could be tuned in the 1842-1994 nm range. Two alternative cavity geometries with R=5 cm and R=10 cm mirrors were tested. When the pump polarization was approximately parallel to the crystal b-axis, R=10

cm configuration yielded a lower pumping threshold. Each configuration produced nearly the same slope efficiency, suggesting that the amount of total resonator loss and the degree of mode overlap between the pump and the resonator beams were similar. A theoretical calculation assuming operation at the center of the stability range predicted nearly equal threshold powers for the two configurations. However, alignment and optimization of the R=5 cm configuration was much more difficult due to the narrow stability range of the cavity in this case. We believe that low-threshold versions of the mid-IR lasers can find widespread applications in spectroscopy as well as medicine and can be more readily integrated into low-cost measurement systems.

Chapter 4

BIO-MEDICAL APPLICATION OF CONTINUOUS WAVE Tm^{3+}: $YAlO_3$ LASER

4.0 Introduction

In medical applications, thulium-based lasers operating in the 1.9-2.0 μm wavelength range are emerging as alternatives to Ho-based lasers which have been in clinical use for some time, as was discussed in Section 2.8.1. Thermal effects of laser radiation on tissues due to absorption by water are exploited in medical applications of two-micron lasers (see Section 2.8.1). Therefore, Tm^{3+}:$YAlO_3$ (Tm:YAP or Tm:YAlO) laser is a strong candidate for such applications since it has a free-running output in the 1.94-1.99 μm range where water has an absorption peak (see Fig. 2.8 and 2.9). This has led us to take on a joint project with a biomedical group from Boğazici University with the objective of developing a surgical system based on diode-pumped cw Tm:YAP laser. Two application areas of medical surgery are targeted in this project. First area includes tissue coagulation (thermally killing pathological tissues without harming the healthy ones) and ablation (vaporization). The other surgical application is laser tissue welding (fusion). This project has had three stages so far: conversion of the diode-pumped Tm:YAP laser from a laboratory set-up to a robust mobile form to be used in tissue experiments, characterizing the interaction of the laser radiation with tissues via experiments on in vitro (dead) samples of animal tissues in order to optimize laser application parameters for desired coagulation and vaporization effects, and laser welding trials on in vivo (live) animal tissues to optimize laser application parameters for high quality closures. The first phase of this project was conducted at Laser Research Laboratory of Koç University while the following phases are still going on at

Boğazici University. The ultimate aim is to present the medical community a laser welding system ready for clinical use. In this chapter, first a review on laser tissue welding will be given to introduce the reader to the laser welding process and its progress through years. The review section will be followed by the description of the reassembled laser and its characterization. In the last part, preliminary results of dosimetry experiments on in vitro (dead) animal tissue samples and welding trials on in vivo (alive) animal skin tissues will be presented.

4.1 A review of Laser Welding

The laser tissue welding is the name given to the incision (cut, wound) closure technique based on the thermal fusion of tissues upon application of laser radiation. Although the mechanism of the process has not been completely understood yet, the general belief is that at temperatures above 65 ^{o}C structural changes (denaturation) take place in the extracellular proteins such as collagen and fibrinogen which form bonds upon cooling[163-165]. Laser welding of tissues has been studied for nearly three decades as an alternative to standard suture (stitching) method since it offers advantages such as immediate watertight closing of incisions and wounds, strong hemostasis (termination of bleeding), and easing of the stress and disorder experienced by the patients due to complications after surgical procedures and reaction of the body to sutures (stitches) and clips[163-165]. Laser welding began to attract more attention especially after the invention of laparoscopic surgery (minimally invasive surgery) and endoscopy where indirect intervention through endoscopic channels is required. Using suture method in laporoscopy is difficult and time consuming and actually not possible in endoscopy[163, 164]. However, laser welding is compatible with both cases due to the radiation transmitting capability of fibers in small and winding channels.

Various lasers including Nd:YAG (1.064 μm)[166, 167], CO_2 (10.6 μm)[168, 169], argon (0.5 μm)[170, 171], holmium (2.01-2.15 μm)[171-174], KTP (532 nm), and diode

lasers (808-810 nm)[173, 175] have been used in tissue welding studies. The first successful demonstration of laser welding was the closure of incisions in blood vessels of rats with an Nd:YAG laser in 1979[166]. Next milestone in the progress of laser welding was the introduction of solders based on albumin (a type of protein that experiences denaturation upon heating) to prevent the damage to the surroundings of the tissues exposed to radiation and improve the strengths of the closures[168]. Since then studies to develop the usage of solders based on albumin and other more complex proteins have shown that solders can improve the strength, reliability and shorten the duration of laser welding process[163, 164]. The function of the protein-based solders have been described as absorbing the heat to prevent thermal injury to the surroundings of the closure and reinforcing the weld via proteins undergoing denaturation and contributing to the bonding of tissues[163, 165]. In addition, chromophores (materials absorbing radiation) applied onto the tissue directly or added in the solders to enhance the absorption of laser radiation have been used to further improve the laser welding technique[163]. The chromophores function to make the energy conversion from the laser radiation to heat more efficient, reduce power requirement, increase reproducibility of welds and limit thermal damage to the area surrounding the closure[163, 167]. Common chromophores are indocine green dye with an absorption peak in albumin solution at 805 nm[173, 175] and carbon black used with diode lasers (808-810 nm)[163], fluorescein dye used with KTP laser (532 nm)[163], India ink used with Nd:YAG laser (1.064 μm)[167, 176].

To date, researchers have successfully demonstrated laser welding of gallbladder[174], gallbladder cystic duct[171], urethra[168, 175], intestine (enterotomy)[170, 172], urinary bladder[169], skin[167, 176], cornea[177], arteries and veins (vascular anastomosis)[166, 173, 178] in animals. However, its admission to clinical use has been slow due to certain limiting factors such as highly operator-dependent and thus subjective nature of the termination point (time) of the weld, difficulty with

reproducibility of results and thermal damage in the proximity of the weld site[164]. In the absence of a feedback system which gives an indication of which state the welding process is in, the operator has to depend on his visual evaluation of the closure (color of tissues, etc.) to terminate the laser radiation[169, 178]. This subjective decision can result in low quality welds due to under or over adequate thermal energy deposition in the weld area. Research has shown that weld quality is highly dependent on tissue temperature in the weld site[163, 169, 178, 179]. Hence, temperature control technique has been developed to optimize the laser welding process further and achieve high weld strength with minimum thermal damage in a reproducible manner[163, 164, 169, 170, 172, 178, 179]. In this technique, the maximum temperature of the welded tissue is stabilized, via feedback, in an optimum range which is determined through measurements of weld strength and thermal damage versus tissue temperature. In fact, using temperature control, increases in consistency[178], quality and stability[172], and success rate[169] of the laser welding process have been reported. Concerning the thermal damage in the vicinity of the closure, it was also shown that when the lateral thermal damage zone is limited to about 200 μm, the scars occurring during the healing period are reduced significantly[180]. Researchers demonstrated that effective welding with confined lateral thermal damage to less than ~200 μm could be obtained with succession of laser pulses with durations less than 100 msec and cooling periods in between pulses long enough to bring the tissues to their initial temperatures[167, 181]. Further optimization of the welding with pulsed radiation was obtained with cryogenic cooling applied to the weld zone in between pulses which increased weld strength while reducing thermal damage and the operation period for the welding process[176].

The critical aspects of laser welding technique are the matching of penetration depth of laser radiation with the thickness of the tissue to be welded, setting duration and intensity of laser radiation and determination of termination point. The desired outcome is a

strong weld covering the full depth of the incision with minimal thermal damage to the vicinity of the closure. The usage of solders and or chromophores is generally preferred in cases of lasers with high-penetration wavelength (Nd:YAG[167], 808 nm diode laser[163, 173, 175]) to increase the absorption in the weld zone and or minimize thermal damage outside it, while with low-penetration lasers (Ho:YAG[172, 173], CO_2[169],1.95 nm diode laser[178]) welding with no solder or chromophore has been demonstrated in several cases. Of course it is desirable to obtain high quality welds with no additives since it has a simpler and less time consuming operative procedure compared to welding with solders and or dyes. In our case Tm:YAP has a low-penetration wavelength (free-running wavelength range of 1.94-1.98 nm) near an absorption peak of water and therefore, we aim at achieving laser welding with no solder or dye. If it is not possible to obtain satisfactory results this way, then addition of solders and or paints will be considered.

4.2 Reassembling and Characterization of the Laser

The diode-pumped continuous-wave (cw) Tm:YAlO laser was converted from an experimental set-up in the laboratory to a robust stand-alone laser to be carried over to Bogazici University for bio-medical experiments on tissues (see Figs. 4.1.-4.3.) The laser was reassembled using two steel platforms which can be seen in Fig. 4.2. The resonator cavity was built on top of the upper platform and the laser diode was placed on the bottom face of the upper platform. The lower platform functioned as a base for the four isolating legs which carried the upper platform. The laser diode pumped the Tm:YAlO crystal via the coupling fiber connected to the imaging telescope that focused the pump beam onto the crystal. The 1.5% thulium-doped crystal and 2% output coupler (OC) was chosen to achieve as high a power as possible while operating below an input pump power of 10 W (see Section 3.2.2). To make the laser more compact and also efficient, the resonator length was reduced to 6.5 cm which resulted in a 5% increase in slope efficiency (22%) compared

to that (21%) for the 7.5 cm long cavity (see Section 3.2.2). Figure 4.4 shows the measured power efficiency of the laser.

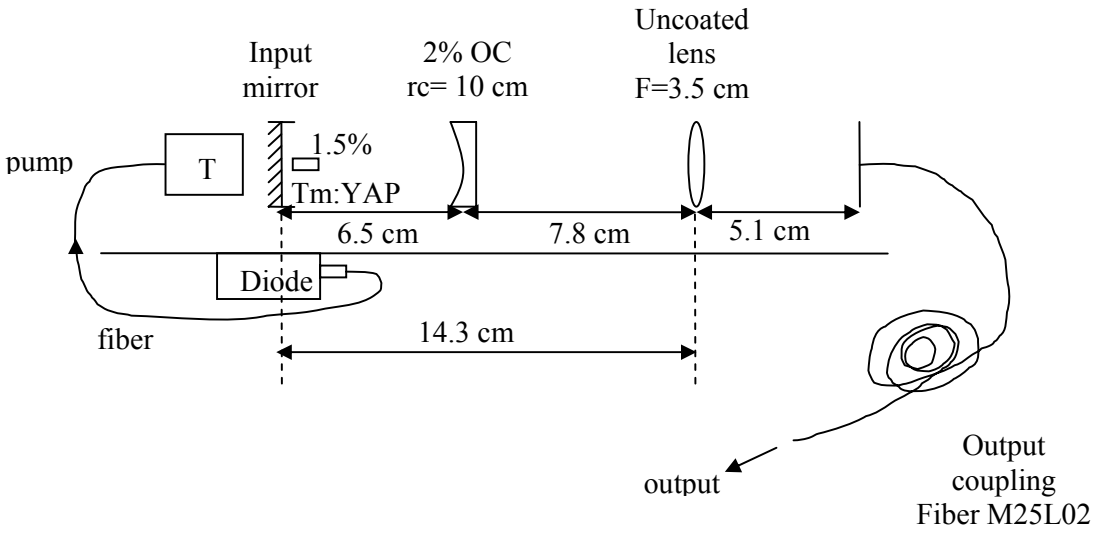

Fig. 4.1. Schematic of the reassembled Tm:YAP laser

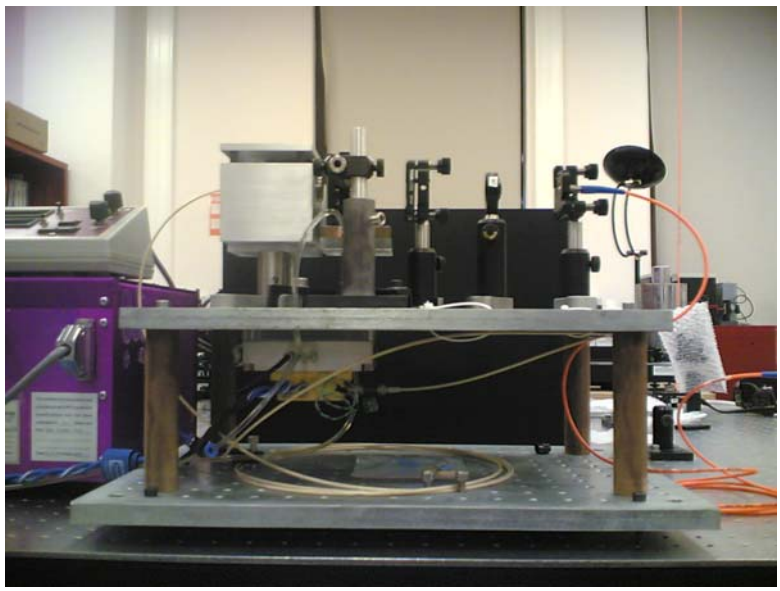

Fig. 4.2. Picture showing side view of the reassembled laser.

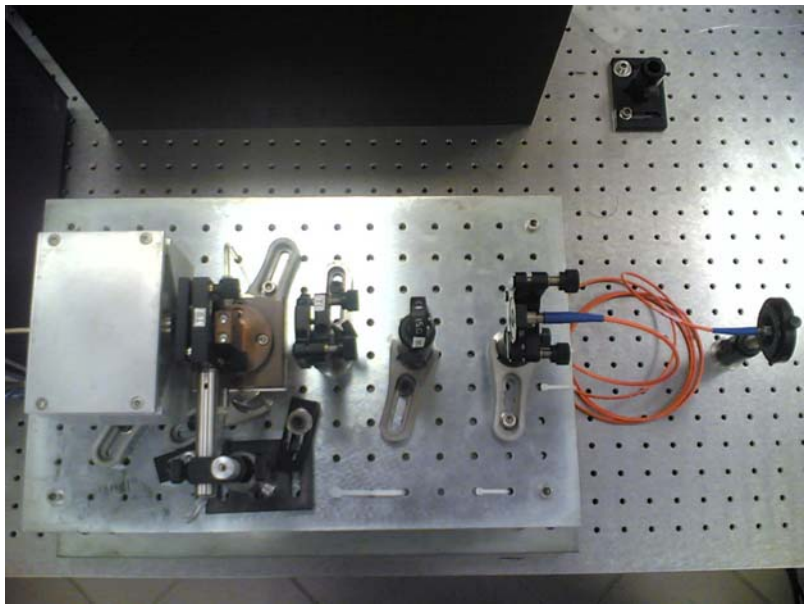

Fig. 4.3. Picture showing top view of the reassembled laser.

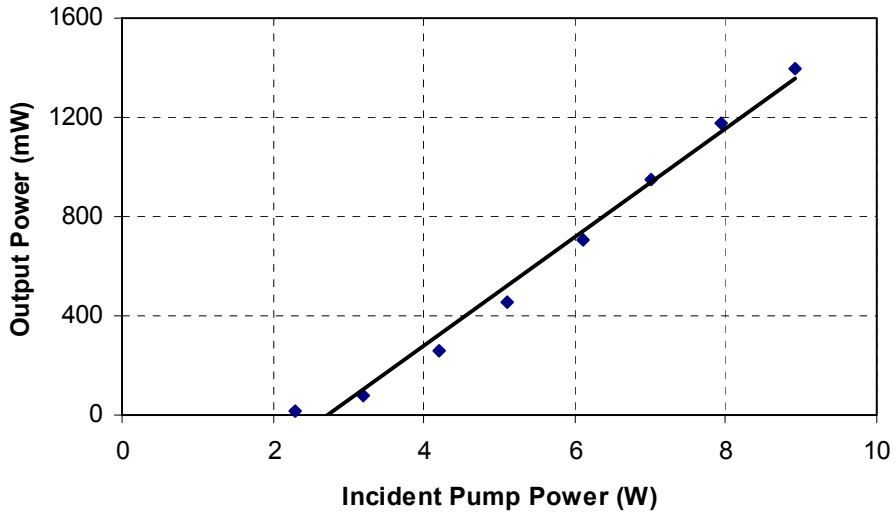

Fig. 4.4. Power efficiency curve of the reassembled Tm:YAlO laser.

4.2.1 Coupling of Laser Output into a Fiber

The output of the laser was coupled into a fiber so that laser radiation could be easily directed on tissue samples. To this end, a 2-m long multimode fiber with a core diameter of 200-μm and numerical aperture of 0.22 was used. This was a low-OH content fiber transmitting 99% at a wavelength of 2 μm. In order to efficiently couple the output of the laser into the fiber, the laser beam was imaged with a lens of 3.5 mm focal-length in a nearly 3:1 (object distance of 14.3 cm and image distance of 5.1 cm) configuration. Beam waist which occurred at the flat mirror inside the laser cavity was calculated to have a spot size of 173 μm using

$$w_1^2 = \frac{L\lambda}{\pi}\sqrt{\frac{g_2}{g_1(1-g_1g_2)}}. \qquad (4.1)$$

Eq. (4.1) gives the spot size on the first mirror of a two-mirror cavity, L is the cavity length, λ is the laser wavelength, g_1=1 - L/R_1, g_2=1 - L/R_2 where R_1 and R_2 are the radii of curvature of the first and second (input and output) mirrors. Taking the spot size at the beam waist as the object size, the imaged spot size at the entrance of the fiber was calculated as 61.7 μm using the imaging formula. The actual power coupling ratio into the fiber with a 100 μm core radius was measured to be 84%. Fig. 4.5 shows the measured power variation with incident pump power at the output of the fiber. The reassembled laser proved to have a very stable operation after running continuously for two hours at an incident pump-power of 8.9 W and an output of 1150 mW.

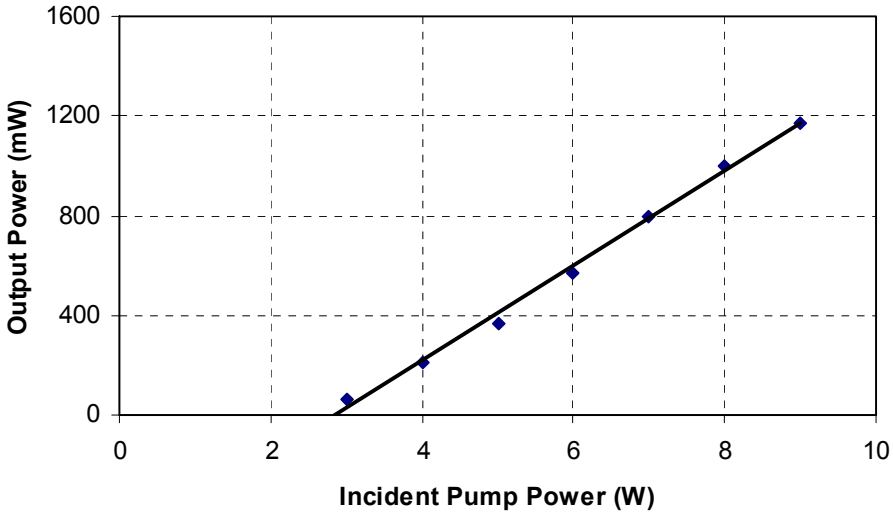

Fig. 4.5. Measured power at the output of the coupling fiber.

4.2.2 Wavelength and Spotsize Measurement at Output of Fiber

The wavelength of operation for the reassembled laser was determined to be 1.98 nm by using a monochromator and germanium detector. This was expected since 2% OC was used (see Section 3.2.2).

The spot size of the laser beam and M^2 were measured at the output of the fiber with the knife edge technique. The waist size w_o of the beam was 100 μm, equal to the core radius of the 200-μm diameter fiber and the waist was located at the output end of the fiber as expected. The M^2 was measured to be 22.7, a reasonable outcome of the multimode characteristic of the fiber. Using the measured w_o and M^2 data, the spot size $w(z)$ of the output beam at a distance z from the output of the fiber was calculated according to

$$w(z) = w_o \sqrt{1 + (\frac{\lambda M^2 z}{\pi w_o^2})^2} \tag{4.5}$$

where λ is equal to 1.98 μm. Then average intensity *I(z)* of the laser radiation at a distance z from the output of the fiber can be calculated according to

$$I(z) = \frac{P_o}{\pi w^2(z)} \tag{4.6}$$

where Po is the laser output power. Hence in experiments on tissues, the average intensity of the laser radiation incident on the tissue for a certain output power and distance of the fiber tip from the tissue can be determined using the measured w_o and M^2 data and Eqns. (4.5) and (4.6). One of the objectives of the dosimetry studies is to determine the correct average intensity level for achieving the desired effect on the tissues.

4.2.3 Cooling of the Laser

The effect of cooling on the laser performance and cooling requirement for efficient operation were investigated, since the laser was to be transported to Bogazici University and a new cooling system would be required. The laser was water-cooled with the cooling water circulating first through the copper crystal holder and then the laser diode**.** The performance measurements shown in Figures 4.4 and 4.5 were taken and stability of the laser was tested with the cooler temperature set to 20 C^o. To calculate the cooling requirement, temperature of the cooling water exiting the laser diode was measured with a thermocouple before and during operation. The temperature settled to 3 C^o above the non-operational state while the laser was operating at an output power of 1150 mW. The non-operational value was 22 C^o. The corresponding cooling rate indicated by the temperature change of the circulating water can be calculated from the heat dissipation rate = (heat

capacity of water) x (water flow rate) x (change in temperature). Water flow rate was measured to be 116 g/min. Then using 1 cal/gC^o for the heat capacity of water, the cooling rate was determined to be 5.8 cal/sec or equivalently 24 W.

The effect of cooling on the performance became apparent when the laser was cooled by circulating city water instead of a temperature-controlled chiller. The performance degraded nearly 40% with an output of 700 mW instead of 1150 mW with the same pump power. Fig. 4.6 shows the power performance at the fiber output under cooling with city water. The main reason for this decline in performance is the shift in the operating wavelength of the pump laser diode caused by the temperature change in the cooling water. The laser diode output wavelength is centered at 797 nm when operating at 25 C^o and shifts 0.3 nm per C^o with changing operation temperature. When cooled with city water, temperature was measured to be 19 C^o at the exit of the laser diode. Hence degrading output power indicated how sensitive the laser is to the shifts in the pump wavelength.

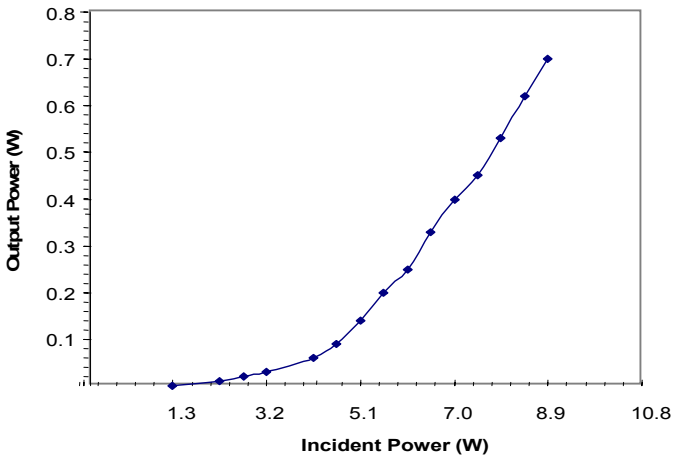

Fig. 4.6. Power performance of Tm:YAlO when cooled with city water.

4.3 Experiments on Tissues

In this section, preliminary results of experiments on tissues reported to date by the biomedical group at Bogazici University will be presented[182, 183]. At the initial stage, the interaction of the Tm:YAP laser radiation with tissues was studied by changing duration and intensity of continuous wave (cw) radiation on dead (in vitro) animal tissues of liver, heart, kidney and brain. The aim was to assess the effect of varying intensity and duration on tissues so that the correct dose for coagulation and ablation can be determined. In the experiments, the laser radiation was applied on tissues from a distance h of 10 mm as shown in Fig. 4.7[182] and the size of the affected tissue spot and penetration depth were recorded for each case. The size (radius) of the laser beam spot incident on tissues equaled 2.9 mm for h=10 mm. The results for an average incident intensity of 12.4 W/cm^2 (laser output power=0.8 W) with varying durations (5 to 120 sec) are summarized in Table 4.1[182]. A picture of the lesions (spots) formed on the tissues by irradiance of 12.4 W/cm^2 at varying durations is shown in Fig. 4.8[184].

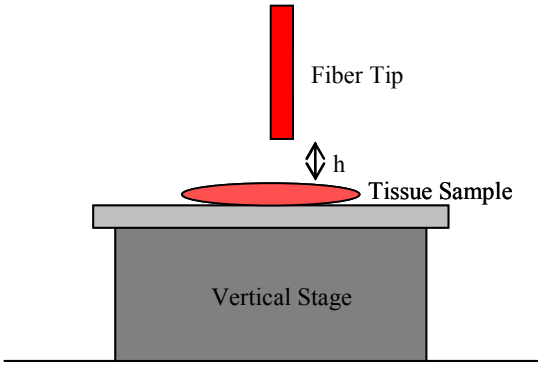

Fig. 4.7. The setup for investigating the effect of laser radiation on tissues (h=10 mm)[182].

Table 4.1

Lesion size and penetration depth for various durations t of laser radiation[182].

	liver	liver	heart	heart
	h = 10 mm	h = 10 mm	h = 10 mm	h = 10 mm
t (sec)	Lesion diameter (mm)	Penetration depth (mm)	Lesion diameter (mm)	Penetration depth (mm)
5	1.9	0.8	1.6	0.6
10	2.3	1.0	2.4	0.8
20	3.0	1.1	2.7	1.0
30	3.5	1.3	3.4	1.3
40	3.7	1.4	3.5	1.6
60	3.8	1.8	3.9	1.7
120	4.6	2.2	4.7	2.6
	kidney	kidney	brain	brain
	h = 10 mm	h = 10 mm	h = 10 mm	h = 10 mm
t (sec)	Lesion diameter (mm)	Penetration depth (mm)	Lesion diameter (mm)	Penetration depth (mm)
5	2.1	0.6	1.5	0.1
10	2.6	0.9	2.5	0.2
20	2.8	1.2	2.9	0.3
30	3.5	1.3	3.1	0.4
40	4.1	1.5	3.5	0.6
60	4.5	2.2	3.9	0.9
120	5.0	2.6	4.4	1.2

The results indicate that the lesion size and penetration depth increase with duration of the radiation as can be seen from Table 4.1. The variance between the sizes of these parameters for different tissues is caused by the different water content in each tissue resulting in a varying level of radiation absorption. It is also reported that the carbonization effect (undesired extreme burning of tissues) is dependent on the intensity of the incident radiation[184]. Further, the penetration depth is still low even if carbonization is observed on the tissue surface due to the high absorption of the radiation by the tissues[184].

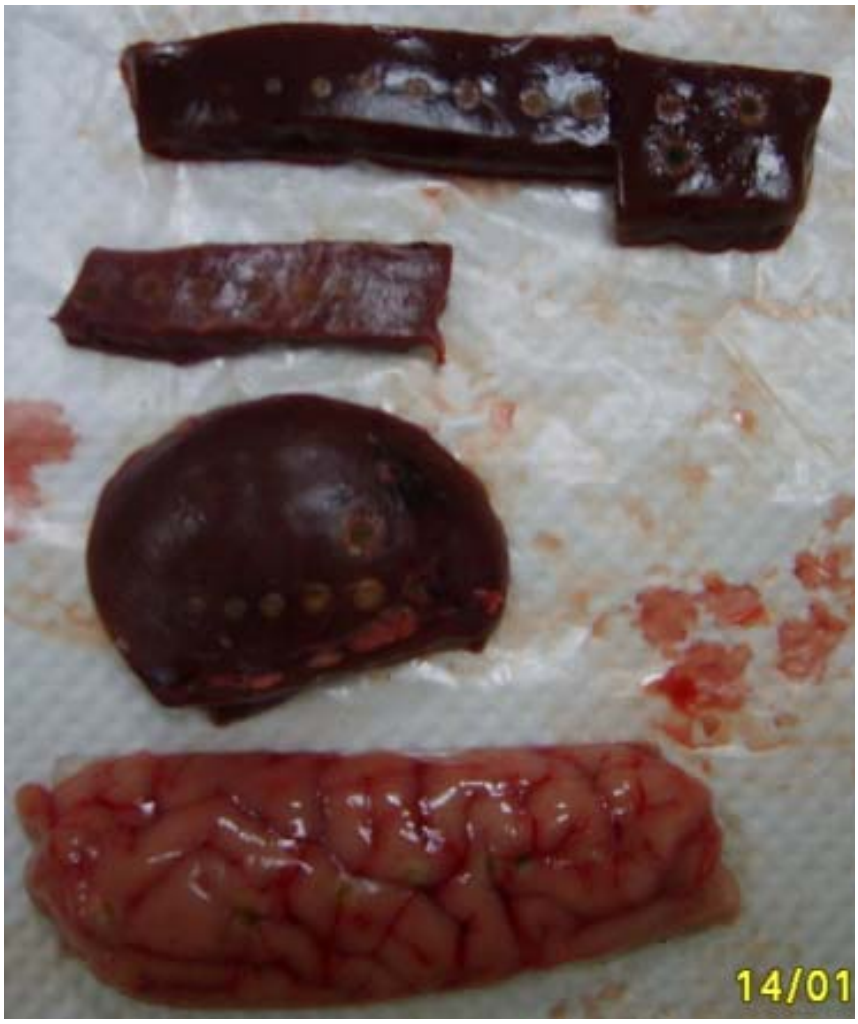

Fig. 4.8. Laser radiation spots on dead animal tissues for I=12.4 W/cm^2 with duration of 5 sec to 120 sec from left to right[184].

In a second set of experiments, laser welding dosimetry studies on live rat skin were conducted. This time cw radiation of Tm:YAP laser was applied on 1-cm long incisions (cuts) on the backs of two live Wistar rats (see Fig. 4.9). Six cuts were made on the shaved back of each Wistar rat (see Fig. 4.9) for welding tests. The welding parameters applied on

six incisions are given in Table 4.2. The welded incisions were investigated histologically after a healing period of four days. Two pictures showing the cuts on the first and fourth day after welding are shown in Fig. 4.10. Also temperature changes under the skin were investigated during the welding process with the help of a thermocouple. For temperature measurements, the laser output powers of 0.37 W and 0.52 W were applied to the incisions from a distance of 2 mm to the skin for a period of 5 sec.

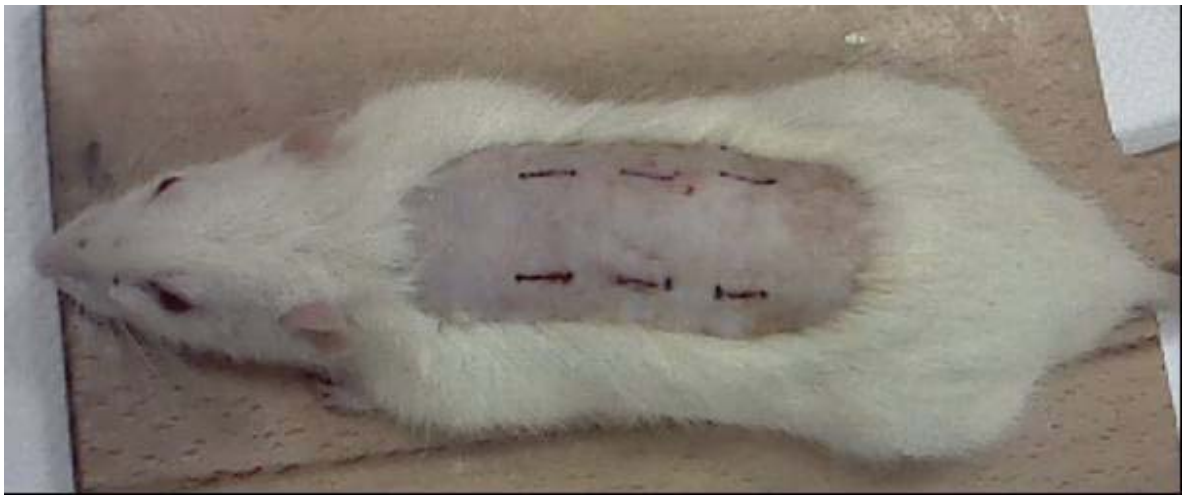

Fig. 4.9. 1-cm long incisions on the back of Wistar rat[183].

Table 4.2

Laser welding parameters for six incisions[183].

Incision No.	Power (W)	Pulse Duration (sec)	Distance to Tissue (mm)	Average Intensity (W/cm^2)
5A	0.25	3	5	15.26
5B	0.25	3	5	15.26
5C	0.53	3	5	32.35
6A	0.53	3	5	32.35
6B	0.70	3	5	42.73
6C	0.70	6	5	42.73

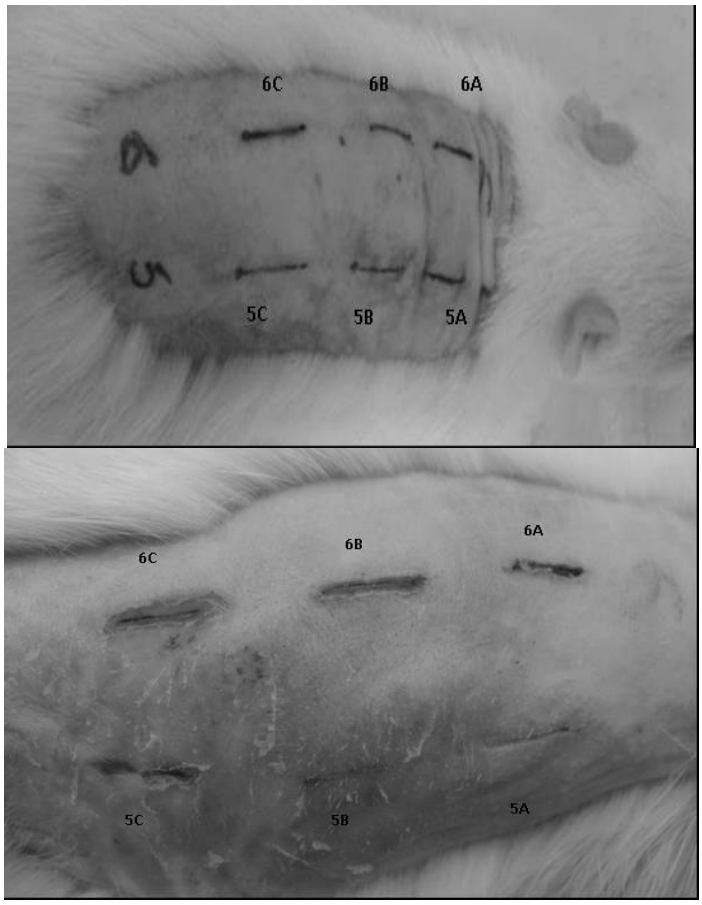

Fig. 4.10. Incisions on the first (top) and fourth (bottom) day after laser welding[183].

The results of the welding experiments show that better quality welds are obtained with the lowest intensity (15.3 W/cm^2 on incisions 5A and 5B) used while a high level of carbonization (thermal damage) on the surface is observed for the highest intensity (42.7 W/cm^2 on 6B and 6C) and less but still some carbonization on the surface observed for the medium intensity (32.4 W/cm^2 on 5C and 6A)[183]. In temperature measurements, increases of 5.3 C^o, and 14.3 C^o under the skin were recorded for 0.37 W and 0.52 W

applied to the cuts, respectively[183]. These temperature changes can only cause a negligible level of thermal damage to the tissues under the skin[183].

4.4 Summary

A joint project has been undertaken with Bogazici University to develop a surgical system based on the cw Tm:YAP laser. For experimenting on tissues, the diode-pumped cw Tm:YAP laser has been reassembled and its output was coupled into a fiber for directing radiation on target tissue samples. So far studies have been conducted to characterize the interaction of laser radiation with tissues by experimenting on in vitro animal liver, heart, kidney and brain tissues and laser welding of incisions on live rat skin. Based on the preliminary results, it has been reported that incident intensity around 15 W/cm^2 is suitable for laser welding while for coagulation and ablation higher intensity is required [182]. This collaborative project is still under progress. It has been stated that experiments are planned where histological evaluations of welding results will be performed.after varying healing periods. Healing periods of 1, 4, 7, 14, and 21 days will be tested[183]. Also pulsed radiation will be used to minimize damage to the surrounding tissues[183].

Chapter 5

SPECTROSCOPIC STUDY OF LASER MATERIALS

5.1 Introduction

Spectroscopic characterization of photonic materials has a two-fold significance relevant to laser research. It is a method for investigating the lasing potential of a new material and also for the determination of important parameters that define lasing characteristics of known laser materials. Spectroscopic study of a material consists of two main parts: measurements and data analysis. Measurements include absorption and fluorescence spectra and determination of fluorescence lifetime of excited states. The wavelength ranges for the spectrum measurements are chosen in relevance to the lasing dynamics under investigation. In our case, 190-2000 nm for absorption and 1000-2500 nm for fluorescence are chosen to cover the transitions of the 4f shell electrons in Tm^{3+} ions relevant to the generation of two-micron radiation. Similarly, in fluorescence lifetime measurements, the $^3H_4$ and $^3F_4$ levels are targeted since they play significant roles in the dynamics of lasing activity around 2 μm. In the second part of a spectroscopic study, a Judd-Ofelt analysis is applied to the absorption data to calculate Judd-Ofelt intensity parameters and radiative lifetimes of the $^3H_4$ and $^3F_4$ levels. Then, using the results of Judd-Ofelt analysis and fluorescence measurements, luminescence quantum efficiencies (parameter indicating the strength of radiative emission) of these levels and laser emission cross section at wavelengths of interest (relevant to two-micron lasing) are determined. A more detailed description of the data analysis will be given in the next section.

5.2 Spectroscopic Analysis

Physicists, beginning with Van Vleck[185] and Broer, Gorter, and Hoogschagen[186] have shown that there are three possible underlying mechanisms (electric dipole, magnetic dipole and electric quadrupole) that can account for an absorption band in a rare-earth ion (lanthanide or Ln^{3+}) and electric dipole is the dominant mechanism among the three for a majority of the transitions in rare-earths[187]. On the other hand, magnetic dipole transitions which obey the selection rules $\Delta J \leq 1$, $\Delta L=0$, $\Delta S=0$ and $\Delta l=0$[187, 188], play a significant role in only few transitions of the Ln^{3+} ions. For the spectral range used in our analyses, magnetic dipole transitions can be neglected for the Tm^{3+} ion[189]. Judd-Ofelt analysis is based on the reciprocity method where absorption bands in an absorption spectrum of a rare-earth ion can be related to the radiative parameters of that material. In this method, first, experimental integrated absorption coefficient (spectral intensity) given by

$$\left(\Sigma_{\mu}\right)_{\exp} = \int_{band} \mu(\lambda) d\lambda \tag{5.1}$$

is calculated for each absorption band by integrating the area under that band. Then, according to the Judd-Ofelt theory[190, 191], the integrated absorption coefficient $(\Sigma_{\mu})_{calc}$ of an electric dipole transition from the ground state (SLJ) to the excited state (S'L'J') can be calculated from

$$\left(\Sigma_{\mu}\right)_{calc} = \frac{8\pi^3 e^2}{3ch} \frac{(n^2+2)^2}{9n} \frac{\overline{\lambda}}{(2J+1)} N \; x \sum_{t=2,4,6} \Omega_t \left| \left\langle SLJ \left\| U^{(t)} \right\| S'L'J' \right\rangle \right|^2 , \tag{5.2}$$

where $\bar{\lambda}$ is the mean wavelength of the absorption band or bands for overlapping cases, n is the refractive index, c is the speed of light, h is Planck's constant, J is the total angular momentum quantum number of the ground state, N_o is the rare-earth ion (Tm^{3+} in our case) concentration in the material, $U^{(t)}$ are the doubly reduced matrix elements of the unit tensor operator of rank t, and Ω_t are the Judd-Ofelt intensity parameters. Then $(\Sigma_\mu)_{exp}$ is equated to $(\Sigma_\mu)_{calc}$ for each absorption band in order to solve for the three unknown Ω_t. Usually the number of absorption bands are more than three, hence an over-determined set of equations for m bands is obtained as shown below:

$$\underset{m \times 1}{\begin{bmatrix} (\Sigma_\mu)_{exp1} \\ \vdots \\ (\Sigma_\mu)_{expm} \end{bmatrix}} = \underset{m \times 3}{\begin{bmatrix} C_1 \left| \langle SLJ \| U^{(t)} \| S'L'J' \rangle \right|^2 & \cdots \\ \vdots & \\ C_m \left| \langle SLJ \| U^{(t)} \| S'L'J' \rangle \right|^2 & \end{bmatrix}} \underset{3 \times 1}{\begin{bmatrix} \Omega_2 \\ \Omega_4 \\ \Omega_6 \end{bmatrix}} \tag{5.3}$$

In (5.2), C_i's are constants given by

$$C_i = \frac{8\pi^3 e^2}{3ch} \frac{(n^2+2)^2}{9n} \frac{\bar{\lambda}_i}{(2J_i+1)} N \quad , \tag{5.4}$$

where the subscript i denotes the absorption band. The set of equations can be either solved iteratively or with an inverse matrix method with numerical means. In our studies, inverse matrix method utilizing a command ("PseudoInverse") in Mathematica was used. This

command produces the closest solution when the matrix is not invertible. With this method, numeric solutions with equivalent precision were obtained much faster compared to the iterative method. Since the matrix elements $U^{(t)}$ are not strongly host dependent[187, 192], the values tabulated by Kaminskii[187] were used in the calculation. The root-mean square error

$$\sigma_{rms} = \sqrt{\frac{\sum\left[(\Sigma_\mu)_{calc} - (\Sigma_\mu)_{\exp}\right]^2}{q-p}} \tag{5.5}$$

indicates the proximity of the approximation. In Eq. (5.5), q represents the number of bands for which line strengths are calculated (six in our case) and p the number of parameters determined (three in our case). Once the intensity parameters Ω_t are determined, the spontaneous emission probability rate $A(J,J')$ for an electric-dipole transition from an SLJ state to $S'L'J'$ state with a mean wave number $\bar{\nu}$ can be calculated using

$$A(J,J') = \frac{64\pi^4 e^2}{3h(2J+1)} \frac{n(n^2+2)^2 \bar{\nu}^3}{9} \; x \sum_{t=2,4,6} \Omega_t \left| \left\langle SLJ \left\| U^{(t)} \right\| S'L'J' \right\rangle \right|^2 . \tag{5.6}$$

Then the radiative lifetime τ_R of an excited state given by Eq. (2.7) (see Section 2.5) can be determined from the spontaneous emission rates for possible transitions from that state to lower states. The luminescence quantum efficiency η (See Section 2.5 Eqn. (2.10)) for that excited state is further calculated by using the radiative lifetime and the measured fluorescence lifetime. The stimulated emission cross section at a specific wavelength, which is an important indicator of the lasing potential of a material, can be calculated with a spectroscopic analysis in two independent ways: using the absorption data (reciprocity method) and using the emission

data. The reciprocity method relates absorption cross section to emission cross section and requires the energy level data for the rare earth ion-host combination under investigation as well as the absorption spectrum. According to the reciprocity method, the emission cross section at a certain wavelength is given by[188, 193, 194]

$$\sigma_L(\lambda) = \sigma_a(\lambda)\frac{Z_1}{Z_2}\exp\left[\left(\mathrm{E}_{z1} - \frac{hc}{\lambda}\right)\Big/ kT\right]. \tag{5.7}$$

In Eqn. (5.7), Z_1 and Z_2 are the partition functions (see Section 2.6 Eqn. (2.14)) of the lower and upper manifolds, respectively, E_{z1} is the energy difference between lowest Stark level of upper multiplet and lowest Stark level of lower multiplet called the zero line energy. In the other method based on the emission data, also called the Einstein metod[194], σ_L is calculated with the Fuchtbauer-Ladenburg equation[137, 193, 195]:

$$\sigma_L(\lambda) = \frac{\lambda^5 I(\lambda) A(J,J')}{8\pi n^2 c \int I(\lambda)\lambda d\lambda}, \tag{5.8}$$

where $I(\lambda)$ is the normalized fluorescence intensity at wavelength λ and the spontaneous emission rate $A(J,J')$ resulting from the Judd-Ofelt analysis is used. In Eqn. (5.8) the integral applies to the emission band in which λ is located and $A(J,J')$ belongs to the underlying transition. In spectroscopic works detailed in this thesis, the Fuchtbauer-Ladenburg equation was preferred because of two reasons. First, there is uncertainty on the energy levels of Tm^{3+} ions in the hosts (LuAG crystal and TeO_2-WO_3 glass) investigated here, which makes the reciprocity method unfeasible in our case. Second, it has been indicated that calculation based on Fuchtbauer-Ladenburg equation is a more accurate method as it uses fluorescence data directly[194].

In the last part of our spectroscopic analysis, the critical distance parameter R_o is estimated. R_o is a measure of the strength of cross relaxation and represents the distance among active ions for which cross relaxation rate equals the radiative decay rate[152]. Cross relaxation is an important non-radiative process in Tm-doped systems contributing to the decay of the $^3H_4$ level (see Section 2.6) while energy transfer takes place from excited-state (donor) to ground-state (acceptor) Tm^{3+} ions. If the excited ions were to decay intrinsically in the absence of non-radiative processes, then the fluorescence decay of the ion density N(t) in the $^3H_4$ level would be given by a simple exponential decay governed by the radiative lifetime as

$$N(t) = \exp(-t/\tau_R). \quad (5.9)$$

In the presence of non-radiative energy transfer mechanisms, the decay of the excited ions is expected to deviate from this exponential form according to the nature of the energy transfer processes:

$$N(t) = \exp[-t/\tau_R - \prod(t)]. \quad (5.10)$$

There are three possible mechanisms for energy transfer between excited donor and ground-state acceptor ions in non-radiative processes: direct relaxation, fast diffusion and diffusion-limited relaxation[196]. Direct relaxation is the limiting case where there is no diffusion (migration) of energy among donor ions and energy is transferred directly via coupling mechanisms such as dipole-dipole, dipole-quadrupole or quadrupole-quadrupole. Here, the fluorescence decays non-exponentially in the beginning and later intrinsically according to Eqn. (5.9). In the limit of fast diffusion, the energy migration among donor ions via resonant energy transfer is rapid due to high diffusion rate and high donor

concentration, and excited state decay has a simple exponential form. Diffusion-limited relaxation describes the case where both resonant energy transfer (diffusion) and relaxation through coupling mechanisms between donor-acceptor ions contribute to the overall decay of the excited state. Since cross relaxation takes place between excited and ground-state Tm^{3+} ions inside a host where ground-state Tm^{3+} ions play the role of both unexcited donor centers for energy diffusion and acceptors for energy transfer through coupling mechanisms, diffusion-limited relaxation applies to this process[152, 196, 197]. In a diffusion-limited relaxation process, Yokota and Tanimoto [197] showed that the deviation term in Eqn. (5.9) for a case including energy transfer by diffusion and dipole-dipole coupling is given by

$$\prod(t) = \frac{4}{3}\pi^{3/2} N_A C^{1/2} t^{1/2} \left(\frac{1 + 10.87x + 15.50x^2}{1 + 8.473x} \right). \qquad (5.11)$$

In (5.11), N_A is the concentration of the acceptor ions (equal to doping concentration N in our case), C is the interaction parameter and

$$x = DC^{1/3} t^{2/3} \qquad (5.12)$$

is the normalized time variable with D being the diffusion coefficient. In our studies, values for coefficients C and D were calculated for each sample by applying a non-linear least-squares fit to the fluorescence decay curve of the $^3H_4$ level with Eqn. (5.10), where $\prod(t)$ is given by Eqn. (5.11) and calculated radiative lifetimes were used. The critical distance parameter R_o represents the separation distance at which the non-radiative donor-acceptor energy transfer rate equals the radiative (intrinsic) decay rate as in[196]

$$C(R_o)^{-s} = \exp(-t/\tau_R). \quad (5.13)$$

In Eqn. (5.13), s depends on the multipolar interaction between donor and acceptor ions and s=6 for dipole-dipole coupling. Then R_o can be estimated from

$$R_o = (\tau_R C)^{-1/6}. \quad (5.14)$$

Once R_o is calculated, the corresponding doping concentration N can be determined considering the Tm^{3+} ions to be located at the corners of cubes each with a side of R_o inside the host lattice. So for each cube there will be 8 x (1/8)= 1 thulium ion and $N = 1/(R_o)^3$.

The following sections (5.3 and 5.4) discuss the spectroscopic studies of Tm^{3+}:LuAG, a garnet crystal with a demonstrated lasing capacity, and thulium-doped telluride-based glass Tm^{3+}:TeO_2-WO_3, a potential laser glass.

5.3 Spectroscopic Analysis of Tm^{3+}:LuAG

Lasing experiments done with thulium-doped $Lu_3Al_5O_{12}$ (Tm:LuAG) crystals have demonstrated their potential as versatile sources of coherent radiation at 2 μm [45, 46, 59, 127]. Also, Filer et al. showed, based on a quantum mechanical model, that LuAG has the best figure of merit and the lowest lasing threshold for the 2-μm transition among several other thulium-doped garnets [198]. In this work, the figure of merit (FOM) was defined as the ratio of the thulium ions in the $^3F_4$ level at the lasing threshold to the total number of thulium ions and comes to 0.06 for the 2.07-μm emission line of LuAG. For comparison, the calculated value of FOM is 0.08 for the YAG (2.04-μm emission) and YScAG (2.03-μm emission) hosts, indicating higher lasing thresholds [198]. In free-running mode, Tm:LuAG lasers operate at 2.023 μm, which is in one of the preferred wavelength ranges for lidar applications [127]. Similar to other thulium-based lasers, they can be directly

diode-pumped by using pumps operating in the 780-790 nm range [45, 46, 127]. Based on these facts, we believe the spectroscopic characteristics of Tm:LuAG deserve a detailed investigation which, to the best of our knowledge, has not been undertaken.

In this work, we present the results of spectroscopic measurements and analyses carried out with two Tm:LuAG crystals with Tm^{3+} ion concentrations of 0.5 at. % and 5 at. % (hereafter referred to as 0.5% Tm:LuAG and 5% Tm:LuAG, respectively, in the text)[199]. In the experiments, absorption and fluorescence spectra were recorded and intensity parameters (Ω_2, Ω_4, Ω_6), radiative lifetimes of the $^3H_4$ and $^3F_4$ levels, and emission cross-sections of the $^3F_4 \rightarrow {}^3H_6$ transition were calculated using the Judd-Ofelt theory (see Fig. 5.1 which shows the energy-level diagram of for Tm^{3+} ions). Fluorescence lifetime of the $^3H_4$ and $^3F_4$ levels were measured and luminescence quantum efficiencies for the $^3H_4 \rightarrow {}^3H_6$ (1470-nm band) and $^3F_4 \rightarrow {}^3H_6$ (1800-nm band) transitions were determined. Finally, the lifetime data were used to estimate the average critical distance parameter R_o which gives a measure of the strength of cross relaxation (see Section 5.2). Our measurements show that the lifetime of the $^3F_4$ level decreases from 11.2 ms for the 0.5% Tm:LuAG to 7.1 ms for the 5% Tm:LuAG sample. The measured lifetime of the $^3H_4$ level drops sharply from 851 μsec for the 0.5% doped sample to 42.3 μsec for the 5% doped sample due to the effect of cross relaxation. The substantial decrease in the lifetime of the $^3H_4$ level is also implied by the vanishing fluorescence of the 1470-nm band in the highly doped sample. The luminescence quantum efficiency of the 1800-nm band was determined to be 0.63±0.12 and 0.40±0.08 for the 0.5% and 5% Tm:LuAG samples, respectively; whereas for the 1470-nm band, it was determined to be 0.82±0.11 and 0.04±0.006 for the 0.5% and 5% Tm:LuAG samples, respectively. The emission cross section for the 2023-nm emission peak was calculated to be $1.2\pm0.2 \times 10^{-21}$ cm^2, and the critical distance parameter R_o was determined to be 10.2±0.8 Å, both representing the average of the two samples.

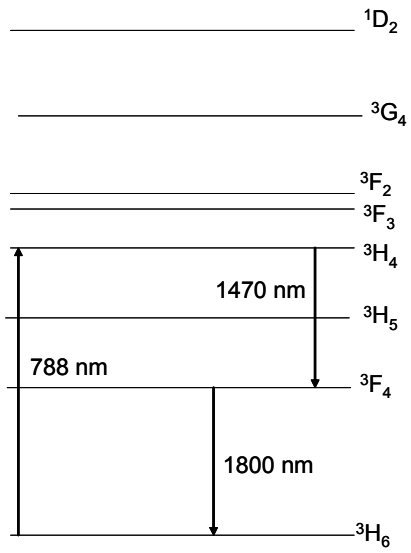

Fig 5.1 Energy-level diagram of Tm^{3+} ions.

5.3.1 Experiment

Two samples of Tm:LuAG with 0.5 at. % and 5 at. % Tm^{+} concentration were supplied by Scientific Materials Corporation, USA. The density of the samples was measured to be 6.317 g/cm^3 with a picnometer by using the Archimedes principle. The Tm^{3+} (doping) concentration N (6.7 x 10^{19} cm^{-3} for the 0.5% Tm:LuAG) was determined using the sample concentration and measured density.

The absorption spectra of the samples were measured with a spectrophotometer in the 190-2500 nm range at room temperature. In the fluorescence measurements, the samples were excited by a continuous-wave diode laser emitting at 785 nm and the collected fluorescence signal was fed into a Czerny-Turner-type monochromator. After passing through the monochromator, the signal was detected with a PbS detector and sent to an electronic amplifying and digitizing circuit. The resulting spectra were corrected for the detector and diffraction grating response. To measure the lifetimes of the $^3H_4$ and $^3F_4$

levels, the crystals were excited with a pulsed Ti:sapphire laser tuned to 788 nm to maximize the fluorescence intensity. The pulsewidth of the pump source was 70 ns. For the $^3H_4$ lifetime, the Ti^{3+}:sapphire was operated at 1 kHz and the fluorescence decay at 823 nm corresponding to $^3H_4 \rightarrow {}^3H_6$ transition was filtered through a monochromator and recorded with the help of a photo-multiplier tube sensitive up to 900-nm range. For the $^3F_4$ lifetime, the pump source was operated at 100 Hz, and fluorescence decay due to $^3F_4 \rightarrow {}^3H_6$ transition was recorded with a Germanium detector after the fluorescence from the $^3H_4$ level was eliminated by using long-pass filters.

5.3.2 Results and Discussion

Fig. 5.2(a)-(d) show the absorption spectra (absorption coefficient versus wavelength) of the samples for the 190-990 nm and 1000-2000 nm ranges. The absorption bands corresponding to the ground-state ($^3H_6$) absorption of the $^1D_2$, $^1G_4$, $^3F_2$, $^3F_3$, $^3H_4$, $^3H_5$ and $^3F_4$ levels (See Fig. 5.1) are indicated in these graphs. It is observed that the peak absorption wavelength for the $^3H_6$->$^3H_4$ transition is 788 nm, and an average absorption cross section of 5.37 x 10^{-21} cm^2 is calculated at this wavelength.

In order to apply the reciprocity method based on the Judd-Ofelt theory, the integrated absorption coefficient $(\Sigma_\mu)_{exp}$ (spectral intensity) (see Eqn. (5.1) in Section 5.2) for each indicated absorption band was calculated. The Judd-Ofelt intensity parameters were obtained by solving the over-determined system of six equations from six absorption bands formed by equating $(\Sigma_\mu)_{exp}$ to $(\Sigma_\mu)_{calc}$ (Eqns. (5.2) and (5.3)) The resulting experimental and calculated line strengths ($(\Sigma_\mu)_{exp}$ and $(\Sigma_\mu)_{calc}$) together with root-mean square error σ_{rms} for both samples, are listed in Table 5.1. Further, Table 5.2 lists the intensity parameters Ω_t, and the radiative lifetimes τ_R of the $^3F_4$ and $^3H_4$ states obtained from the Judd-Ofelt analysis. Since the intensity parameters are expected to be independent of the

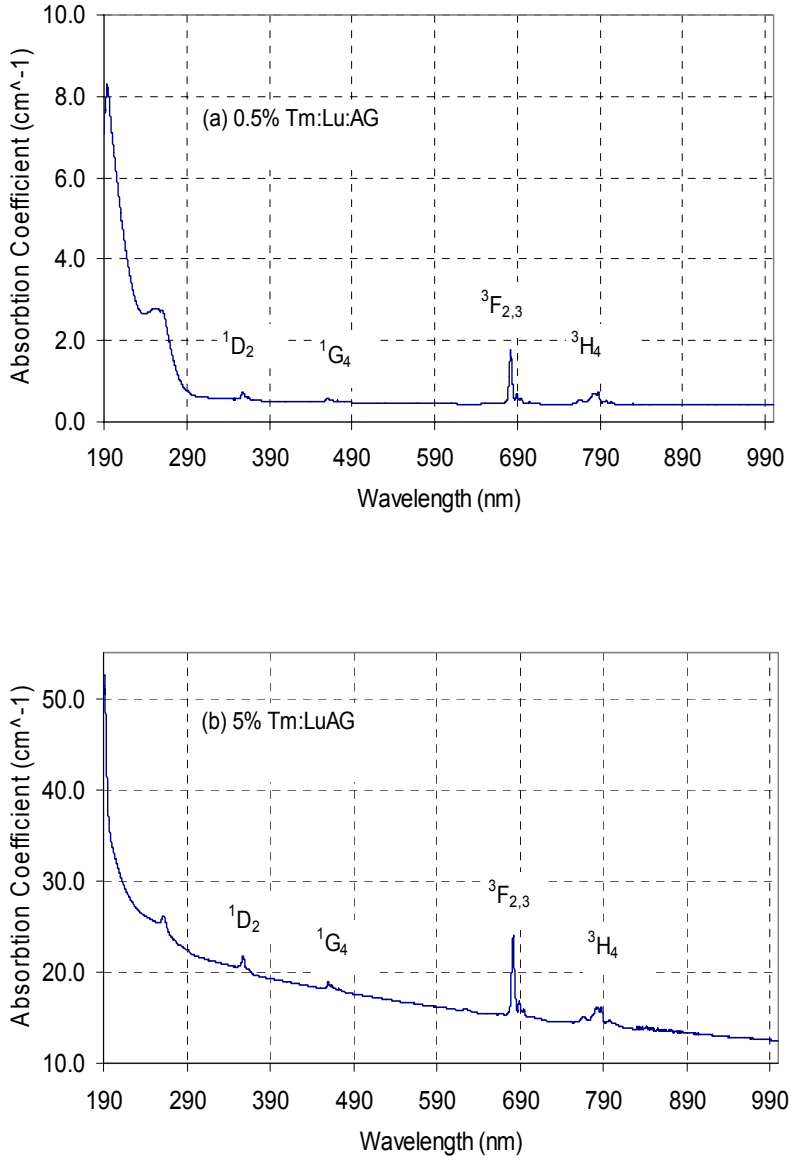

Fig. 5.2. Absorption spectra of the Tm:LuAG samples with (a) 0.5% Tm^{3+} concentration in the range 190-990 nm, (b) 5% Tm^{3+} concentration in the range 190-990 nm.

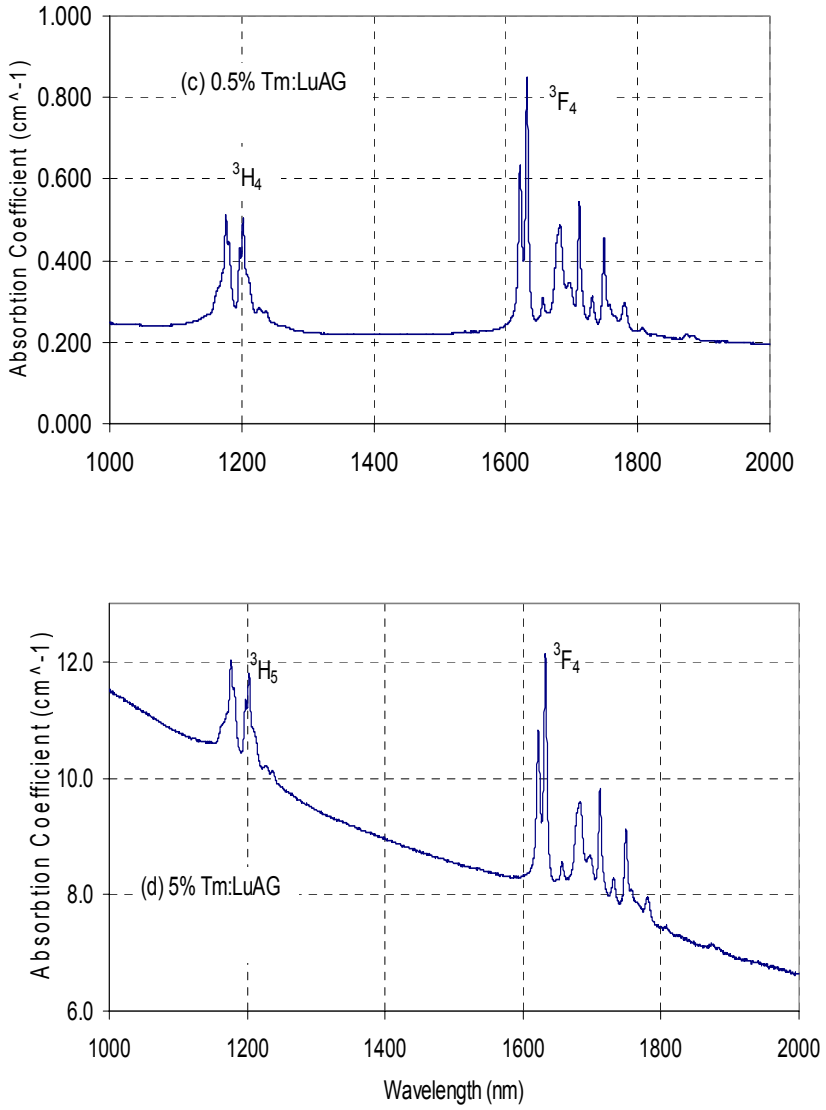

Fig. 5.2. Absorption spectra of the Tm:LuAG samples with (c) 0.5% Tm^{3+} concentration in the range 1000-2000 nm, and (d) 5% Tm^{3+} concentration in the range 1000-2000 nm.

Table 5.1

Measured and calculated integrated absorption coefficients and root-mean square error for the Tm:LuAG samples.

Transition from $^3H_6\rightarrow$	0.5% Tm:LuAG		5% Tm:LuAG	
	$(\Sigma_\mu)_{exp}$ (10^{-6})	$(\Sigma_\mu)_{calc}$ (10^{-6})	$(\Sigma_\mu)_{exp}$ (10^{-6})	$(\Sigma_\mu)_{calc}$ (10^{-6})
$^1D_2$	0.15	0.11	0.96	0.66
$1G_4$	0.09	0.04	0.57	0.30
$^3F_{23}$	0.86	0.84	5.48	5.22
$^3H_4$	0.58	0.55	4.25	3.98
$^3H_5$	0.91	0.94	5.76	6.20
$^3F_4$	1.58	1.58	12.2	12.2
σ_{rms} (10^{-7})	0.45		4.1	

doping concentration, the average values of Ω_t, shown in Table 5.2, were used in the calculation of τ_R. Also included in Table 5.2, is the estimated error in each parameter originating from the difference between the calculated intensity parameters for the two samples. The uncertainty in the results is comparable to the expected accuracy limit for the Judd-Ofelt model [200]. In calculating the lifetimes of the $^3F_4$ the(1800 nm) and $^3H_4$ (1470 nm) levels, the tabulated matrix elements $\left|\left\langle SLJ\right\|U^{(t)}\left\|S'L'J'\right\rangle\right|^2$ in [187] were used.

Table 5.2

Calculated values of the intensity parameters and the radiative lifetimes of the $^3F_4$ and $^3H_4$ levels for the Tm:LuAG samples.

Tm:LuAG sample	Ω_2 (10^{-21} cm^2)	Ω_4 (10^{-21} cm^2)	Ω_6 (10^{-21} cm^2)	$\tau_{R\,(\mu s)}$ $^3H_4$	$\tau_{R\,(ms)}$ $^3F_4$
0.5%	4.39	8.08	10.5	917.6	14.9
5%	5.93	4.84	6.59	1203.8	21.7
Average	5.16±15%	6.46±25%	8.55±23%	1041.4±143[a]	17.7±3.4[a]

[a] Calculated by using the average intensity parameters from Table5.2.

Figs. 5.3(a) and (b) show the fluorescence spectra of the two Tm:LuAG samples for the 1000-2500 nm range. Disappearance of the 1470-nm ($^3H_4 \rightarrow {}^3F_4$) emission band for the sample with higher Tm^{3+} concentration (Fig. 5.3(b)) indicates strong cross relaxation. A similar effect was observed in other thulium doped materials [148, 201]. The vanishing 1470-nm band points to the evident growth in the strength of cross relaxation as the Tm^{3+} concentration increases ten-fold, bringing the ions closer.

The fluorescence spectra were used to calculate the stimulated emission cross section σ_{em} for the $^3F_4 \rightarrow {}^3H_6$ (1800-nm) transition using the Fuchtbauer-Ladenburg equation (Eqn. (5.8)). Calculated σ_{em}, for the two samples, at 1754, 1969 and 2023-nm peaks inside the 1800-nm band are presented in Table 5.3. Among the three peaks, the highest σ_{em} value of 1.2±0.2 x 10^{-21} cm^2 (average of the two samples) occurring at 2023 nm is in reasonable agreement with the value (1.66 x 10^{-21} cm^2) reported in Ref [127]. It also confirms the free-running wavelength of the Tm:LuAG laser.

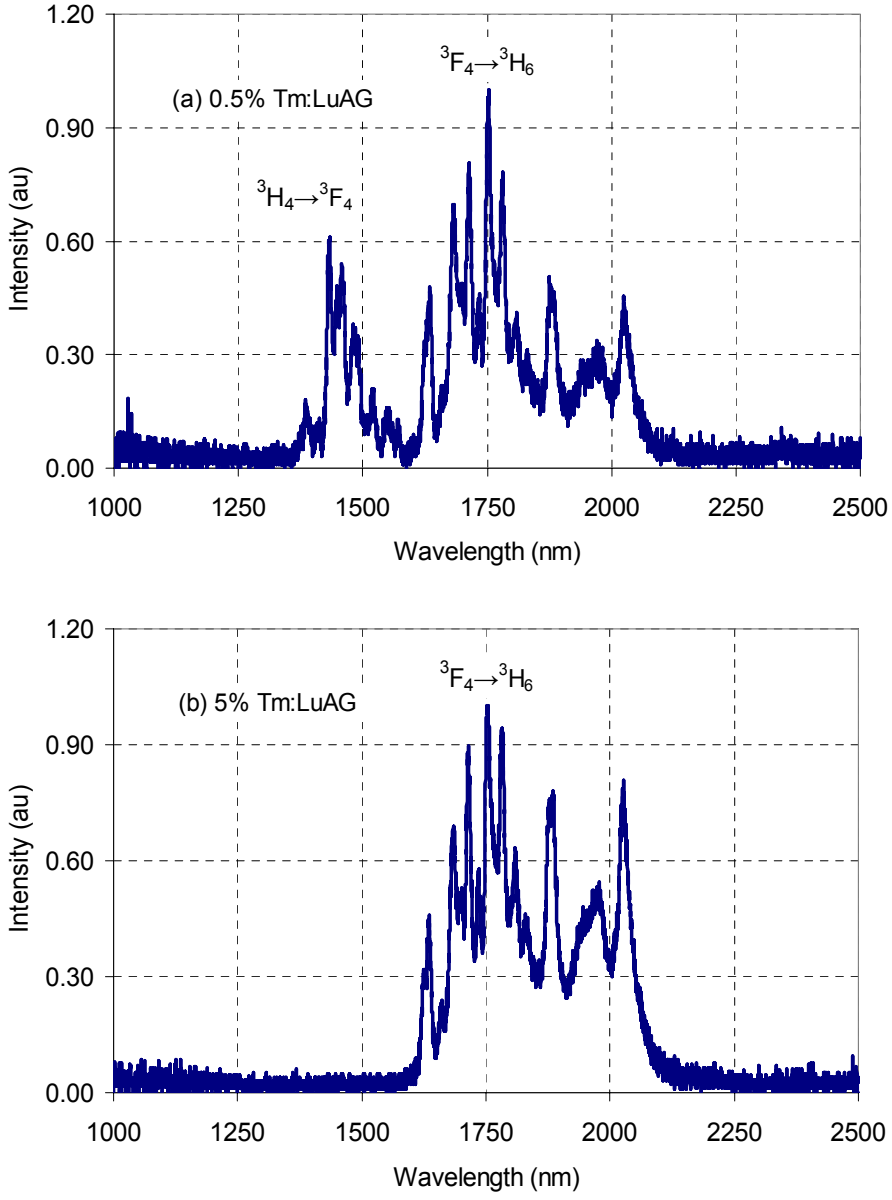

Fig. 5.3. Fluorescence spectra of the (a) 0.5% Tm:LuAG and (b) 5% Tm:LuAG samples. Emission bands corresponding to the $^3H_4 \rightarrow {}^3F_4$ and $^3F_4 \rightarrow {}^3H_6$ transitions are indicated.

Table 5.3

Stimulated emission cross sections for three peaks of the $^3F_4 \rightarrow {}^3H_4$ (1800 nm) transition.

Tm:LuAG	σ_{se} (10^{-21} cm^2)		
Sample	1754 nm	1969 nm	2023 nm
0.5%	1.36±0.26	0.71±0.13	1.11±0.21
5%	0.93±0.18	0.84±0.16	1.38±0.26
Average	1.15±0.22	0.78±0.15	1.24±0.24

The recorded fluorescence decay curves of the $^3F_4$ and $^3H_4$ levels for both samples are shown in Figs. 5.4 and 5.5, respectively. The initial rise in the decay curve of the $^3F_4$ level (see Fig. 5.4) is a result of the gradual build-up of this level, as the ions initially excited to the $^3H_4$ level by the pump radiation decay after a finite time to populate the $^3F_4$ level. The initial build-up effect is notably more visible in the 0.5% Tm:LuAG sample in which the decay of the $^3H_4$ level is significantly slower than that in the 5% Tm:LuAG sample. The faster decay of the $^3H_4$ level for the 5% sample is clearly observed in Fig. 5.5, where the time scale for the decay of this level is about twenty times larger for the 0.5% Tm:LuAG sample. The cross relaxation effect is mainly responsible for the sharp increase in the decay rate of the $^3H_4$ level with increasing concentration. The measured fluorescence lifetimes τ_F of the $^3H_4$ and $^3F_4$ levels were determined by fitting the tail of each fluorescence decay curve to a single exponential. Table 5.4 lists for both samples the measured lifetimes τ_F and the corresponding luminescence efficiencies η. In calculating the luminescence efficiency, average radiative lifetimes resulting from the Judd-Ofelt analysis (see Table 5.2) were used. The decrease from 11.2 ms for the 0.5% Tm:LuAG sample to

7.1 ms for the 5% Tm:LuAG sample in the lifetime of the $^3F_4$ level also indicates the effect of increasing nonradiative processes with denser population of Tm^{3+} ions inside the lattice. Comparable variations of lifetime with Tm^{3+} concentration have been reported for other host crystal and glasses [148, 152, 201]. The average lifetime value determined in our study is somewhat lower than 10.2 ms reported in [46] for the $^3F_4$ lifetime of Tm:LuAG samples with Tm^{3+} concentration varying from 2 to 11%.

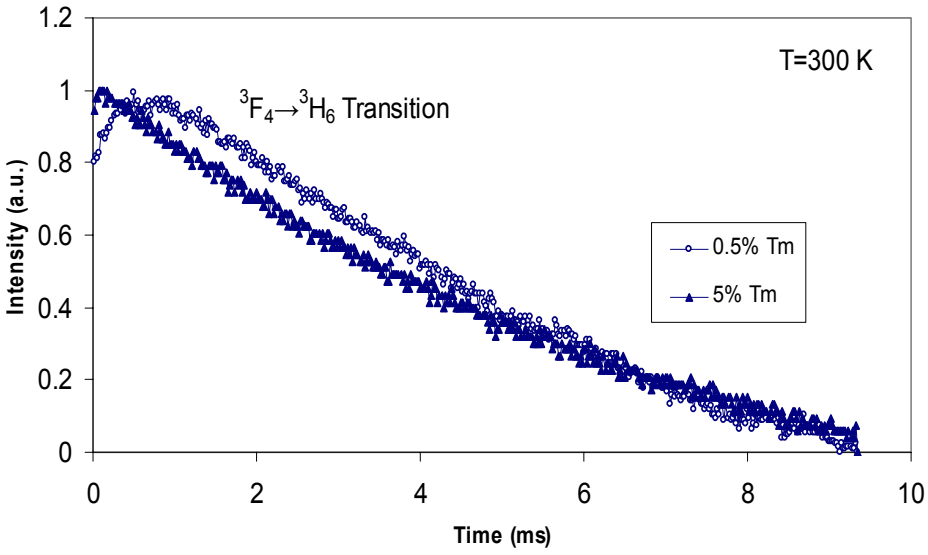

Fig. 5.4. Measured fluorescence decay curves of the $^3F_4$ level for the Tm:LuAG samples.

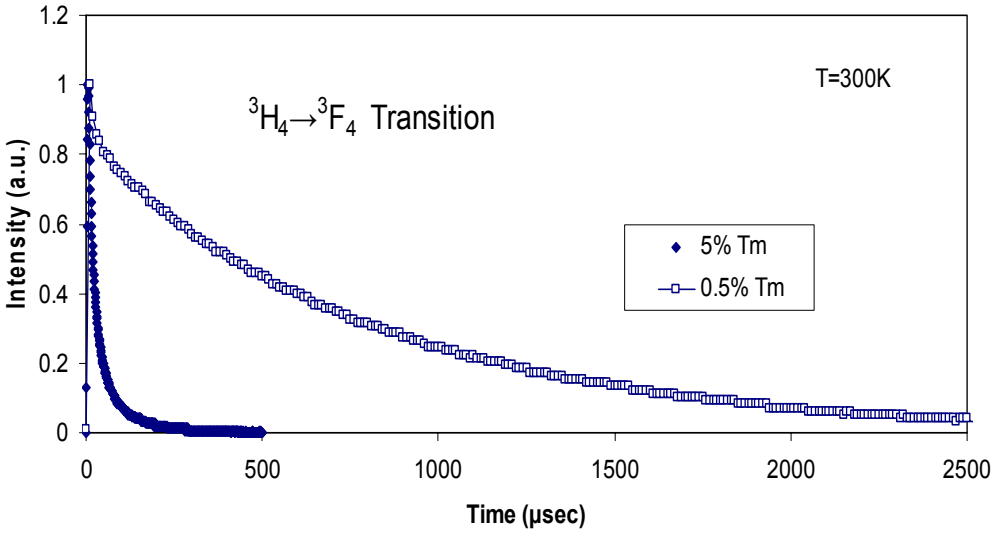

Fig. 5.5. Measured fluorescence decay curves of the $^3H_4$ level for the Tm:LuAG samples.

Table 5.4

Fluorescence lifetimes τ and fluorescence quantum efficiencies η for the Tm:LuAG samples

Tm:LuAG sample	τ (μs) $^3H_4$	τ (ms) $^3F_4$	η $^3H_4$	η $^3F_4$
0.5%	851	11.2	0.82±0.11	0.63±0.12
5%	42.3	7.1	0.041±0.006	0.40±0.08

Finally, we estimated the critical distance parameter R_o for Tm:LuAG (see last part of Section 5.2). Interaction parameter C and diffusion coefficient D in Eqns. (5.11) and (5.12) were calculated by applying non-linear least-squares fit. The measured decay curve of the $^3H_4$ level and the calculated best fit curve for the 5% Tm:LuAG sample are both shown in

Fig. 5.6. The least-squares fit yielded C=6.74x10^{-40} cm^{6}s^{-1} and D=6.05x10^{-12} cm^{2}s^{-1} for the 0.5% Tm:LuAG, and C=1.70x10^{-39} cm^{6}s^{-1} and D=8.66x10^{-12} cm^{2}s^{-1} for the 5% Tm:LuAG sample. Using the calculated value for C and the average radiative lifetime τ_R for the $^3H_4$ level (see Table 5.2), R_o values of 9.4 Å and 11.0 Å were obtained for the 0.5% and 5% Tm:LuAG samples, respectively, giving an average value of 10.2±0.8 Å. This corresponds to a Tm^{3+} concentration of 9.42 x 10^{20} cm^{-3} or nearly 7 at. %. In other studies, average R_0 values of 17.9 and 7.3 Å were reported for thulium-doped $0.7TeO_2$:$0.3CdCl_2$ glass[152] and for thulium-doped $Ge_{30}Ga_2As_6S_{62}$[202], respectively.

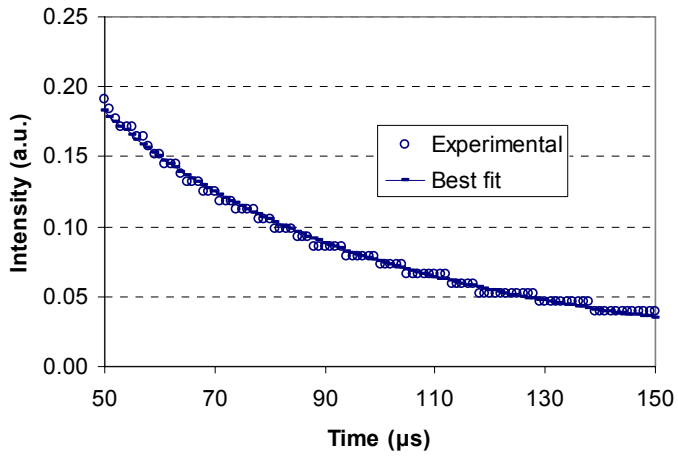

Figure 5.6. Measured fluorescence decay of the $^3H_4 \rightarrow {}^3F_4$ transition and calculated best fit to equations (8) and (9) for the 5% Tm:LuAG sample.

5.4 Spectroscopic Investigation of Tm^{3+}:TeO_2-WO_3 Glass

Thulium doped glasses have attracted a great deal of interest for several reasons. First and foremost, the emission band of Tm^{3+} centered at 1460 nm holds a potential for developing fiber-optic amplifiers in telecommunication systems, while the second band centered at 1800 nm is suitable for developing lasers for medical applications as well as atmospheric

and chemical sensing. The ease and low cost of preparing glasses, in comparison with crystals, further makes them an attractive candidate as host materials. Furthermore, telluride glasses have numerous favorable optical properties such as a wide transmission range from ultraviolet to mid infrared (0.35-5.0 μm), lower phonon energy (700-750 cm^{-1}) than other known glass hosts such as borates or silicates, high linear and nonlinear refractive index, good stability and resistance to moisture[203-205]. This has prompted a widespread interest in the spectroscopic investigation of thulium doped telluride glasses[152, 201, 204-210]. In the particular case of TeO_2-WO_3 glass host, researchers investigated the effects of glass composition on the emission strengths in thulium (Tm_2O_3) doped (1-x)TeO_2-(x)WO_3 glasses[209] and concluded, based on radiative lifetime calculations, that lower WO_3 content (x=0.15) favored the 1460 nm and 1800 nm emissions compared to the higher contents of x=0.25 and x=0.30.

In this section, we present a detailed spectroscopic analysis of Tm_2O_3:(0.85)TeO_2-(0.15)WO_3 glass and investigate the characteristics of the near-infarared bands centered at 1460 nm and 1800 nm[211]. In the experiments, absorption and fluorescence measurements were performed on two glass samples; 0.25 mol% and 1.0 mol% Tm_2O_3 doped (0.85)TeO_2-(0.15)WO_3 (hereafter referred to as 0.25 mol% sample and 1.0 mol% sample). Intensity parameters were calculated with an average error margin of 5% by applying the Judd-Ofelt theory on the absorption spectra of the two samples. Radiative lifetimes of 305±7.5 μsec and 1.95±0.02 msec were obtained for the $^3H_4$ and $^3F_4$ levels (refer to Figure 5.1 for the energy diagram of Tm^{3+} ion), respectively, by using the calculated intensity parameters. The measured fluorescence lifetimes yielded luminescence quantum efficiencies of 0.72±0.02 ($^3H_4$) and 0.95±0.01 ($^3F_4$) for the 0.25 mol% sample, decreasing to about 0.2 for both levels in the case of the 1 mol% sample. The fluorescence spectra showed a reversal in relative strengths of the 1460-nm and 1800-nm bands with increasing doping concentration, 1460 nm being dominant in the 0.25 mol% sample and

1800 nm in the 1.0 mol% sample. Calculated stimulated emission cross sections (3.73±0.1 $x10^{-21}$ cm^2 at 1460 nm and 6.57±0.07 $x10^{-21}$ cm^2 at 1800 nm) suggest that the Tm_2O_3:(0.85)TeO_2-(0.15)WO_3 glass is a potentially important gain medium for thulium-based amplifiers and lasers. Finally, the average critical distance, R_o, which is a measure of the strength of cross relaxation in the material, was determined to be 9.1 ± 0.8 Å for the samples.

5.4.1 Experiment

The glass samples were prepared from reagent-grade powders of TeO_2 (99.999% purity, Aldrich Chemical Company), WO_3 (99% purity, Aldrich Chemical Company) and Tm_2O_3 (99% purity, Aldrich Chemical Company). In preparing the powder mixtures for the glass samples, we used 0.25 mole of Tm_2O_3 and 1.0 mole of Tm_2O_3 to 100 moles of (0.85)TeO_2-(0.15)WO_3 for the 0.25 mol% and 1.0 mol% sample, respectively. The batches were mixed and melted in an air-filled furnace at 800 ºC for 1 hour by using a platinum crucible with a closed lid. The melts were then removed from the furnace at 800 ºC and quenched in air inside a stainless steal mold at room temperature. The glass samples were annealed at 250 ºC, below the glass transition temperature[212] for 1 hour to remove the internal thermal stresses. Finally, two surfaces of the samples were polished for spectroscopic measurements. The density of the glass was determined to be 5.82 g cm^{-3} with the help of a picnometer.

A spectrophotometer was used to measure the absorption spectra of the glass samples in the 300-2000 nm range. To measure the fluorescence spectrum, each sample was excited by a pulsed Ti:sapphire laser tuned to around 794 nm operating at a pulse repetition frequency of 1 kHz and the emitted luminescence was recorded by a system consisting of a collecting mirror, 0.5-m Czerny-Turner-type monochoromator, PbS detector, and lock-in amplifier. Spectral response of the grating and the detector was taken

into account in producing the final spectra. In measuring the lifetimes of the $^3H_4$ and $^3F_4$ levels, the pulsed Ti:sapphire laser, tuned to around 794 nm, was used again to excite the samples, but this time with different repetition rates for each level. For the $^3H_4$ level, the laser was operated at 1 kHz and the fluorescence emitted from each sample at 823 nm, corresponding to the $^3F_4 \rightarrow {}^3H_6$ transition, was detected with a monochromator and a photomultiplier tube. For the $^3F_4$ level, the laser was operated at 100 Hz and the fluorescence of the band centered at 1800 nm was selected with the help of band-pass filters and detected with a Ge detector. The pulsewidth of the laser source was 70 ns for all cases.

5.4.2 Results and Discussion

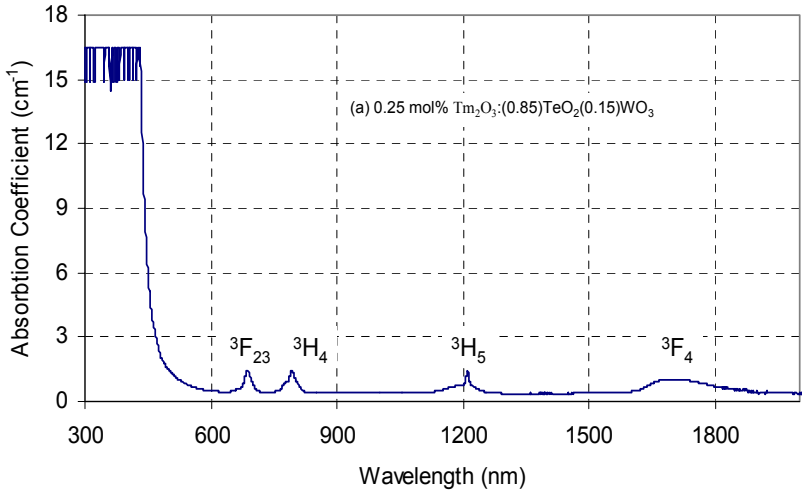

Figure 5.7 (a). Absorption spectra of the Tm_2O_3:(0.85)TeO_2-(0.15)WO_3 samples with 0.25 mol% Tm_2O_3 concentration in the 300-2000 nm range.

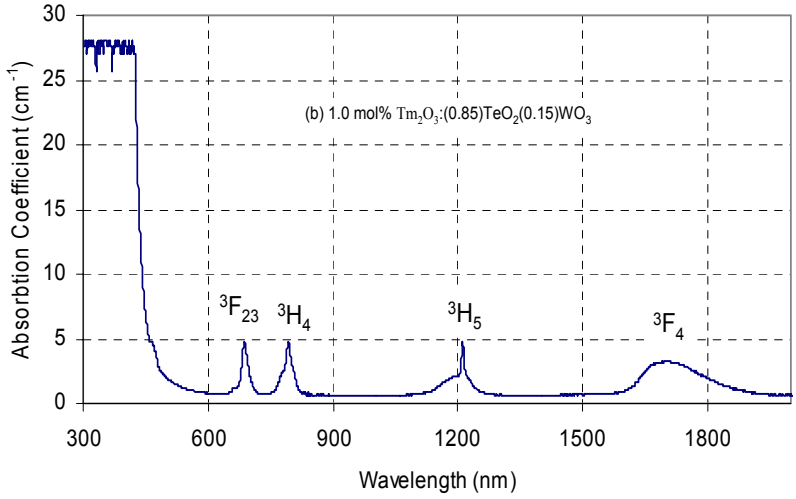

Figure 5.7(b). Absorption spectra of the Tm_2O_3:(0.85)TeO_2-(0.15)WO_3 samples with 1.0 mol% Tm_2O_3 concentration in the 300-2000 nm range.

The measured absorption spectra (see figures 5.7(a)-(b)) show four bands corresponding to the transitions from the $^3H_6$ ground state to $^3F_2$ and $^3F_3$, $^3F_4$, $^3H_5$ and $^3H_4$ levels. The absorption cross section at the pump wavelength (794 nm) was determined to be 9.7 x 10^{-27} cm^2 using the spectra and calculated thulium (Tm^{3+}) concentration N which came to 1.0 x 10^{20} cm^{-3} and 4.0 x 10^{20} cm^{-3} for the 0.25 mol% and 1.0 mol% samples, respectively. N was calculated using the measured density (5.82 g cm^{-3}) and the molar weight w for the samples, where w (0.25 mol% sample)= 0.0025x385.86 (Tm_2O_3) + 0.85x159.6 (TeO_2) + 0.15x215.85 (WO_3) =169.00 and w (1.0 mol% sample)= 0.01x385.86 (Tm_2O_3) + 0.85x159.6 (TeO_2) + 0.15x215.85 (WO_3)= 171.90.

Table 5.5

Measured and calculated integrated absorption coefficients and root-mean squared error for the Tm_2O_3:(0.85)TeO_2-(0.15)WO_3 samples.

Transition from $^3H_6\rightarrow$	0.25 mol% Tm_2O_3: (0.85)TeO_2-(0.15)WO_3		1.0 mol% Tm_2O_3 :(0.85)TeO_2-(0.15)WO_3	
	$(\Sigma_\mu)_{exp}$ (10^{-6})	$(\Sigma_\mu)_{calc}$ (10^{-6})	$(\Sigma_\mu)_{exp}$ (10^{-6})	$(\Sigma_\mu)_{calc}$ (10^{-6})
$^3F_{2,3}$	1.99	2.17	8.46	9.6
$^3F_4$	2.52	2.61	10.2	10.8
$^3H_5$	3.56	3.32	15.8	14.3
$^3H_4$	11.6	11.6	47.4	47.5
σ_{rms} (10^{-6})	0.32		2.0	

The experimental integrated absorption coefficient $(\Sigma_\mu)_{exp}$ was calculated for each one of the four bands from the absorption spectra after subtracting the background. The over-determined set of four equations for each sample was solved approximately for the intensity parameters Ω_t with an inverse matrix method. In solving the equations for Ω_t, host- independent matrix elements $U^{(t)}$ tabulated by Kaminskii[187] were used. As mentioned previously in Section 5.2, the contributions of magnetic dipole transitions in the integrated absorption coefficient were neglected. Table 5.5 shows the experimental and calculated integrated absorption coefficients for each sample and the root-mean squared

error which gives a measure of the uncertainty resulting from approximately solving four equations for three unknown intensity parameters. The calculated intensity parameters Ω_t for both samples are listed in Table 5.6. The average error of 5% in the mean Ω_t values arising from the discrepancy between the two samples is well within the uncertainty level inherent in the Judd-Ofelt technique[200]. Table 5.6 also shows the radiative lifetimes for the $^3F_4$ and $^3H_4$ levels obtained using the calculated intensity parameters. Note that the average radiative lifetimes were calculated using the mean intensity parameters and the low uncertainty (below 3%) reflects that the Judd-Ofelt analysis was consistent for each sample.

Table 5.6

Calculated values of the intensity parameters and the radiative lifetimes of the $^3F_4$ and $^3H_4$ levels for the Tm_2O_3:(0.85)TeO_2-(0.15)WO_3 samples.

Tm_2O_3:(0.85)TeO_2-(0.15)WO_3 sample	Ω_2 (10^{-21} cm^2)	Ω_4 (10^{-21} cm^2)	Ω_6 (10^{-21} cm^2)	$\tau_{R\ (\mu s)}$ $^3H_4$	$\tau_{R\ (ms)}$ $^3F_4$
0.25 mol%	4.54	1.77	1.22	312	1.97
1.0 mol%	4.65	2.1	1.41	297	1.94
Average	4.6±1.2%	1.93±8.6%	1.32±7.3%	305±7.5[a]	1.95±0.02[a]

[a] Calculated by using the average intensity parameters from Table 5.6.

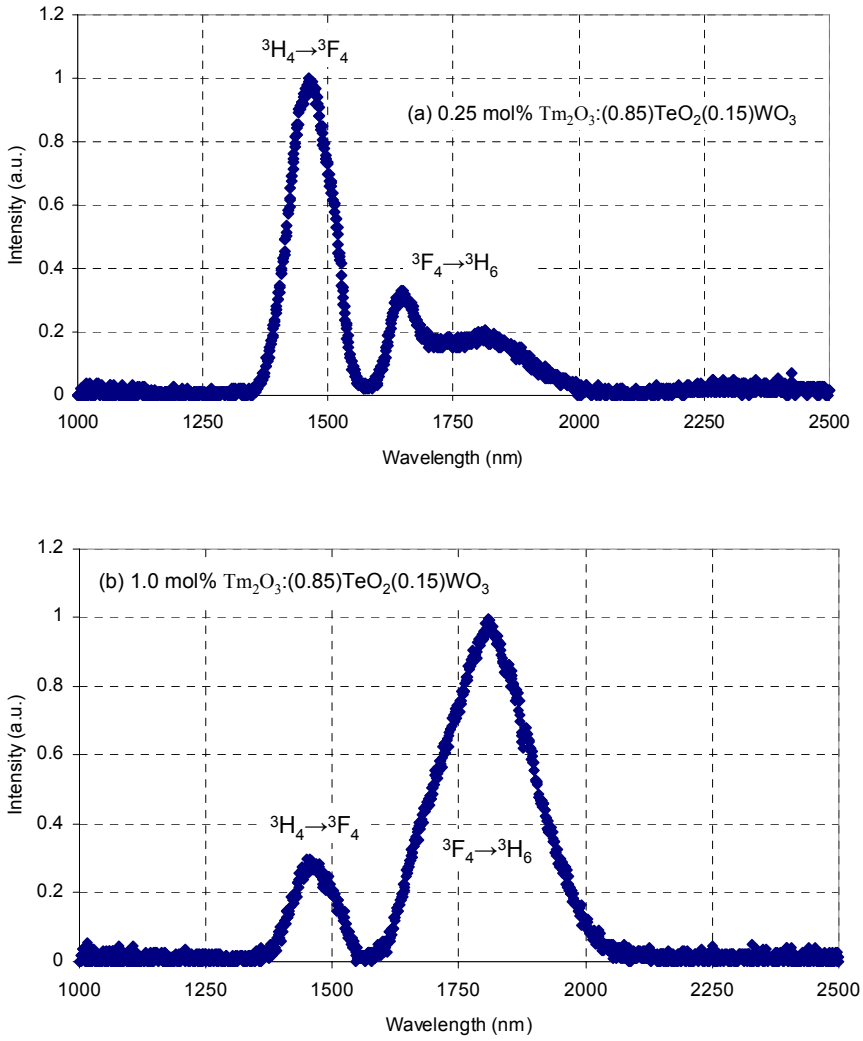

Fig. 5.8. Fluorescence spectra of the glass samples.

Figures 5.8(a) and (b) show the relative strengths of the luminescence bands centered at 1460 nm ($^3H_4 \rightarrow {}^3F_4$ transition) and 1800 nm ($^3F_4 \rightarrow {}^3H_6$ transition) at the two different thulium concentrations. The reduction in the strength of the 1460 nm band with respect to that at 1800 nm with increasing thulium concentration is a consequence of the cross

relaxation effect which becomes more effective with denser population of active ions. The fact that the 1460-nm band is dominant for the 0.25 mol% sample indicates that cross relaxation is negligible at this doping level in (0.85)TeO2-(0.15)WO_3 glass.

Figures 5.9 and 5.10 contain the measured fluorescence decay curves of the $^3H_4$ and $^3F_4$ levels, respectively, for both samples. The fluorescence lifetimes were inferred by doing a single exponential fit to the tails of the decay curves. Shown in Table 5.7 are the fluorescent lifetimes τ_F for the $^3F_4$ and $^3H_4$ levels and the resulting luminescence (fluorescence) efficiencies η. Here, average calculated radiative lifetimes from Table 5.6 were used. The decreasing efficiencies with increasing doping concentration indicate that both levels are affected by increasing nonradiative decay. Luminescence efficiency η for an energy level gives the ratio of total radiative decay rate to total decay (radiative plus nonradiative) rate. Transitions to three lower levels ($^3H_5$, $^3F_4$ and $^3H_6$) are involved in the decay of the $^3H_4$ level and the branching ratio to $^3F_4$ level (see Table 5.8) reveals that$^3H_4 \rightarrow {}^3F_4$ transition has only a small contribution. Therefore, radiative efficiency for the

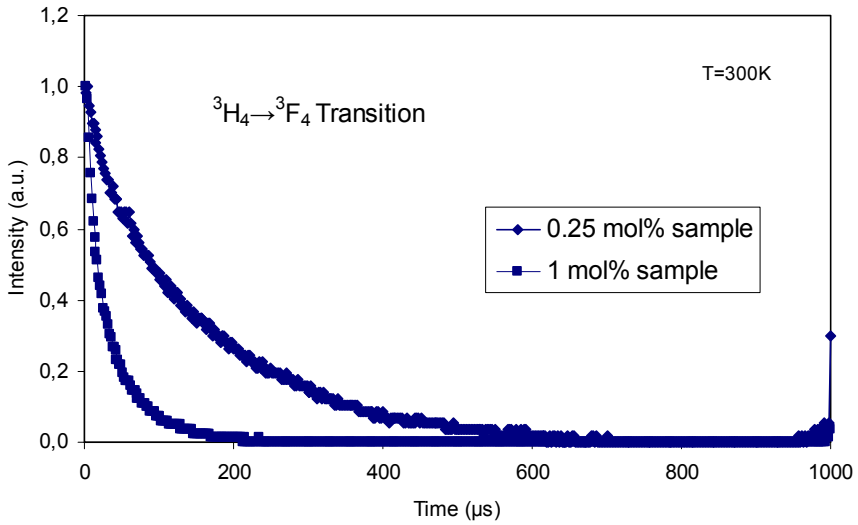

Fig. 5.9. Measured fluorescence decay curves of the $^3H_4$ level for the glass samples.

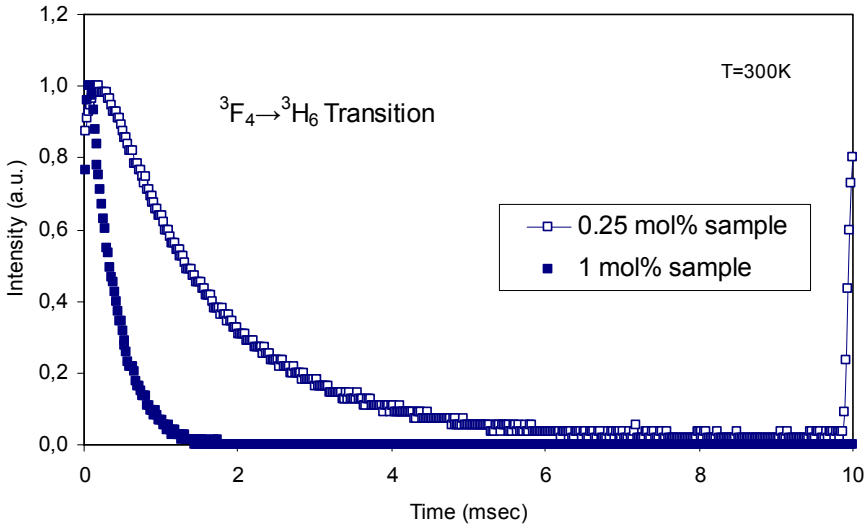

Fig. 5.10. Measured fluorescence decay curves of the $^3F_4$ level for the glass samples.

$^3H_4 \rightarrow {}^3F_4$ transition should be significantly lower than the fluorescence efficiency of the $^3H_4$ level (0.17) for the 1 mol% sample due to the increasing cross relaxation effect which boosts the nonradiative decay from $^3H_4$ to $^3F_4$. This point is supported by the fluorescence spectrum of the 1 mol% sample where the emission strength of the 1800 nm ($^3F_4 \rightarrow {}^3H_6$) band is three times that of the 1460 nm ($^3H_4 \rightarrow {}^3F_4$).

Table 5.7

Fluorescence lifetimes τ_F and fluorescence quantum efficiencies η for the Tm_2O_3:(0.85)TeO_2-(0.15)WO_3 samples.

Tm_2O_3:(0.85)TeO_2-(0.15)WO_3 sample	$\tau_{F\,(\mu s)}$ $^3H_4$	$\tau_{F\,(ms)}$ $^3F_4$	η $^3H_4$	η $^3F_4$
0.25 mol%	218	1.86	0.72±0.02	0.95±0.01
1 mol%	51	0.35	0.17±0.004	0.18±0.002

Table 5.8

Calculated branching ratios β of the $^3H_4$ level

	β ($^3H_4 \rightarrow$)		
Tm_2O_3:TeO_2-WO_3	$^3H_5$	$^3F_4$	$^3H_6$
0.25 mol%	0.02	0.08	0.9
1 mol%	0.02	0.08	0.9

Table 5.9 lists the emission cross sections σ_{em} for the peaks in the fluorescence spectra calculated using the Fuchtbauer-Ladenburg equation (Eqn. (5.8)). In obtaining σ_{em}, spontaneous emission rates *A(J,J')* based on mean intensity parameters (see Table 5.6) were used. Comparing the measured emission cross section value with those of other thulium doped telluride glasses[201, 208] and thulium doped crystals[148, 199], higher values for Tm^{3+}:(0.85)TeO_2-(0.15)WO_3 reveal the potential of this glass for laser and amplifier systems.

Table 5.9

Stimulated emission cross sections for the peaks in the fluorescence spectra.

Tm_2O_3:(0.85)TeO_2-(0.15)WO_3 Sample	σ_{se} (10^{-21} cm^2)		
	1460 nm	1649 nm	1808 nm
0.25 mol%	3.54±0.09	5.83±0.06	5.73±0.06
1 mol%	3.92±0.1	-	7.40±0.19

The critical distance parameter R_o, which is an indicator of the strength of cross relaxation mechanism in the material, was also calculated for the glass samples using the fluorescence decay data and the average radiative lifetime for the $^3H_4$ level (see Table 5.6). The calculation was based on the diffusion-limited relaxation model of the energy transfer between Tm^{3+} ions during the cross relaxation process (see Section 5.2). First, interaction parameter C (1.10 x 10^{-39} cm^6s^{-1} for 0.25 mol% and 3.08 x 10^{-39} cm^6s^{-1} for 1.0 mol% sample) and diffusion constant D (1.74 x 10^{-11} cm^2s^{-1} for 0.25 mol% and 1.40 x 10^{-11} cm^2s^{-1} for 1.0 mol% sample) were determined by applying a nonlinear least-squares fit to the tail of the $^3H_4$ fluorescence decay curve for each sample with Eqn. (5.10) where Eqn. (5.11) was substituted for $\prod(t)$. Figure 5.11 shows the curve fitting applied in the case of the 1.0mol% sample. Using the calculated C parameter for each sample and the average value of τ_R (305 μsec), a mean value of, 9.1 ± 0.8 Å was computed for R_o. Other examples of mean R_o determined for thulium doped materials are 7.3 Å for $Ge_{30}Ga_2As_6S_{62}$ glass[202], 17.9 Å for $0.7TeO_2$:$0.3CdCl_2$ glass[152] and 10.2 Å for LuAG crystal[199].

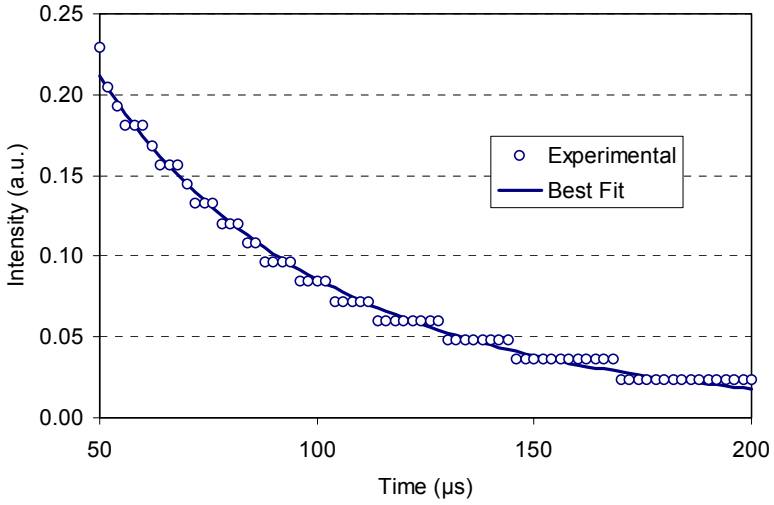

Fig. 5.11. Measured fluorescence decay of the $^3H_4 \rightarrow {}^3F_4$ transition and the calculated best fit to equations (5.10) and (5.11) for the 1.0mol% Tm_2O_3 :$(0.85)TeO_2$-$(0.15)WO_3$ sample.

5.5 Summary

In this chapter, an introduction to spectroscopic study of photonic materials with a detailed description of data analysis was provided in Sections 5.1 and 5.2. Then, spectroscopic investigations of two different materials Tm^{3+}:LuAG crystal and thulium-doped telluride-based glass Tm^{3+}:TeO_2-WO_3 were described in Sections 5.3 and 5.4, respectively.

We first presented in Section 5.3 the results of spectroscopic measurements and analyses done on two Tm:LuAG crystals with Tm^{3+} ion concentrations of 0.5 at. % and 5 at. %. Average values of 1041±143 μs and 17.7±3.4 ms were determined for the radiative lifetimes of the $^3H_4$ and $^3F_4$ levels based on the Judd-Ofelt theory. The fluorescence lifetime of the $^3H_4$ level was measured to be 851 μs and 42.3 μs for the 0.5% and 5% TmLuAG samples, respectively, showing that the strength of cross relaxation increases with concentration. The fluorescence spectra further showed that the 1470-nm ($^3H_4 \rightarrow {}^3F_4$) emission vanished for the 5% sample, while its strength was 60% of the 1800-nm ($^3F_4 \rightarrow {}^3H_6$) emission for the 0.5% sample, also supporting the role of cross relaxation. In the same concentration range, the lifetime of the $^3F_4$ level decreased from 11.2 ms to 7.1 ms due to the enhancement of the nonradiative decay mechanisms. Using the fluorescence data and the results of the Judd Ofelt analysis, an average value of 1.2±0.2 x 10^{-21} cm^2 was obtained for the emission cross section at 2023 nm. Finally, the average value of the critical distance parameter R_o was determined to be 10.2±0.8 Å by using the diffusion-limited relaxation model for cross relaxation.

Then in Section 5.4, we gave a detailed account of the spectroscopic properties of the Tm_2O_3:(0.85)TeO_2-(0.15)WO_3 glass in the near infrared. Based on the absorption spectra, average radiative lifetimes of 305 ± 7.5 μsec ($^3H_4$) and 1.95 ± 0.02 msec ($^3F_4$) were calculated by using the Judd-Ofelt analysis. Fluorescence lifetimes of the $^3F_4$ and $^3H_4$ levels were further measured. The luminescence efficiency of both the $^3H_4$ (0.72→0.17) and $^3F_4$

(0.95→0.18) levels were found to decrease substantially due to an increase in the nonradiative decay with higher doping concentration. The main conclusion of this study is that the Tm_2O_3:(0.85)TeO_2-(0.15)WO_3 glass is a potentially important candidate for mid-IR emission systems with the 0.25 mol% Tm_2O_3 doping concentration being suitable for fiber-optic amplifiers operating around 1.5 micron and 1.0 mol% suitable for laser systems near 2.0 micron. This conclusion was supported by the fluorescence spectra of the 0.25 mol% and 1.0 mol% samples and the calculated emission cross sections ($3.73 \pm 0.1 \times 10^{-21}$ cm^2 at 1460 nm and $6.57 \pm 0.07 \times 10^{-21}$ cm^2 at 1808 nm).

Chapter 6

Lasing In Neodymium-Doped Telluride Glass

6.0 Introduction

Ever since the first demonstration of lasing in glass by E. Snitzer in 1961[213], a lot of effort has gone into the development of laser glasses. These offer the advantages of lower cost and simpler preparation in comparison with single-crystal laser hosts. If lasing can be achieved with glasses at desired wavelengths, it will be possible to build versatile laser sources much more easily and at a much lower cost. In addition, glasses can be drawn into fibers to enable power scaling. To date, lasing in a thulium-doped bulk (as opposed to fiber) glass has not been demonstrated. Telluride-based glasses have attracted increasing attention in recent years as potential hosts for laser glass owing to several favorable characteristics such as a wide transparency range (0.35-5.0 μm), high rare-earth solubility, lower non-radiative decay rates than silicates, phosphates or germanates, high refractive index, high emission and absorption cross sections, good stability, and resistance to corrosion[204, 214, 215]. This has motivated our group to experiment on thulium-doped telluride glasses as potential 2-micron laser sources which would make such lasers much less costly and more practical to build. As a matter of fact, our group has been investigating the spectroscopy of thulium-doped telluride-based glasses[152, 201, 211] in a joint effort with Istanbul Technical University (ITU) where the glass samples have been prepared. In our studies, we have attempted to obtain lasing in thulium-doped telluride-tungstate

(Tm^{3+}:TeO_2-WO_3) bulk glass. Our trials with thulium-doped glass were not successful, but we obtained lasing when the telluride-based host was doped with neodymium (Nd^{3+})[216].

6.1 Lasing Trials with Tm^{3+}: TeO_2-WO_3 Glass

The main goal of our experiments with telluride-based glass has been to obtain home-made laser glass. To begin with, in order to assess the lasing capacity of thulium-doped samples, an x-cavity pumped by a pulsed Ti-sapphire laser was set-up. This cavity was tested first with 4 % Tm:YAP crystal, which was used in cw diode-pumped and low-threshold lasing experiments described in Chapter 3. The pump operated at 795 nm with a repetition rate of 1 kHz, pulsewidth varying from 150 ns to 60 ns with increasing power. The schematic of the resonator is shown in Fig. 6.1. The x-cavity consisted of two curved mirrors (M1 and M2, R=10 cm), a one-meter long folded high reflector arm consisting of two flat high reflectors (M4, M5), and a one-meter long folded output arm made of a flat high reflector M3 and two alternative output couplers (OC) (2% and 6%). The laser mode spot size was estimated to be 28.5 μm (assuming operation at the center of the stability region), using the standard ABCD matrix method. The pump waist was measured by the knife edge technique to be 26 μm. As expected lasing was observed with the 4 % Tm:YAP crystal and the power efficiency results for both OCs are shown in Fig. 6.2. Incident threshold energy was 19 μJ and 25 μJ for the 2% and 6% OC, respectively. Next, thulium-doped telluride-tungstate glass samples (0.25 mol% and 1.0 mol% Tm_2O_3-doped $(0.85)TeO_2$-$(0.15)WO_3$) were tested in the same resonator cavity, however no lasing was observed. Then, to test the suitability of the telluride-tungstate glass host (TeO_2-WO_3) for lasing, neodymium-doped samples were prepared and used in lasing trials.

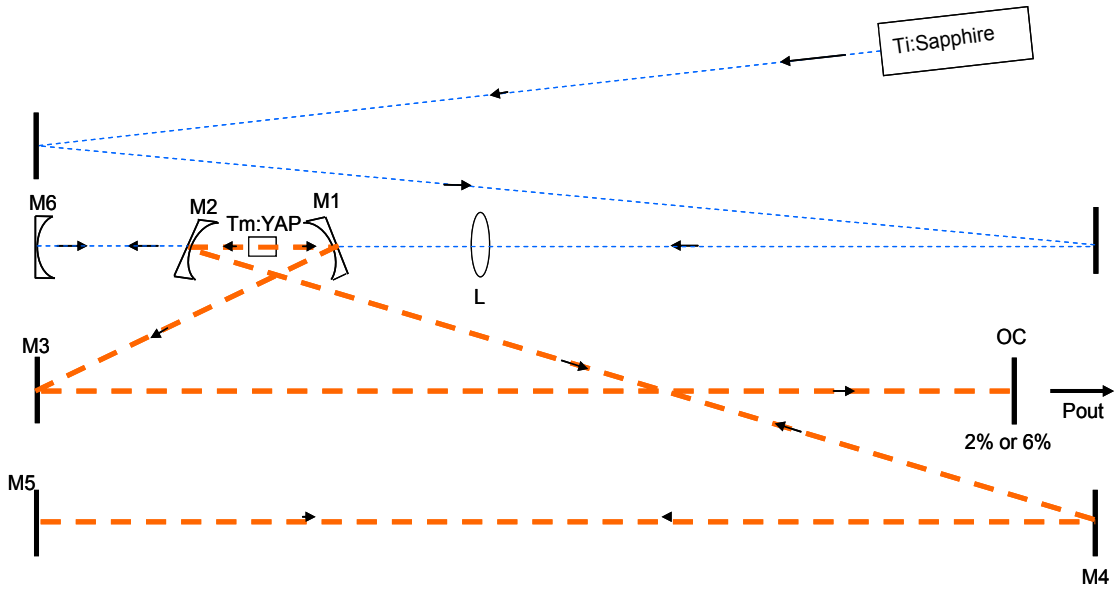

Fig. 6.1. X-cavity set-up for lasing trials in glass.

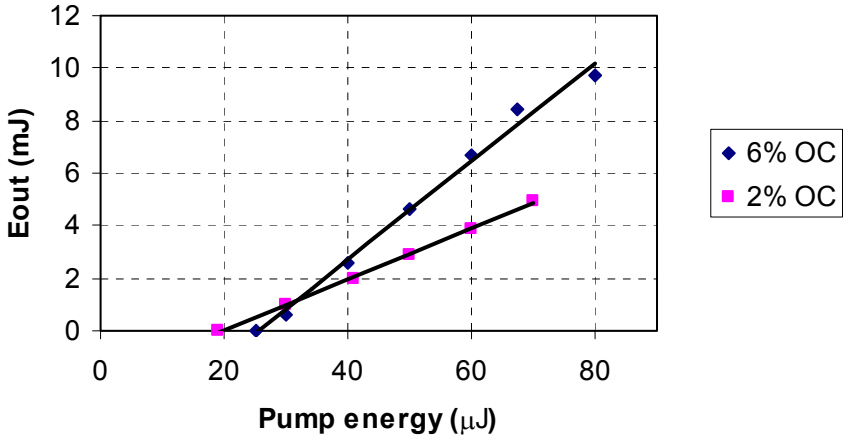

Fig. 6.2. Lasing performance results of 4 % Tm:YAP inside x-cavity.

6.2 Lasing at 1065 nm in Bulk Nd^{3+}-Doped Telluride-Tungstate glass

Among the rare-earth-doped glasses, those doped with Nd^{3+} ions have been most widely investigated due to the highly efficient $^4F_{3/2} \rightarrow {}^4I_{11/2}$ transition near 1.06 μm. In fact, neodymium-doped silicate and phosphate-based bulk laser glasses have been commercially available for a long time. Lasing has also been obtained in various other bulk glasses doped with neodymium such as fluorides[217, 218], chalcogenides[219], aluminosilicates[220], germanates[221], and telluride-based[222-224] glasses. Furthermore, it has been reported that, based on the Judd-Ofelt analysis, telluride glasses have the highest emission cross sections among the Nd^{3+}-doped pure oxide glasses[214]. To date, lasing has been reported in Nd^{3+}[225], Er^{3+}[226], and Tm^{3+}[215, 227] -doped telluride fibers as well as Nd^{3+}-doped bulk telluride glasses[222-224]. In the case of neodymium-doped bulk tellurite glasses, Michel et al. reported lasing in the host $(0.955)TeO_2$-$(0.45)Li_2O$ with an absorbed threshold power of 20 mW and a slope efficiency of 14% by using an argon-ion pump laser at 5145 Å[222]. In another study, Lei et al. obtained gain-switched operation in(0.866)TeO2-(0.84)BaO-$(0.04)Na_2O$ by using a Ti:sapphire pump laser at 804 nm. The corresponding threshold pump energy and slope efficiency were 4.2 mJ and 14.7%, respectively [223].

In this study, we obtained for the first time to our knowledge, lasing in a new, Nd^{3+}-doped telluride-based bulk glass (Nd^{3+}-telluride) with the composition Nd_2O_3:$(0.8)TeO_2$-$(0.2)WO_3$[216]. Lasing was achieved by using samples with two different doping concentrations: 0.5 mol.% and 1.0 mol.% Nd_2O_3 doped $(0.8)TeO_2$-$(0.2)WO_3$ (hereafter referred to as the 0.5 mol% and 1.0 mol% sample). During gain-switched operation, the 0.5 mol% sample produced 11 μJ of output energy at 1065 nm with 114 μJ of pump. In the case of the 1.0 mol% sample, nearly the same output energy was obtained with 129 μJ of pump energy. From the laser threshold data, the average emission cross section at 1065 nm was determined to be $2.0\pm0.13 \times 10^{-20}$ cm^2. The spectroscopic properties of the samples

were further investigated by using the Judd-Ofelt theory. By using the absorption and emission data, the average emission cross section was determined to be 3.23±0.09 x 10^{-20} cm^2 at 1065 nm, in good agreement with the result obtained from the laser threshold analysis.

6.2.1 Experiment

The glass samples were prepared by melting the powder mixtures of Nd_2O_3 (99.9% purity), TeO_2 (99.999% purity), and WO_3 (99% purity) inside a platinum crucible in an air-filled furnace at 800 ºC. The glass melts were then rapidly quenched in a stainless steel mold in air at room temperature. Afterwards, glass samples were annealed at 250 ºC to release the internal thermal stresses. The powder mixtures contained 0.5 mole and 1.0 mole of Nd_2O_3 to 100 moles of (0.8)TeO_2-(0.2)WO_3 for the 0.5 mol% and 1.0 mol% samples, respectively. After polishing, the lengths of the samples were 4.1 mm (0.5 mol%) and 3.7 mm (1.0 mol%). Using the measured density of 5.82 gm/cm^3, the Nd^{3+} ion concentration was determined to be 2.02 x 10^{20} cm^{-3} for the 0.5 mol% and 3.98 x 10^{20} cm^{-3} for the 1.0 mol% sample. The small-signal single-pass absorption was measured to be 92% and 99% at the pump wavelength of 805 nm for the 0.5 and 1.0 mol% samples, respectively.

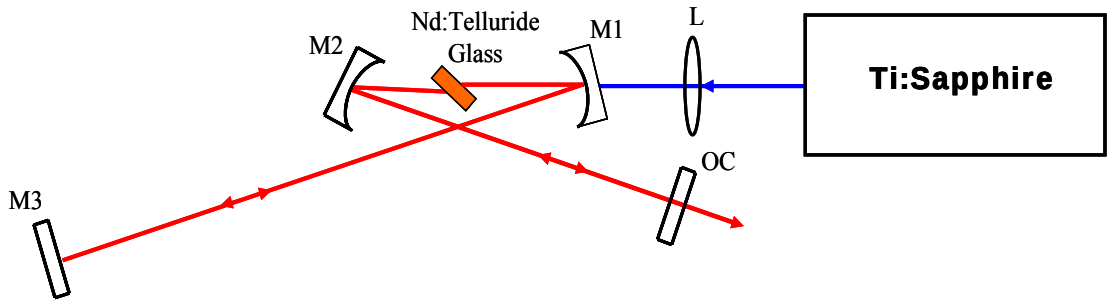

Fig. 6.3. Schematic of the gain-switched (Nd^{3+}:(0.8)TeO_2-(0.2)WO_3) glass laser.

Fig. 6.3 shows the schematic of the laser setup. The astigmatically compensated x-cavity consisted of two curved mirrors (M1 and M2, R=10 cm), a flat high reflector (M3), and a flat output coupler which had a transmission of 3.3%. The threshold pump energy was also measured by replacing the output coupler with a high reflector to estimate the passive cavity losses. The cavity was end-pumped by a pulsed 805-nm Ti:sapphire laser operating at a repetition rate of 1 kHz. The pump beam was focused with a lens (L) of 10-cm focal length. The pump beam waist was measured to be 29 μm by using the knife-edge method. The high reflector and the output coupler arms had respective lengths of 100 cm and 54 cm, giving an estimated laser mode waist of 21 μm near the middle of the stability range. In the experiments, the output pulse profiles of the glass laser were measured with a Si detector (response time= 1ns) and a digital storage oscilloscope. Laser efficiency measurements were made with a power meter.

For spectroscopic characterization of the glass samples, a commercial spectrophotometer was used to measure the absorption spectra. Emission spectra were further measured with a ½-m Czerny-Turner-type monochoromator. To determine the fluorescence lifetime of the $^4F_{3/2}$ level, each sample was excited at 805 nm with a Ti:sapphire laser emitting 60-ns long pulses at a repetition rate of 1 kHz. The time-dependent fluorescence signal was measured by using a germanium detector with a response time of 4.5 μs.

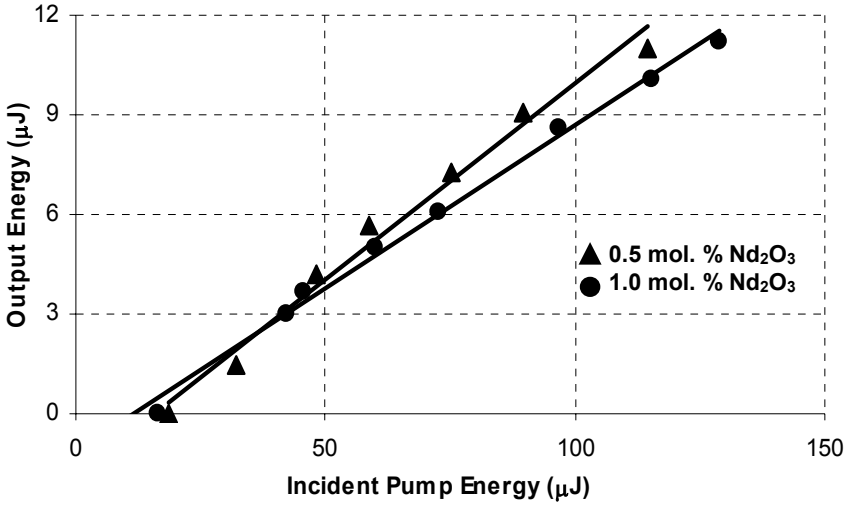

Fig. 6.4. Energy efficiency curves for the 0.5 mol% and 1.0 mol% Nd^{3+}:$(0.8)TeO_2$-$(0.2)WO_3$ glass samples. The output is at 1065 nm.

6.2.2 Results and Discussion

Fig. 6.4 shows the laser performance results for the Nd^{3+}:telluride glass samples at 1065 nm during gain-switched operation. The threshold incident pump energies were 19 μJ and 16 μJ for the 0.5 mol% and 1.0 mol% samples, respectively. The slope efficiency for the 0.5 mol% sample was 12% with respect to the incident pump energy, a little better than the value (10%) obtained for the 1.0 mol% sample. Our results are in reasonable agreement with the slope efficiency of 14% reported by Michel et al.[222] and 14.7% reported by Lei et al. for other bulk telluride-based glasses[223]. When the output coupler was replaced with a high reflector, the threshold pump energy decreased to 13 μJ for the 0.5 mol% sample and to 12 μJ for the 1.0 mol% sample. Assuming that the threshold pump energy is directly proportional to (L+T), (L=roundtrip cavity loss, T= output coupler transmission), the round trip loss was estimated to be 8.1% and 9% for the 0.5 mol% and 1.0 mol% samples, respectively. By using a 1064-nm Nd:YAG laser, the loss of the samples was

further determined directly from transmission measurements. The results (8.5% and 8.7% for the 0.5 and 1.0 mol% sample, respectively) were in very good agreement with those determined from the threshold analysis.

Figures 6.5(a) and (b) show the temporal profile of the output pulses for the 0.5 and 1.0 mol% samples, respectively, at different pump energies. We note that output pulsewidths are significantly shorter than the fluorescence lifetime which is in the microsecond range. This is a clear indication of gain-switched laser operation. The output pulsewidth was further found to vary with pump energy. In the case of the 0.5 mol% sample, for example, the output pulsewidth decreased from 1270 to 270 ns as the pump energy was increased from 24 to 118 μJ (pump pulsewidth= 60 ns). A similar trend was observed with the 1.0 mol% sample where the pulsewidth decreased from 2006 to 327 ns when the pump energy was increased from 18 to 115 μJ. Furthermore, Fig. 6.6 shows the pump and output pulses together for the 1.0 mol% sample at a pump energy of 115 μJ. Note that there is a delay of 500 ns between the two pulses.

The threshold data were used to estimate the emission cross section σ_L for the Nd^{3+}-telluride glass at the lasing wavelength. Assuming a square-shaped pump pulse, the threshold pump energy for a pulsed laser is approximated by[2]

$$E_{th} = \frac{P_{th}\tau_p}{1-\exp\left(\frac{-\tau_p}{\tau}\right)} \tag{6.1}$$

where P_{th} is the threshold pump power for continuous wave operation, τ_p is the pump pulsewidth and τ is the fluorescence lifetime. In the limit where the pump pulsewidth is much shorter than the fluorescence lifetime (which was the case in our experiment with τ_p=60 ns, τ=142 μs and 105.5 μs for the 0.5 mol% and 1.0 mol% sample, respectively),

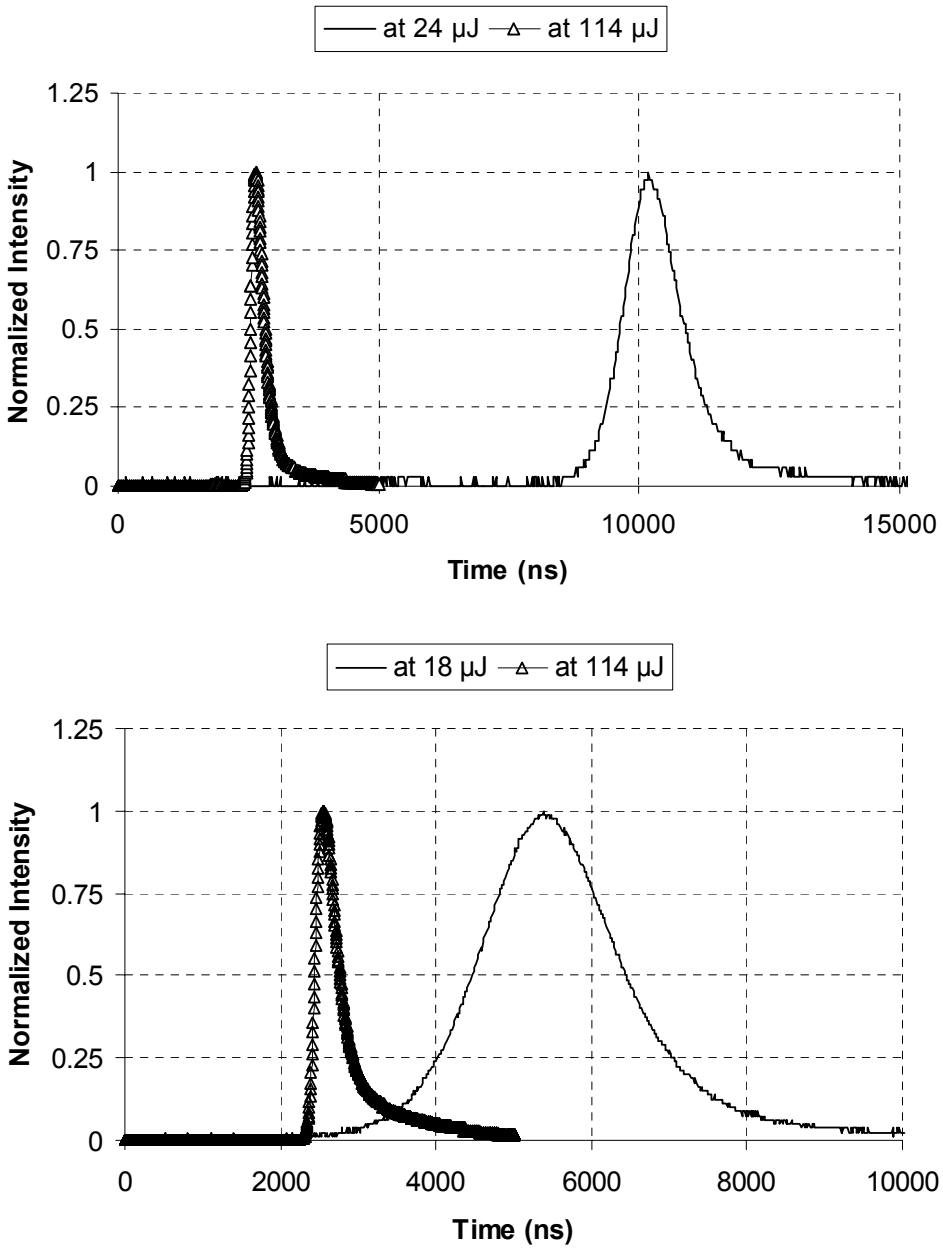

Fig. 6.5. Output pulse profiles of the (Nd^{3+}:(0.8)TeO_2-(0.2)WO_3) glass laser at different pump energies for the (a) 0.5 mol% and (b) 1.0 mol% samples.

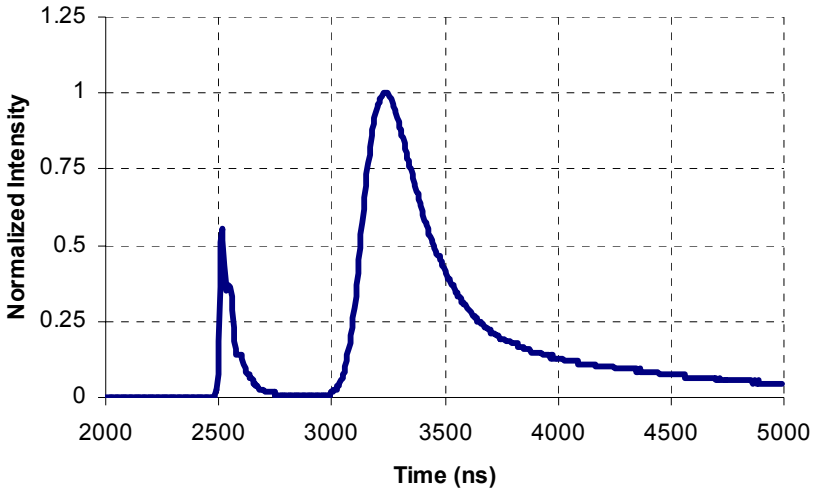

Fig. 6.6. Temporal profiles of the pump and laser pulses for the 1.0 mol% sample at a pump energy of 115 μJ. The 327-ns-wide laser pulse follows the pump pulse with a delay of 500 ns.

$E_{th} \approx P_{th}\tau$ since $\exp(-\tau_p/\tau) \approx 1-(\tau_p/\tau)$. Then using the formula for threshold pump power for four-level systems (Eq. (2.4)), the incident threshold pump energy will be given by

$$E_{th} = \frac{\pi h \nu_p (w_L^2 + w_p^2)(T + L)}{4\eta_a \sigma_L}, \tag{6.2}$$

where $h\nu_p$ is the pump photon energy, w_L is the laser spotsize, w_P is the pump spot size, and η_a is the absorption at the pump wavelength. The root-mean-squared values of the pump and laser beams (w_P=30 μm, w_L=23 μm) inside the gain medium were used for a more accurate determination of the emission cross section. With E_{th}= 13 μJ, T=0 (for the high reflector), L =0.081, η_a=0.92, the emission cross section σ_L for the 0.5 mol% sample was determined to be 1.87 x 10^{-20} cm^2 at 1065 nm. Similarly, by using E_{th}=12 μJ, T=0 (for the

high reflector), L=0.09, and η_a=0.99, a σ_L value of 2.13 x 10^{-20} cm^2 was calculated for the 1.0 mol% sample at 1065 nm. The average emission cross section was thus estimated to be 2.0±0.13 x 10^{-20} cm^2 for the Nd_2O_3:(0.8)TeO_2-(0.2)WO_3 glass from the laser threshold data.

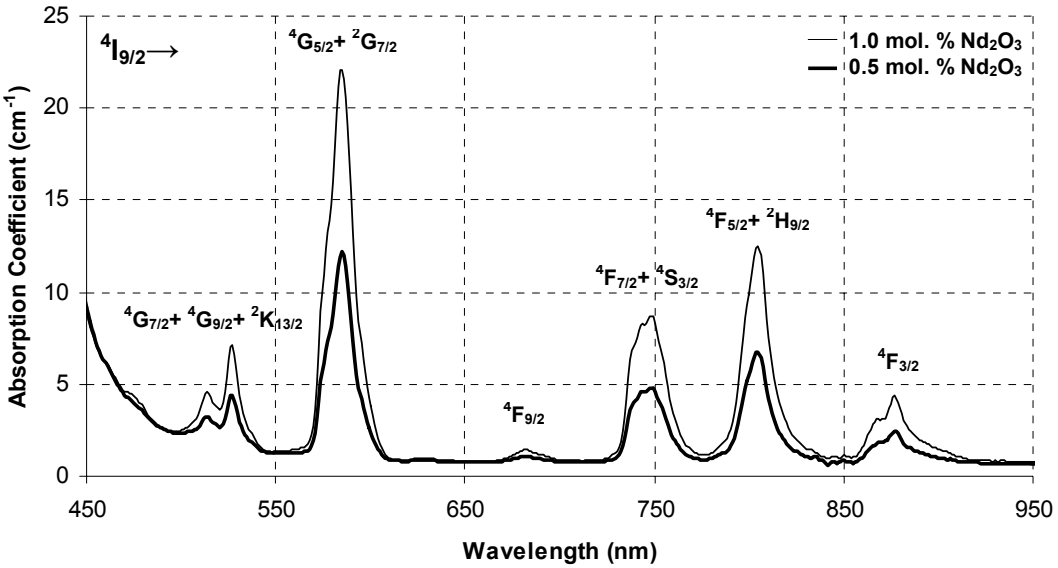

Fig. 6.7. Absorption spectra of the 0.5 mol% and 1.0 mol% Nd_2O_3:(0.8)TeO_2-(0.2)WO_3 glass samples.

In the Judd-Ofelt analysis, the absorption characteristics of the samples were first investigated. Fig. 6.7 shows the absorption spectra for the 0.5 mol% and 1.0 mol% samples. As expected, the shapes and positions of the bands are similar to other Nd^{3+}-doped glasses[214, 228, 229]. Six separate peaks are visible in each spectrum and the corresponding transitions from the ground state $^4I_{9/2}$ are indicated for each one in Fig.6.7. To apply the Judd-Ofelt analysis, the integrated absorption coefficient measured for each peak in the spectra was equated to the theoretical expression calculated for electric-dipole

transitions. Only the contribution from electric-dipole transitions was taken into account since this is the dominant process in Nd^{3+}-doped systems. The best-fit values of the intensity parameters were calculated to be Ω_2=4.71±0.2%, Ω_4=4.06±3.7%, and Ω_6=3.89±1.4%. The radiative lifetime for the $^4F_{3/2}$ level was then determined to be 149.4±0.36 μs by calculating the spontaneous emission rate for electric-dipole transitions from the $^4F_{3/2}$ level to the lower levels by using the calculated intensity parameters. Note that, similar values in the 141-243 μs range have been reported for the $^4F_{3/2}$ radiative lifetime in other Nd^{3+}-doped telluride-based glasses[214, 228, 229].

Fig. 6.8 shows the emission spectrum of the 1.0 mol% sample in the 1000-1500 nm range. The spectrum of the other sample was nearly identical. The data from the emission spectra and the spontaneous emission rates for the $^4F_{3/2}$ level calculated by the Judd-Ofelt analysis were used to determine the emission cross section σ_L at the operating wavelength (1065 nm) of the laser. Using the Fuchtbauer-Ladenburg equation[195], σ_L was calculated to be 3.23±0.09 x 10^{-20} cm^2 (average of the two samples) at 1065 nm. In

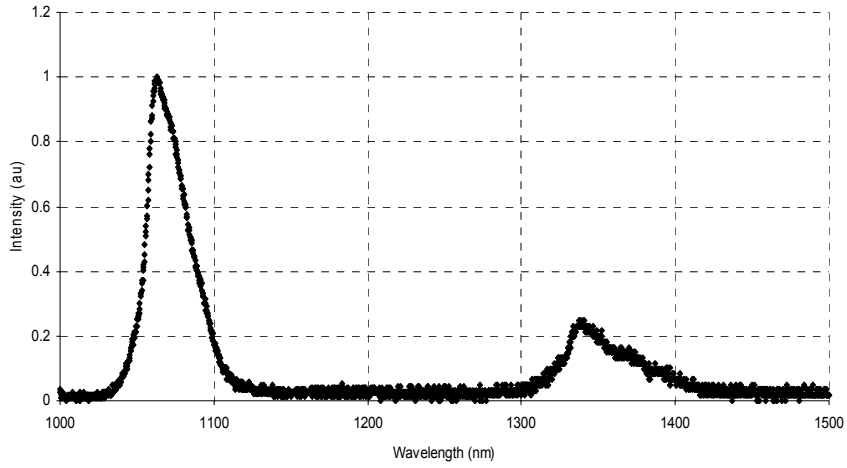

Fig. 6.8. Emission spectrum of the 1.0 mol% Nd_2O_3:(0.8)TeO_2-(0.2)WO_3 glass sample in the 1000-1500 nm range.

comparison, emission cross sections of 4.7 x 10^{-20} cm^2[222] and 3.94 x 10^{-20} cm^2[223] were reported for other telluride-based hosts using the Judd-Ofelt method. Overall, our value is in agreement with the range of emission cross section values (3.1-5.1 x 10^{-20} cm^2) determined with spectroscopic techniques for other Nd^{3+}-doped telluride-based glasses as reported by Weber et al[214]. Furthermore, the emission cross section (2.0±0.13 x 10^{-20} cm^2) determined from the laser threshold data is in reasonable agreement with the spectroscopic result. Finally, Figs. 6.9(a) and (b) show the recorded fluorescence decay curves for the 0.5 and 1.0 mol% samples, respectively. The fluorescence lifetime of the $^4F_{3/2}$ level was measured to be 142 μs and 105.5 μs for the 0.5 and 1.0 mol% samples, respectively. The resulting luminescence efficiency which is the ratio of actual fluorescence lifetime to the radiative lifetime was determined to be 0.95 and 0.71 for the 0.5 and 1.0 mol% samples. The results indicate that the rate of non-radiative decay begins to increase as the doping concentration is increased from 0.5 mol% to 1.0 mol%.

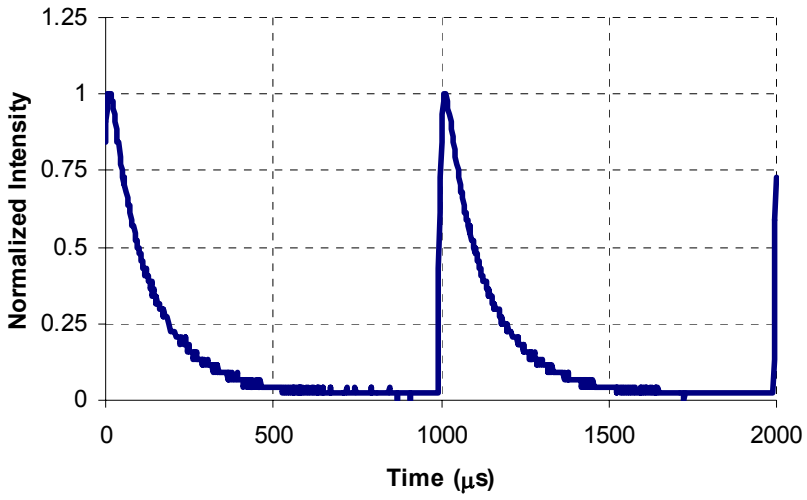

Fig. 6.9(a). Fluorescence decay curves for the 0.5 mol% Nd_2O_3:(0.8)TeO_2-(0.2)WO_3 glass sample at 1064 nm.

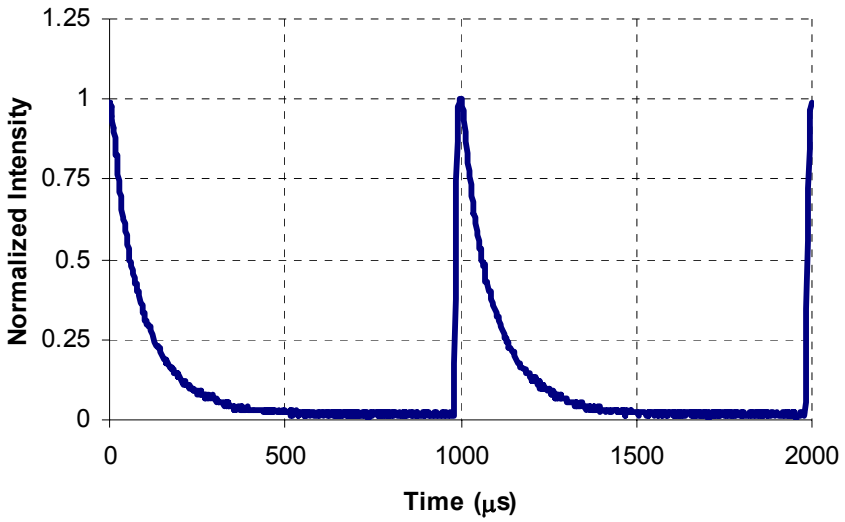

Fig. 6.9(b). Fluorescence decay curves for the 1.0 mol% Nd_2O_3:(0.8)TeO_2-(0.2)WO_3 glass sample at 1064 nm.

6.2.3 Summary

We have described the first experimental demonstration of lasing in bulk Nd^{3+}-doped (0.8)TeO_2-(0.2)WO_3 glass at 1065 nm. By using the 0.5 mol% sample, we obtained 11 μJ of output energy with a slope efficiency of 12% by using 114 μJ of pump energy. The corresponding incident pump threshold energy was 19 μJ. The average emission cross section of the doped glass determined from the lasing threshold data was in good agreement with that obtained from the spectroscopic analysis based on the Judd-Ofelt theory. Overall, the results suggest that the new tellurite-based laser glass developed in this study should be potentially important in the development of new efficient bulk glass or fiber lasers.

Chapter 7

CONCLUSIONS

In this thesis, experimental development of advanced solid-state lasers operating in the 2-μm region have been investigated with a focus on thulium-doped (Tm^{3+}-doped) systems.

To begin with, two studies were conducted on continuous-wave Tm^{3+}:$YAlO_3$ (Tm:YAP or Tm:YAlO) lasers which are important lasers for medical and remote sensing applications with free running wavelengths near the absorption peak of water at 1.94 μm. The aim of our experimental studies was to optimize the power performance of end-pumped Tm:YAP lasers. In the first case, a detailed investigation of the cw power performance of diode single-end-pumped Tm:YAP lasers was performed as a function of thulium ion concentration, which is a critical design parameter. Samples with 1.5, 3, and 4% doping concentration were pumped at 797 nm with a fiber-coupled diode laser and the best performance was obtained with the 1.5% Tm:YAP sample. Using the laser threshold data, an emission cross section of 4.2×10^{-21} cm^2 was estimated at 1.94 μm for the Tm^{3+}:$YAlO_3$ crystal in good agreement with previously published results. Spectroscopic measurements and rate-equation analysis indicate that cross relaxation is effective in samples with 1.5% Tm^{3+} ion concentration and that in single-end-pumped configurations, use of crystals with more than 4% doping concentration may cause degradation in laser performance due to higher reabsorption losses and faster non-radiative decay rates.

In the second experimental study on cw Tm:YAP lasers, low-threshold operation at 1945 nm with threshold pump powers as low as 10 mW was obtained with a z-cavity under Ti:sapphire pumping. Low-threshold operation served the goal of making cost-effective

and less power consuming systems. The achieved threshold was the lowest result reported to date. The output could be tuned in the 1842-1994 nm range. Two alternative cavity geometries with R=5 cm and R=10 cm mirrors were tested and R=10 cm configuration yielded a lower pumping threshold. Each configuration produced nearly the same slope efficiency, suggesting that the amount of total resonator loss and the degree of mode overlap between the pump and the resonator beams were similar. A theoretical calculation assuming operation at the center of the stability range predicted nearly equal threshold powers for the two configurations.

Next, a project was undertaken in collaboration with a biomedical group from Bogazici University to develop a surgical system based on the cw Tm:YAP laser. The ultimate aim of this project is to obtain a laser tissue welding (fusion) system exploiting the high interaction of tissues with the laser radiation due to the absorption peak of water. For experimenting on tissues, the diode-pumped cw Tm:YAP laser has been rebuilt in a portable configuration and its output was coupled into a fiber for directing radiation on target tissue samples. Stable operation was achieved where 84% of the laser output was coupled through the delivery fiber. Based on the preliminary results of experiments testing interaction of laser radiation with animal tissues and laser welding of incisions on live rat skin, it has been reported that incident intensity around 15 W/cm^2 is suitable for laser welding while for coagulation and ablation higher intensities are required.

In spectroscopic studies, two potentially important new laser materials were investigated. In the first study, Tm:LuAG, which is an isotropic garnet with a demonstrated lasing ability at the free running wavelength of 2.02 μm, was characterized. Two Tm:LuAG crystals with Tm^{3+} ion concentrations of 0.5 at. % and 5 at. % were used in measurements. Radiative lifetimes of 1041±143 μs ($^3H_4$) and 17.7±3.4 ms ($^3F_4$) were calculated by employing the Judd-Ofelt technique. The fluorescence lifetime of the $^3H_4$ level sharply decreased from 851 μs for the 0.5% sample to 42.3 μs for the 5% sample due to cross

relaxation. The fluorescence spectra further showed that the 1470-nm ($^3H_4 \rightarrow {}^3F_4$) emission vanished for the 5% sample, while its strength was 60% of the 1800-nm ($^3F_4 \rightarrow {}^3H_6$) emission for the 0.5% sample, also supporting the role of cross relaxation. An average value of 1.2±0.2 x 10^{-21} cm^2 was obtained for the emission cross section at 2023 nm.

In the second spectroscopic work, a detailed characterization of the Tm_2O_3:(0.85)TeO_2-(0.15)WO_3 glass was performed in order to investigate its lasing potential in the near to mid-infrared region since glasses are attractive host materials due to the ease and low cost of preparation. In the study, average radiative lifetimes of 305 ± 7.5 μsec ($^3H_4$) and 1.95 ± 0.02 msec ($^3F_4$) were calculated by using the Judd-Ofelt analysis. The luminescence efficiency of both the $^3H_4$ (0.72→0.17) and $^3F_4$ (0.95→0.18) levels decreased substantially due to an increase in the nonradiative decay with higher doping concentration. The fluorescence spectra of the samples and the calculated emission cross sections (3.73 ± 0.1 x 10^{-21} cm^2 at 1460 nm and 6.57 ± 0.07 x 10^{-21} cm^2 at 1808 nm) indicated the high potential of this material for emission systems around 1.5 μm and 2.0 μm.

Lasing trials in thulium-doped Tm_2O_3:(0.85)TeO_2-(0.15)WO_3 glass samples were conducted with an x-cavity under pulsed Ti:sapphire pumping. There was no success with thulium-doped samples, so to further asses the lasing potential of the TeO_2-WO_3 glass as a laser host, neodymium-doped samples were tested and lasing at 1065 nm was successfully demonstrated. Lasing was achieved with two samples, one with 0.5 mol% and the other with 1.0 mol% Nd_2O_3 doping. By using the 0.5 mol% sample, we obtained 11 μJ of output energy with a slope efficiency of 12% by using 114 μJ of pump energy. The emission cross section calculated with a laser threshold analysis (2.0±0.13 x 10^{-20} cm^2) was in good agreement with that (3.23±0.09 x 10^{-20} cm^2) obtained with a spectroscopic analysis.

As a consequence of efforts in developing advanced solid-state lasers operating in the 2-μm region, better performance in cw diode-pumped operation of Tm:YAP laser was obtained with 1.5% doping (Tm^{3+}) concentration compared to 3% and 4% and it was

observed that cross relaxation is already effective at 1.5% Tm^{3+} concentration. A cw Tm:YAP resonator which operated at a record low threshold of 10 mW under Ti:sapphire pumping was further designed. Spectroscopic characterization of potentially important new materials (laser crystal Tm:LuAG, potential laser glass Tm: TeO_2-WO_3) were performed and lasing in a novel telluride host $(0.8)TeO_2$-$(0.2)WO_3$ doped with neodymium was demonstrated for the first time. Furthermore, the preliminary results of a biomedical project indicated the high potential for a laser tissue welding system based on Tm:YAP laser. Overall, our experiments have shown that Tm:YAP is an efficient and stable candidate for many applications especially in medical surgery. Also, the TeO_2-WO_3 glass host prepared in our studies has potential for the development of new efficient bulk glass or fiber lasers.

BIBLIOGRAPHY

[1] T. H. Maiman, "Stimulated optical radiation in ruby," *Nature*, vol. 187, pp. 493-494, 1960.

[2] P. F. Moulton, "An Investigation of the Co:MgF_2 Laser System," *IEEE Journal of Quantum Electronics*, vol. 21, pp. 1582-1595, 1985.

[3] W. Koechner, *Solid-State Laser Engineering*, vol. 1, 4 ed. New York: Springer, 1996.

[4] M. J. Weber, "Multiphonon Relaxation of Rare-Earth Ions in Yttrium Orthoaluminate," *Phys. Rev. B*, vol. 8, pp. 54-64, 1973.

[5] M. J. Weber, M. Bass, T. E. Varitimos, and D. P. Bua, "Laser Action from Ho^{3+}, Er^{3+}, and Tm^{3+} in $YAlO_3$," *IEEE Journal of Quantum Electronics*, vol. QE-9, pp. 1079-1086, 1973.

[6] J. A. Caird, L. G. DeShazer, and J. Nella, "Characteristics of Room-Temperature 2.3-μm Laser Emission from Tm^{3+} in YAG and $YAlO_3$," *IEEE Journal of Quantum Electronics*, vol. QE-11, pp. 874-881, 1975.

[7] R. C. Stoneman and L. Esterowitz, "Efficient 1.94-μm Tm:YALO Laser," *IEEE Journal of Selected Topics in Quantum Electronics*, vol. 1, pp. 78-81, 1995.

[8] I. F. Elder and M. J. P. Payne, "Lasing in diode-pumped Tm:YAP, Tm,Ho:YAP and Tm,Ho:YLF," *Optics Communications*, vol. 145, pp. 329-339, 1998.

[9] T. Y. Fan, "Quasi-Three-Level Lasers," presented at Nato Advanced Study Institute on Solid State Lasers: New Developments and Applications, Elba, Italy, 1992.

[10] T. Y. Fan and R. L.Byer, "Modeling and CW Operation of a Quasi-Three-Level 946 nm Nd: YAG Laser," *IEEE JOURNAL OF QUANTUM ELECTRONICS*, vol. 23, pp. 605-612, 1987.

[11] W. P. Risk, "Modeling of longitudinally pumped solid-state lasers exhibiting reabsorption losses," *J.Opt.Soc.Am.B*, vol. 5, pp. 1412-1423, 1988.

[12] I. T. Sorokina, "Crystalline Mid-Infrared Lasers," in *Solid-State Mid-Infrared Laser Sources*, vol. 89, *Springer Topics in Applied Physics*, K. L. Vodopyanov, Ed. Berlin Heidelberg: Springer, 2003, pp. 255-349.

[13] R. C. Stoneman, "Eyesafe Rare Earth Solid-State Lasers," in *Solid-State Lasers and Applications*, vol. 119, *Optical Science and Engineering*, A. Sennaroglu, Ed. Boca Raton, Fla: CRC Press, 2007, pp. 529.

[14] L. F. Johnson, G. D. Boyd, and K. Nassau, "Optical maser characteristics of Ho^{3+} in $CaWO_4$," presented at IRE, 1962.

[15] L. F. Johnson, G. D. Boyd, and K. Nassau, "Optical maser characteristics of Tm^{3+} in $CaWO_4$," presented at IRE, 1962.

[16] L. F. Johnson, J. E. Geusic, and L. G. Van Uitert, "Coherent oscillations from Tm^{3+}, Ho^{3+}, Yb^{3+} and Er^{3+} ions in yttrium aluminum garnet," *Applied Physics Letters*, vol. 7, pp. 127, 1965.

[17] M. J. Weber, M. Bass, E. Comperchio, and R. L.A., "Ho^{3+} Laser Action in $YAlO_3$ at 2.119 μ," *IEEE Journal of Quantum Electronics*, vol. QE-7, pp. 497-498, 1971.

[18] L. F. Johnson, J. F. J. Dillon, and J. P. Remeika, "Optical Properties of Ho^{3+} Ions in Yttrium Gallium Garnet and Yttrium Iron Garnet," *Physical Review B*, vol. 1, pp. 1935-1936, 1970.

[19] E. P. Chickles, C. S. Naiman, R. C. Folweiler, and J. C. Doherty, "Stimulated Emission in Multiply Doped Ho^{3+}:YLF and YAG-A Comparison," *IEEE Journal of Quantum Electronics*, vol. QE-8, pp. 225-230, 1972.

[20] I. V. Klimov, I. A. Shcherbakov, and V. B. Tsvetkov, "Room-Temperature 2-μm Laser Action of Ho^{3+}-Doped YSGG, GSAG, YSAG, and YAG crystals," presented at Advanced Solid-State Lasers, New Orleans, LA, 1993.

[21] N. P. Barnes and K. E. Murray, "Flashlamp pumped, Ho:Tm:Cr:LuAG laser," presented at Advanced Solid-State Lasers, Memphis, TN, 1995.

[22] G. J. Quarles, A. Rosenbaum, C. L. Marquardt, and L. Esterowitz, "High-efficency 2.09 μm flashlamp-pumped laser," *Applied Physics Letters*, vol. 55, pp. 1062-1064, 1989.

[23] S. R. Bowman, M. J. Winings, R. C. Y. Auyeung, J. E. Tucker, S. K. Searles, and B. J. Feldman, "Laser and Spectral Properties of Cr, Tm, Ho - Yag at 2.1 Mu-M," *Ieee Journal of Quantum Electronics*, vol. 27, pp. 2142-2149, 1991.

[24] S. J. Hamlin, J. D. Myers, and T. R. Rexrode, "High-Ffficiency, Flashlamp-Pumped CTH:YAG Lasers Operated Above Room Temperature," presented at Advanced Solid-State Lasers, Santa Fe, NM, 1992.

[25] G. J. Quarles, A. Rosenbaum, C. L. Marquardt, and L. Esterowitz, "Efficient Room-Temperature Operation of a Flash-Lamp-Pumped, Cr,Tm-Yag Laser at 2.01 μm," *Optics Letters*, vol. 15, pp. 42-44, 1990.

[26] G. J. Quarles, A. Rosenbaum, C. L. Marquardt, and L. Esterowitz, "Efficient room-temperature operation of a flashlamp-pumped Cr;Tm:YAG laser at 2.014 μm," presented at Advanced Solid-State Lasers, Salt Lake City, Utah, 1990.

[27] J. F. Pinto and L. Esterowitz, "Tunable, flashlamp-pumped operation of a Cr;Tm:YAG laser between 1.945 and 2.014 μm," presented at Advanced Solid-State Lasers, Salt Lake City, Utah, 1990.

[28] G. J. Quarles, J. F. Pinto, and L. Esterowitz, "Broad Tunability of Flashlamp-Pumped, Tm-Activated Garnet Lasers," presented at Advanced Solid-State Lasers, Hilton Head, SC, 1991.

[29] S. R. Bowman, G. J. Quarles, and B. J. Feldman, "Upconversion Losses in Flashlamp-Pumped Cr,Tm:YAG," presented at Advanced Solid-State Lasers, Santa Fe, NM, 1992.

[30] T. Y. Fan, G. Huber, R. L. Byer, and P. Mitzscherlich, "Continuous-Wave Operation at 2.1-μm of a Diode-Laser-Pumped, Tm-Sensitized Ho:$Y_3Al_5O_{12}$ Laser at 300-K," *Optics Letters*, vol. 12, pp. 678-680, 1987.

[31] H. Hemmati, "2.07-μm Cw Diode-Laser-Pumped Tm,Ho-$YLiF_4$ Room-Temperature Laser," *Optics Letters*, vol. 14, pp. 435-437, 1989.

[32] G. J. Kintz, "Highly Efficient CW 2μm Laser," presented at Lasers and Electro-Optics Society Annual Meeting, 1990.

[33] R. Allen, L. Esterowitz, L. Goldberg, J. F. Weller, and M. Storm, "Diode-Pumped 2 μm Holmium Laser," *Electronics Letters*, vol. 22, pp. 947-947, 1986.

[34] H. Hemmati, "Efficient Holmium-Yttrium Lithium-Fluoride Laser Longitudinally Pumped by a Semiconductor-Laser Array," *Applied Physics Letters*, vol. 51, pp. 564-565, 1987.

[35] G. J. Kintz, L. Esterowitz, and R. Allen, "Cw Diode-Pumped Tm-3+, Ho-3+-Yag 2.1-μm Room-Temperature Laser," *Electronics Letters*, vol. 23, pp. 616-616, 1987.

[36] T. Y. Fan, G. Huber, R. L. Byer, and P. Mitzscherlich, "Spectroscopy and Diode Laser-Pumped Operation of Tm, Ho-Yag," *Ieee Journal of Quantum Electronics*, vol. 24, pp. 924-933, 1988.

[37] G. J. Kintz, R. Allen, and L. Esterowitz, "Continuous-wave laser emission at 2.02 mm from diode-pumped Tm3+:YAG at room temperature.," presented at Conference on Lasers and Electro-Optics, 1988.

[38] T. J. Kane and T. S. Kubo, "Diode-Pumped Single-Frequency Lasers and Q-Switched Laser Using Tm:YAG and Tm,Ho:YAG," presented at Advanced Solid-State Lasers, Salt Lake City, Utah, 1990.

[39] P. J. M. Suni and S. W. Henderson, "1-Mj/Pulse Tm-Yag Laser Pumped by a 3-W Diode-Laser," *Optics Letters*, vol. 16, pp. 817-819, 1991.

[40] C. P. Hale, S. W. Henderson, and P. J. M. Suni, "Single-Longitudinal-Mode and Q-Switched Diode-Pumped Tm,Ho:YLF Oscillators," presented at Advanced Solid-State Lasers, New Orleans, LA, 1993.

[41] S. R. Bowman, J. G. Lynn, S. K. Searles, B. J. Feldman, J. Mcmahon, W. Whitney, C. L. Marquardt, D. Epp, G. J. Quarles, and K. J. Riley, "Comparative Study of Diode-Pumped Two Micron Laser Materials," presented at Advanced Solid-State Lasers, New Orleans, LA, 1993.

[42] S. R. Bowman, J. G. Lynn, S. K. Searles, B. J. Feldman, J. Mcmahon, W. Whitney, D. Epp, G. J. Quarles, and K. J. Riley, "High-Average-Power Operation of a Q-Switched Diode-Pumped Holmium Laser," *Optics Letters*, vol. 18, pp. 1724-1726, 1993.

[43] G. J. Quarles, S. R. Bowman, J. G. Lynn, C. L. Marquardt, S. K. Searles, and B. J. Feldman, "Design and Performance of a High-Average-Power, Diode-Pumped 2.1 μm Tm,Ho:YAG Laser," presented at Advanced Solid-State Lasers, New Orleans, LA, 1993.

[44] M. G. Jani, N. P. Barnes, C. B. Murray, D. W. Hart, G. J. Quarles, and V. K. Castillo, "Diode-pumped Ho:Tm:$LuLiF_4$ laser at room temperature," *IEEE Journal of Quantum Electronics*, vol. 33, pp. 112-115, 1997.

[45] J. D. Kmetec, T. S. Kubo, and T. J. Kane, "Laser performance of diode-pumped thulium-doped $Y_3Al_5O_{12}$, $(Y, Lu)_3Al_5O_{12}$ and $Lu_3Al_5O_{12}$ crystals," *Optics Letters*, vol. 19, pp. 186-188, 1994.

[46] N. P. Barnes, M. G. Jani, and R. L. Hutcheson, "Diode-pumped, room-temperature Tm:LuAG laser," *Appl. Opt.*, vol. 34, pp. 4290-4294, 1995.

[47] I. F. Elder and M. J. P. Payne, "Characterization of a CW Diode-Pumped Tm:$YAlO_3$ Laser," presented at OSA TOPS Advanced Solid-State Lasers, Memphis, TN, 1995.

[48] I. F. Elder and M. J. P. Payne, "YAP versus YAG as a diode-pumped host for thulium," *Optics Communications*, vol. 148, pp. 265-269, 1998.

[49] J. J. Zayhowski, J. Harrison, C. D. III, and J. Ochoa, "Tm:YVO_4 microchip laser," *Applied Optics*, vol. 34, pp. 435-437, 1995.

[50] C. P. Wyss, W. Luthy, H. P. Weber, V. I. Vlasov, Y. D. Zavartsev, P. A. Studenikin, A. I. Zagumennyi, and I. A. Shcherbakov, "Diode-pumped 1.4-w Tm3+: GdVO4 microchip laser at 1.9 mu m," *Ieee Journal of Quantum Electronics*, vol. 34, pp. 2380-2382, 1998.

[51] N. Coluccelli, G. Galzerano, P. Laporta, F. Cornacchia, D. Parisi, and M. Tonelli, "Tm-doped LiLuF4 crystal for efficient laser action in the wavelength range from 1.82 to 2.06 mu m," *Optics Letters*, vol. 32, pp. 2040-2042, 2007.

[52] J. M. Cano-Torres, M. D. Serrano, C. Zaldo, M. Rico, X. Mateos, J. Liu, U. Griebner, V. Petrov, F. JoseValle, M. Galan, and G. Viera, "Broadly tunable laser operation near 2 mu m in a locally disordered crystal of Tm3+-doped NaGd(WO4)(2)," *Journal of the Optical Society of America B-Optical Physics*, vol. 23, pp. 2494-2502, 2006.

[53] X. Mateos, V. Petrov, J. H. Liu, M. C. Pujol, U. Griebner, M. Aguilo, F. Diaz, M. Galan, and G. Viera, "Efficient 2-mu m continuous-wave laser oscillation of Tm3+: KLu(WO4)(2)," *Ieee Journal of Quantum Electronics*, vol. 42, pp. 1008-1015, 2006.

[54] K. H. Kim, Y. S. Choi, R. V. Hess, C. H. Blair, P. Brockman, N. P. Barnes, G. W. Henderson, and M. R. Kokta, "Experiments and Theory for a Tm:Ho:YAG Laser End Pumped by a Cr:GSAG Laser," presented at Advanced Solid-State Lasers, Salt Lake City, Utah, 1990.

[55] E. D. Filer, N. P. Barnes, F. L. Naranjo, and M. R. Kokta, "Spectroscopy and Lasing in Ho:Tm:$Lu_3Al_5O_{12}$," presented at Advanced Solid-State Lasers, New Orleans, LA, 1993.
[56] J. C. Lee and G. Han, "Alexandrite Laser Pumped Ho,Tm:YLF Laser Performance," presented at Advanced Solid-State Lasers, New Orleans, LA, 1993.
[57] E. W. Duczynski, G. Huber, V. G. Ostroumov, and I. A. Shcherbakov, "Cw Double Cross Pumping of the 5/7-5/8 Laser Transition in Ho-3+ -Doped Garnets," *Applied Physics Letters*, vol. 48, pp. 1562-1563, 1986.
[58] W. J. Rodriguez, N. P. Barnes, E. D. Filer, and F. L. Naranjo, "Laser Operation of 1.76 μm Pumped Ho:Tm:LuAG," presented at Advanced Solid-State Lasers, New Orleans, LA, 1993.
[59] W. J. Rodriguez, F. L. Naranjo, N. P. Barnes, and M. R. Kokta, "Quasi-two-level laser operation of Tm:LuAG," presented at Technical Digest of Conference on Lasers and Electro-Optics, 1994.
[60] P. B. Phua, K. S. Lai, R. F. Wu, Y. L. Lim, and E. Lau, "Room-temperature operation of a multiwatt Tm:YAG laser pumped by a 1-μm Nd:YAG laser," *Optics Letters*, vol. 25, pp. 619-621, 2000.
[61] R. C. Stoneman and L. Esterowitz, "Efficient, broadly tunable, laser-pumped Tm:YAG and Tm:YSGG cw lasers," *Optics Letters*, vol. 15, pp. 486-488, 1990.
[62] H. Saito, S. Chaddha, R. S. F. Chang, and N. Djeu, "Efficient 1.94-μm Tm^{3+} laser in YVO_4 host," *Optics Letters*, vol. 17, pp. 189-191, 1992.
[63] V. A. Mikhailov, Y. D. Zavartsev, A. I. Zagumennyi, V. G. Ostroumov, P. A. Studenikin, E. Heumann, G. Huber, and I. A. Shcherbakov, "GdVO4:Tm3+ - A new efficient medium for diode-pumped 2-mu m lasers.," *Kvantovaya Elektronika*, vol. 24, pp. 15-16, 1997.
[64] E. Sorokin, A. N. Alpatiev, I. Sorokina, A. I. Zagumennyi, and I. A. Scherbakov, "Tunable efficient continuous-wave room-temperature Tm^{3+}:$GDVO_4$ laser," presented at Advanced Solid-State Lasers, 2002.
[65] P. Camy, J. L. Doualan, S. Renard., A. Braud, V. Menard, and R. Moncorge, "Tm^{3+}:CaF_2 for 1.9 μm laser operation," *Optics Communications*, vol. 236, pp. 395-402, 2004.
[66] V. Petrov, F. Guell, J. Massons, J. Gavalda, R. M. Sole, M. Aguilo, F. Diaz, and U. Griebner, "Efficient tunable laser operation of Tm : KGd(WO4)(2) in the continuous-wave regime at room temperature," *Ieee Journal of Quantum Electronics*, vol. 40, pp. 1244-1251, 2004.
[67] S. Rivier, X. Mateos, V. Petrov, U. Griebner, Y. E. Romanyuk, C. N. Borca, F. Gardillou, and M. Pollnau, "Tm : KY(WO4)(2) waveguide laser," *Optics Express*, vol. 15, pp. 5885-5892, 2007.

[68] X. M. Han, J. M. Cano-Torres, M. Rico, C. Cascales, C. Zaldo, X. Mateos, S. Rivier, U. Griebner, and V. Petrov, "Spectroscopy and efficient laser operation near 1.95 mu m of Tm3+ in disordered NaLu(WO4)(2)," *Journal of Applied Physics*, vol. 103, pp. -, 2008.

[69] N. P. Barnes, E. D. Filer, F. L. Naranjo, W. J. Rodriguez, and M. R. Kokta, "Spectroscopic and lasing properties of Ho:Tm:Luag," *Optics Letters*, vol. 18, pp. 708-710, 1993.

[70] J. F. Pinto, L. Esterowitz, and G. H. Rosenblatt, "Continuous-Wave Mode-Locked 2-Mu-M Tm - Yag Laser," *Optics Letters*, vol. 17, pp. 731-732, 1992.

[71] F. Heine, E. Heumann, G. Huber, and K. Schepler, "CW Mode-Locking of Tm and Ho Lasers," presented at Advanced Solid-State Lasers, Santa Fe, NM, 1992.

[72] S. R. Bowman and B. J. Feldman, "Demonstration and Analysis of a holmium quasi-two-level laser," presented at SPIE Solid State Lasers III, 1992.

[73] R. C. Stoneman and L. Esterowitz, "Intracavity-pumped 2.09-μm Ho:YAG laser," *Optics Letters*, vol. 17, pp. 736-738, 1992.

[74] C. D. Nabors, J. Ochoa, T. Y. Fan, A. Sanchez, H. K. Choi, and G. W. Turner, "Ho-Yag Laser-Pumped by 1.9-Mu-M Diode-Lasers," *Ieee Journal of Quantum Electronics*, vol. 31, pp. 1603-1605, 1995.

[75] C. Bollig, R. A. Hayward, W. A. Clarkson, and D. C. Hanna, "2-W Ho : YAG laser intracavity pumped by a diode-pumped Tm : YAG laser," *Optics Letters*, vol. 23, pp. 1757-1759, 1998.

[76] M. Schellhorn, A. Hirth, and C. Kieleck, "Ho : YAG laser intracavity pumped by a diode-pumped Tm : YLF laser," *Optics Letters*, vol. 28, pp. 1933-1935, 2003.

[77] S. So, J. I. Mackenzie, D. P. Shepherd, W. A. Clarkson, J. G. Betterton, E. K. Gorton, and J. A. C. Terry, "Power-scalable Ho:YAG slab laser intracavity side-pumped by a Tm:YLF slab laser," presented at ASSP 2006: 21st Annual Conference on Advanced Solid-State Photonics (Topical Meeting and Tabletop Exhibit), Lake Tahoe, USA, 2006.

[78] S. So, J. I. Mackenzie, D. P. Shepherd, W. A. Clarkson, J. G. Betterton, E. K. Gorton, and J. A. C. Terry, "Intra-cavity side-pumped Ho : YAG laser," *Optics Express*, vol. 14, pp. 10481-10487, 2006.

[79] P. A. Budni, L. A. Pomeranz, C. A. Miller, B. K. Dygan, M. L. Lemons, and E. P. Chickles, "CW and Q-switched Ho:YAG pumped by Tm:YALO," presented at OSA Trends in Optics and Photonics on Advanced Solid State Lasers, Washington, DC, 1998.

[80] P. A. Budni, M. L. Lemons, J. R. Mosto, and E. P. Chicklis, "High-Power/High-Brightness Diode-Pumped 1.9 μm Thulium and Resonantly Pumped 2.1-μm holmium Lasers," *IEEE Journal of Selected Topics in Quantum Electronics*, vol. 6, pp. 629-635, 2000.

[81] S. So, J. I. Mackenzie, D. P. Shepherd, and W. A. Clarkson, "High-power slab-based Tm:YLF laser for in-band pumping of Ho:YAG," presented at SPIE Solid State Lasers XVII: Technology and Devices, 2008.

[82] P. A. Budni, C. R. Ibach, S. D. Setzler, E. J. Gustafson, R. T. Castro, and E. P. Chicklis, "50-mJ, Q-switched, 2.09-mu m holmium laser resonantly pumped by a diode-pumped 1.9-mu m thulium laser," *Optics Letters*, vol. 28, pp. 1016-1018, 2003.

[83] N. Sims, M. C. Cimolino, N. P. Barnes, and B. G. Asbury, "10 Hz PRF Operation and Temperature Estimation of a conductively Cooled, Room Temperature, Diode-Pumped Ho:Tm:YLF Laser," presented at Advanced Solid-State Lasers, Memphis, TN, 1995.

[84] M. G. Jani, "Diode-Pumped, Long Pulse Length Ho:Tm:$YLiF_4$ laser at 10 Hz," presented at Advanced Solid-State Lasers, Memphis, TN, 1995.

[85] V. D. Rodriguez, M. E. Storm, and N. P. Barnes, "Small Signal Gain of Ho:Tm:$YLiF_4$ at High Pump Fluences," presented at Advanced Solid-State Lasers, Memphis, TN, 1995.

[86] J. R. Yu, U. N. Singh, N. P. Barnes, and M. Petros, "125-mJ diode-pumped injection-seeded Ho : Tm : YLF laser," *Optics Letters*, vol. 23, pp. 780-782, 1998.

[87] J. R. Yu, A. Braud, and M. Petros, "600-mJ, double-pulse 2-μm laser," *Optics Letters*, vol. 28, pp. 540-542, 2003.

[88] G. Hansson, A. Callenas, and C. Nelsson, "Upconversion Studies in Laser Diode Pumped Tm,Ho:$YLiF_4$," presented at Advanced Solid-State Lasers, New Orleans, LA, 1993.

[89] J. R. Yu, B. C. Trieu, E. A. Modlin, U. N. Singh, and M. J. Kavaya, "1J/pulse Q-switched 2 μm solid-state laser," *Optics Letters*, vol. 31, pp. 462-464, 2006.

[90] C. Bollig, W. A. Clarkson, R. A. Hayward, and D. C. Hanna, "Efficient high-power Tm : YAG laser at 2 mu m, end-pumped by a diode bar," *Optics Communications*, vol. 154, pp. 35-38, 1998.

[91] E. C. Honea, R. J. Beach, S. B. Sutton, J. A. Speth, I. V. Mitchell, J. A. Skidmore, M. A. Emanuel, and S. A. Payne, "115-W Tm:YAG CW diode-pumped solid-state laser," *IEEE Journal of Quantum Electronics*, vol. 33, pp. 1592-1600, 1997.

[92] K. S. Lai, P. B. Phua, R. F. Wu, Y. L. Lim, E. Lau, S. W. Toh, B. T. Toh, and A. Chang, "120-W continuous-wave diode-pumped Tm:YAG laser," *Optics Letters*, vol. 25, pp. 1591-1593, 2000.

[93] N. I. Borodin, P. V. Kryukov, A. Popov, S. N. Ushakov, and A. Shestakov, "Diode-pumped cw Tm3+ : YAlO3 laser," *Quantum Electronics*, vol. 35, pp. 511-514, 2005.

[94] L. A. Pomeranz, P. A. Budni, M. L. Lemons, C. A. Miller, J. R. Mosto, T. M. Pollak, and E. P. Chicklis, "Power Scaling Performence of Tm:YLF and Tm:YALO

Lasers," presented at OSA Trends in Optics and Photonics on Advanced Solid State Lasers, 1999.
[95] A. Dergachev, K. Wall, and P. F. Moulton, "A CW Side-Pumped Tm:YLF Laser," presented at OSA TOPS Advanced Solid State Lasers, 2002.
[96] A. C. Sullivan, G. J. Wagner, D. Gwin, R. C. Stoneman, and A. I. R. Malm, "High power Q-switched Tm:$YAlO_3$ lasers," presented at Technical Digest of Advanced Solid State Photonics, Santa Fe, New Mexico, 2005.
[97] H. Kalaycioglu and A. Sennaroglu, "Low-threshold continuous-wave Tm^{3+}:$YAlO_3$ laser," *Opt. Commun.*, vol. 281, pp. 4071-4074, 2008.
[98] Y. F. Li, Y. L. Ju, B. Q. Yao, Y. Z. Wang, and S. Ubizskii, "A laser-diode-pumped widely tunable single-longitude-mode Tm : YAP laser at room temperature," *Chinese Physics Letters*, vol. 24, pp. 2594-2596, 2007.
[99] J. A. Curcio and C. C. Petty, "The Near Infrared Absorption Spectrum of Liquid Water," *Journal of the Optical Society of America*, vol. 41, pp. 302-304, 1951.
[100] B. Jean and T. Bende, "Mid-IR laser applications in medicine," *Solid-State Mid-Infrared Laser Sources*, vol. 89, pp. 511-544, 2003.
[101] H. O. Teichmann, T. R. Herrmann, and T. Bach, "Technical aspects of lasers in urology," *World Journal of Urology*, vol. 25, pp. 221-225, 2007.
[102] N. S. Nishioka and Y. Domankevitz, "Comparison of Tissue Ablation with Pulsed Holmium and Thulium Lasers," *IEEE Journal of Quantum Electronics*, vol. 26, pp. 2271-2275, 1990.
[103] M. R. Treat, S. L. Trokel, R. D. Reynolds, V. J. Defilippi, J. Andrew, J. Y. Liu, and M. G. Cohen, "Preliminary Evaluation of a Pulsed 2.15-Mu-M Laser System for Fiberoptic Endoscopic Surgery," *Lasers in Surgery and Medicine*, vol. 8, pp. 322-326, 1988.
[104] N. M. Fried, "Therapeutic applications of lasers in urology: an update," *Expert Review of Medical Devices*, vol. 3, pp. 81-94, 2006.
[105] A. H. H. Tan and P. J. Gilling, "Holmium laser prostatectomy: Current techniques," *Urology*, vol. 60, pp. 152-156, 2002.
[106] R. L. Kuo, R. F. Paterson, S. C. Kim, T. M. Siqueira Jr., M. M. Elhilali, and J. E. Lingeman, "Holmium laser enucleation of the prostate (HoLEP): A Technical Update," *World Journal of Surgical Oncology*, vol. 1, 2003.
[107] R. Tooher, P. Sutherland, A. Costello, P. Gilling, G. Rees, and G. Maddern, "A systematic review of holmium laser prostatectomy for benign prostatic hyperplasia," *Journal of Urology*, vol. 171, pp. 1773-1781, 2004.
[108] A. J. Costello, M. J. Westcott, and J. S. Peters, "Experience with the holmium laser as an endoscopic lithotrite," *Australian and New Zealand Journal of Surgery*, vol. 70, pp. 348-350, 2000.

[109] K. F. Chan, G. J. Vassar, T. J. Pfefer, J. W. H. Teichman, R. D. Glickman, S. T. Weintraub, and A. J. Welch, "Holmium : YAG laser lithotripsy: A dominant photothermal ablative mechanism with chemical decomposition of urinary calculi," *Lasers in Surgery and Medicine*, vol. 25, pp. 22-37, 1999.
[110] J. Helfmann and G. Müller, "Laser Lithotripsy: Process and Overview," *Medical Laser Application*, vol. 16, pp. 30-37, 2001.
[111] S. A. Pierre and D. M. Albala, "The future of lasers in urology," *World Journal of Urology*, vol. 25, pp. 275-283, 2007.
[112] T. Bach, T. R. W. Herrmann, R. Ganzer, M. Burchardt, and A. J. Gross, "RevoLix (TM) vaporesection of the prostate: initial results of 54 patients with a 1-year follow-up," *World Journal of Urology*, vol. 25, pp. 257-262, 2007.
[113] N. M. Fried and K. E. Murray, "New technologies in endourology - High-power thulium fiber laser ablation of urinary tissues at 1.94 mu m," *Journal of Endourology*, vol. 19, pp. 25-31, 2005.
[114] T. Bach, T. R. W. Herrmann, C. Cellarius, and A. J. Gross, "Bladder neck incision using a 70 W 2 micron continuous wave laser (RevoLix)," *World Journal of Urology*, vol. 25, pp. 263-267, 2007.
[115] G. Wendt-Nordahl, S. Huckele, P. Honeck, P. Alken, T. Knoll, M. S. Michel, and A. Hacker, "Systematic Evaluation of a Recently Introduced 2−µm Continuous-Wave Thulium Laser for Vaporesection of the Prostate," *Journal of Endourology*, vol. 22, pp. 1041-1045, 2008.
[116] N. M. Fried, "High-power laser vaporization of the canine prostate using a 110 W thulium fiber laser at 1.91 mu m," *Lasers in Surgery and Medicine*, vol. 36, pp. 52-56, 2005.
[117] T. J. Carrig, A. K. Hankla, G. J. Wagner, C. B. Rawle, and I. T. M. Kinnie, "Tunable infrared laser sources for DIAL," presented at SPIE Laser Radar Technology and Applications VII, 2002.
[118] T. J. Carrig, "Novel Pulsed Solid-State Sources for Laser Remote Sensing," presented at SPIE Solid State Laser Technologies and Femtosecond Phenomena, Bellingham, WA, 2004.
[119] R. Targ, M. J. Kavaya, R. M. Huffaker, and R. L. Bowles, "Coherent Lidar Airborne Windshear Sensor - Performance Evaluation," *Applied Optics*, vol. 30, pp. 2013-2026, 1991.
[120] J. Bösenberg, "Ground-based differential absorption lidar for water-vapor and temperature profiling," *Applied Optics*, vol. 37, pp. 3845-3860, 1998.
[121] A. Godard, "Infrared (2-12 µm) solid-state laser sources: a review," *C. R. Physique*, vol. 8, pp. 1100-1128, 2007.

[122] S. Cha, N. Sugimoto, K. F. Chan, and D. K. Killinger, "Tunable 2.1-μm Ho laser for DIAL remote sensing of atmospheric water vapor," presented at OSA Advanced Solid State Lasers, 1990.
[123] S. W. Henderson, C. P. Hale, J. R. Magee, M. J. Kavaya, and A. V. Huffaker, "Eye-Safe Coherent Laser-Radar System at 2.1-Mu-M Using Tm,Ho-Yag Lasers," *Optics Letters*, vol. 16, pp. 773-775, 1991.
[124] M. J. Kavaya, S. W. Henderson, E. C. Russell, R. M. Huffaker, and R. G. Frehlich, "Monte-Carlo Computer-Simulations of Ground-Based and Space-Based Coherent Dial Water-Vapor Profiling," *Applied Optics*, vol. 28, pp. 840-851, 1989.
[125] M. G. Jani, N. P. Barnes, and K. E. Murray, "Long Pulselength Two Micrometer Lasers for LAWS Application," presented at Advanced Solid-State Lasers, New Orleans, LA, 1993.
[126] S. W. Henderson, C. P. Hale, and J. R. Magee, "Injection-Seeded Operation of a Q-Switched Cr,Tm,Ho:YAG Laser," presented at Advanced Solid-State Lasers, Salt Lake City, Utah, 1990.
[127] K. Scholle, E. Heumann, and G. Huber, "Single mode Tm and Tm,Ho:LuAG lasers for LIDAR applications," *Laser Physics Letters*, vol. 1, pp. 285-290, 2004.
[128] H. Jelinkova, P. Koranda, M. E. Doroshenko, T. T. Basiev, J. Sulc, M. Nemec, P. Cerny, V. K. Komar, and M. B. Kosmyna, "Cr2+: ZnSe laser pumped by 1.66 mu m or 1.97 mu m radiations," *Laser Physics Letters*, vol. 4, pp. 23-29, 2007.
[129] U. Demirbas and A. Sennaroglu, "Intracavity-pumped Cr^{2+}: ZnSe laser with ultrabroad tuning range between 1880 and 3100 nm," *Optics Letters*, vol. 31, pp. 2293-2295, 2006.
[130] G. J. Wagner, T. J. Carrig, R. H. Page, K. I. Schaffers, J. Ndap, X. Ma, and A. Burger, "Continuous-wave broadly tunable Cr^{2+}:ZnSe laser," *Optics Letters*, vol. 24, pp. 19-21, 1999.
[131] P. A. Budni, L. A. Pomeranz, M. L. Lemons, C. A. Miller, J. R. Mosto, and E. P. Chicklis, "Efficient mid-infrared laser using 1.9-μm pumped Ho:YAG and $ZnGeP_2$ optical parametric oscillators," *J. Opt. Soc. Amer. B*, vol. 17, pp. 723-728, 2000.
[132] E. Lippert, S. Nicolas, G. Arisholm, K. Stenersen, and G. Rustad, "Midinfrared laser source with high power and beam quality," *Applied Optics*, vol. 45, pp. 3839-3845, 2006.
[133] L. A. Pomeranz, P. A. Ketteridge, P. A. Budni, K. M. Ezzo, D. M. Rines, and E. P. Chicklis, "Tm:$YALO_3$ Laser Pumped ZGP Mid-IR Source," presented at OSA TOPS on Advanced Solid-State Photonics, 2003.
[134] M. Eichhorn and A. Hirth, "Electro-Optically Q-switched Tm:YAG Laser Pumped ZGP Optical-Parametric Oscillator," presented at Conference on Lasers and Electro-Optics CLEO, San Jose, CA, 2008.

[135] C. Kieleck, M. Eichhorn, A. Hirth, D. Faye, and E. Lallier, "20-50 kHz Mid-Infrared OP-GaAs OPO," presented at Conference on Lasers and Electro-Optics CLEO, San Jose, CA, 2008.
[136] G. J. Wagner, T. J. Carrig, R. H. Jarman, R. H. Page, K. I. Schaffers, J.-O. Ndap, X. Ma, and A. Burger, "High-efficiency, broadly-tunable continuous-wave Cr^{2+}:ZnSe laser," presented at Advanced Solid State Photonics, Boston, 1999.
[137] V. Sudesh and E. M. Goldys, "Spectroscopic properties of thulium-doped crystalline materials including a novel host, La2Be2O5: a comparative study," *Journal of the Optical Society of America B-Optical Physics*, vol. 17, pp. 1068-1076, 2000.
[138] J. M. O'Hare, "Crystal-field determination for trivalent thulium in yttrium orthoaluminate," *Phys. Rev. B*, vol. 14, pp. 3732-3743, 1976.
[139] M. J. Weber, T. E. Varitimos, and B. H. Matsinger, "Optical Intensities of Rare-Earth Ions in Yttrium Orthoaluminate," *Physical Review B*, vol. 8, pp. 47-53, 1973.
[140] H. Ni and S. C. Rand, "Avalanche Upconversion in Tm-Yalo3," *Optics Letters*, vol. 16, pp. 1424-1426, 1991.
[141] I. F. Elder and J. Payne, "Diode-pumped, room-temperature Tm:YAP laser," *Applied Optics*, vol. 36, pp. 8606-8610, 1997.
[142] T. Thevar and N. P. Barnes, "Diode-pumped, continuous-wave Tm : YAlO3 laser," *Applied Optics*, vol. 45, pp. 3352-3355, 2006.
[143] P. Cerny and D. Burns, "Modeling and experimental investigation of a diode-pumped Tm : YA1O(3) Laser with a- and b-cut crystal orientations," *Ieee Journal of Selected Topics in Quantum Electronics*, vol. 11, pp. 674-681, 2005.
[144] P. Cerny, J. Sulc, and H. Jelinkova, "Continously tunable diode-pumped Tm:YAP laser," presented at SPIE Solid State Lasers and Amplifiers II, 2006.
[145] P. Cerny, G. J. Valentine, and D. Burns, "Actively stabilised diode pumped Tm : YAIO laser," *Electronics Letters*, vol. 40, pp. 1061-1063, 2004.
[146] O. A. Buryy, D. Y. Sugak, S. B. Ubizskii, I. I. Izhnin, M. M. Vakiv, and I. M. Solskii, "The comparative analysis and optimization of the free-running Tm3+: YAP and Tm3+: YAG microlasers," *Applied Physics B-Lasers and Optics*, vol. 88, pp. 433-442, 2007.
[147] I. Razdobreev and A. Shestakov, "Self-pulsing of a monolithic Tm-doped YAlO3 microlaser," *Physical Review A*, vol. 73, pp. -, 2006.
[148] H. Kalaycioglu, A. Sennaroglu, and A. Kurt, "Influence of Doping Concentration on the Power Performance of Diode-Pumped Continuous-Wave Tm^{3+}:$YAlO_3$ Lasers," *IEEE Journal of Selected Topics in Quantum Electronics*, vol. 11, pp. 667-673, 2005.
[149] G. J. Kintz, "Highly Efficient CW 2μ Laser," presented at Lasers and Electro-Optics Society Annual Meeting, 1990.

[150] S. A. Payne, L. L. Chase, L. K. Smith, W. L. Kway, and W. F. Krupke, "Infrared Cross-Section Measurements for Crystals Doped with Er^{3+}, Tm^{3+}, and Ho^{3+}," *IEEE Journal of Quantum Electronics*, vol. QE-28, pp. 2619-2630, 1992.
[151] D. N. Nikogosyan, *Properties of Optical and Laser-Related Materials - A Handbook*, First ed: John Wiley & Sons Ltd., 1997.
[152] A. Sennaroglu, A. Kurt, and G. Özen, "Effect of cross relaxation on the 1470 and 1800 nm emissions in Tm^{3+}:TeO_2-$CdCl_2$ glass," *Journal of Physics: Condensed Matter*, vol. 16, pp. 2471-2478, 2004.
[153] A. K. Cousins, "Temperature and thermal stress scaling in finite-length end-pumped laser rods," *IEEE J. Quantum Electron.*, vol. 28, pp. 1057-1069, 1992.
[154] A. Sennaroglu, "Continuous wave thermal loading in saturable absorbers: theory and experiment," *Appl. Opt.*, vol. 36, pp. 9528-9535, 1997.
[155] A. Sennaroglu, "Analysis and optimization of lifetime thermal loading in continuous-wave Cr^{4+} doped solid-state lasers," *J. Opt. Soc. Amer. B*, vol. 18, pp. 1578-1586, 2001.
[156] K. Read, F. Blonigen, N. Riccelli, M. M. Murnane, and H. C. Kapteyn, "Low-threshold operation of an ultrashort-pulse mode-locked Ti:sapphire laser," *Optics Letters*, vol. 21, pp. 489-491, 1996.
[157] A. J. Tiffany, I. T. McKinnie, and D. M. Warrington, "Low-threshold, single-frequency, coupled cavity Ti:sapphire laser," *Applied Optics*, vol. 36, pp. 4989-4992, 1997.
[158] A. Agnesi, Piccinini, E., Reali, G., "Threshold optimization of all-solid-state Cr:forsterite lasers," *JOSA B*, vol. 17, 2000.
[159] A. Sennaroglu, "Analysis and optimization of lifetime thermal loading in continuous-wave Cr^{4+}-doped solid-state lasers," *Journal of Optical Society of America B*, vol. 18, pp. 1578-1586, 2001.
[160] M. Kowalevicz, T. R. Schibli, F. X. Kartner, and T. G. Fujimoto, "Ultralow-threshold Kerr-lens mode-locked Ti:Al2O3 laser," *Optics Letters*, vol. 27, pp. 2037-2039, 2002.
[161] W. Ling, Y. Jia, J. Sun, Z. Wang, and Z. Wei, "Low-threshold self-starting femtosecond Ti:sapphire laser," *Applied Optics*, vol. 45, pp. 2495-2498, 2006.
[162] A. Sennaroglu, F. X. Kaertner, and J. G. Fujimoto, "Low-threshold, room-temperature femtosecond Cr^{4+}:forsterite laser," *Optics Express*, vol. 15, pp. 13043-13048, 2007.
[163] M. Talmor, C. B. Bleustein, and D. P. Poppas, "Laser tissue welding: a biotechnological advance for the future," *Arch Facial Plast Surg.*, vol. 3, pp. 207-213, 2001.

[164] T. S. Flock and K. S. Marchitto, "Progress Towards Seamless Tissue Fusion for Wound Closure," *Otolaryngologic Clinics of North America*, vol. 38, pp. 295-305, 2005.
[165] D. P. Poppas and D. S. Scherr, "Laser tissue welding: a urological surgeon's perspective," *Hemophilia*, vol. 4, pp. 456-462, 1998.
[166] K. Jain and W. Gorisch, "Repair of small blood vessels with the neodymium-YAG laser: a preliminary report.," *Surgery*, vol. 85, pp. 684-688., 1979.
[167] N. M. Fried and J. T. Walsh, "Laser skin welding: In vivo tensile strength and wound healing results," *Lasers in Surgery and Medicine*, vol. 27, pp. 55-65, 2000.
[168] D. P. Poppas, S. M. Schlossberg, I. L. Richmond, D. A. Gilbert, and C. J. Devine, "Laser-Welding in Urethral Surgery - Improved Results with a Protein Solder," *Journal of Urology*, vol. 139, pp. 415-417, 1988.
[169] B. Lobel, O. Eyal, N. Kariv, and A. Katzir, "Temperature controlled CO2 laser welding of soft tissues: Urinary bladder welding in different animal models (rats, rabbits, and cats)," *Lasers in Surgery and Medicine*, vol. 26, pp. 4-12, 2000.
[170] I. Cilesiz, S. Thomsen, and A. J. Welch, "Controlled temperature tissue fusion: Argon laser welding of rat intestine in vivo .1.," *Lasers in Surgery and Medicine*, vol. 21, pp. 269-277, 1997.
[171] M. C. Oz, L. S. Bass, H. W. Popp, R. S. Chuck, J. P. Johnson, S. L. Trokel, and M. R. Treat, "Invitro Comparison of Thulium-Holmium-Chromium - Yag and Argon Ion Lasers for Welding of Biliary Tissue," *Lasers in Surgery and Medicine*, vol. 9, pp. 248-253, 1989.
[172] I. Cilesiz, S. Thomsen, A. J. Welch, and E. K. Chan, "Controlled temperature tissue fusion: Ho:YAG laser welding of rat intestine in vivo .2.," *Lasers in Surgery and Medicine*, vol. 21, pp. 278-286, 1997.
[173] B. Ott, B. J. Zuger, D. Erni, A. Banic, T. Schaffner, H. P. Weber, and M. Frenz, "Comparative in vitro study of tissue welding using a 808 nm diode laser and a Ho : YAG laser," *Lasers in Medical Science*, vol. 16, pp. 260-266, 2001.
[174] H. W. Popp, M. C. Oz, L. S. Bass, R. S. Chuck, S. L. Trokel, and M. R. Treat, "Welding of Gallbladder Tissue with a Pulsed 2.15 Mu-M Thulium-Holmium-Chromium - Yag Laser," *Lasers in Surgery and Medicine*, vol. 9, pp. 155-159, 1989.
[175] L. Newman, "Laser welding research looks to eliminate sutures," *Urology Times*, vol. 23, pp. 7, 1995.
[176] N. M. Fried and J. T. Walsh, "Cryogen spray cooling during laser tissue welding," *Physics in Medicine and Biology*, vol. 45, pp. 753-763, 2000.
[177] G. Noguera, W. S. Lee, J. Castro-Combs, R. S. Chuck, B. Soltz, R. Soltz, and A. Behrens, "Novel laser-activated solder for sealing corneal wounds," *Investigative Ophthalmology & Visual Science*, vol. 48, pp. 1038-1042, 2007.

[178] R. B. Stewart, A. Benbrahim, G. M. LaMuraglia, M. Rosenberg, G. J. LItalien, W. M. Abbott, and R. T. V. Kung, "Laser assisted vascular welding with real time temperature control," *Lasers in Surgery and Medicine*, vol. 19, pp. 9-16, 1996.
[179] I. Cilesiz, T. Springer, S. Thomsen, and A. J. Welch, "Controlled temperature tissue fusion: Argon laser welding of canine intestine in vitro," *Lasers in Surgery and Medicine*, vol. 18, pp. 325-334, 1996.
[180] H. A. Green, E. E. Burd, N. S. Nishioka, and C. C. Compton, "Skin graft take and healing following 193-nm excimer, continuous-wave carbon dioxide (CO2), pulsed CO2, or pulsed holmium: YAG laser ablation of the graft bed," *Archives of Dermatology*, vol. 129, pp. 979-988, 1993.
[181] N. M. Fried and J. T. Walsh, "Dye-assisted laser skin closure with pulsed radiation: an in-vitro study of weld strength and thermal damage.," *Journal of Biomedical Optics*, vol. 3, pp. 401-408, 1998.
[182] T. Bilici, H. Kalaycioglu, O. Tabakoglu, A. Kurt, A. Sennaroglu, and M. Gulsoy, "Design of Tm:YAP Laser System for Medical Applications," presented at 13. National Conference on Biomedical Engineering, (Biomut 2008), Ankara, Turkey, 2008.
[183] T. Bilici, O. Tabakoglu, H. Kalaycioglu, A. Kurt, A. Sennaroglu, and M. Gulsoy, "Laser Tissue Welding at 1980-nm," presented at 13. National Conference on Biomedical Engineering, (Biomut 2008), Ankara, Turkey, 2008.
[184] T. Bilici, "Tm:YAP laser system preliminary results by liver, heart, kidney, and brain," Bogazici University, Istanbul 17 January 2007 2007.
[185] J. H. V. Vleck, "The puzzle of rare-earth spectra in solids," *Journal of Physical Chemistry*, vol. 41, pp. 67, 1936.
[186] L. J. F. Broer, C. J. Gorter, and J. Hoogschagen, "On the intensities and the multipole character in the spectra of the rare earth ions," *Physica*, vol. 11, pp. 231, 1945.
[187] A. A. Kaminskii, "Chapter 4," in *Laser Crystals*, D. L. MacAdam, Ed. Berlin: Springer-Verlag, 1990.
[188] B. M. Walsh, N. P. Barnes, and B. D. Bartolo, "Branching ratios, cross sections, and radiative lifetimes of rare earth ions in solids: Application to Tm^{3+} and Ho^{3+} ions in $LiYF_4$," *J. Appl. Phys.*, vol. 83, pp. 2772-2787, 1998.
[189] W. T. Carnall, P. R. Fields, and K. Rajnak, "Spectral intensities of the trivalent lanthanides and actinides in solution II. Pm^{3+}, Sm^{3+}, Eu^{3+}, Gd^{3+},Tb^{3+}, Dy^{3+}, and Ho^{3+}," *The Journal of Chemical Physics*, vol. 49, pp. 4412-4423, 1968.
[190] B. R. Judd, "Optical Absorption Intensities of Rare-Earth Ions," *Physical Review*, vol. 127, pp. 750-761, 1962.
[191] G. S. Ofelt, "Intensities of crystal spectra of rare-earth ions," *The Journal of Chemical Physics*, vol. 37, pp. 511, 1962.

[192] P. C. Mehta and S. P. Tandon, "Spectral intensities of some Nd^{3+} β–diketonates," *Journal of Chemical Physics*, vol. 53, pp. 414, 1970.
[193] L. D. DeLoach, R. H. Page, G. D. Wilke, S. A. Payne, and W. F. Krupke, "Transition Metal-Doped Zinc Chalcogenides Spectroscopy and Laser Demonstration of a New Class of Gain Media," *IEEE Journal of Quantum Electronics*, vol. 32, pp. 885-895, 1996.
[194] A. J. Bayramian, C. D. Marshall, K. I. Schaffers, and S. A. Payne, "Characterization of Yb3+: Sr5-xBax(PO4)(3)F crystals for diode-pumped lasers," *Ieee Journal of Quantum Electronics*, vol. 35, pp. 665-674, 1999.
[195] P. F. Moulton, "Spectroscopic and Laser Characteristics of Ti-Al2O3," *Journal of the Optical Society of America B-Optical Physics*, vol. 3, pp. 125-133, 1986.
[196] M. J. Weber, "Luminescence Decay by Energy Migration and Transfer: Observation of Diffusion-Limited Relaxation," *Physical Review B*, vol. 4, pp. 2932-2939, 1971.
[197] M. Yokota and O. Tanimoto, "Effects of Diffusion on Energy Transfer by Resonance," *Journal of the Physical Society of Japan*, vol. 22, pp. 779-784, 1967.
[198] E. D. Filer, N. P. Barnes, and C. A. Morrison, "Theoretical Temperature-Dependent Branching Ratios and Laser Thresholds of the $^3F_4$ to $^3H_6$ Levels of Tm^{3+} in ten Garnets," presented at OSA TOPS Advanced Solid-State Lasers, 1991.
[199] H. Kalaycioglu, A. Sennaroglu, A. Kurt, and G. Ozen, "Spectroscopic analysis of Tm3+: LuAG," *Journal of Physics: Condensed Matter*, vol. 19, pp. -, 2007.
[200] W. F. Krupke, "Radiative Transition Probabilities Within the $4f^3$ Ground Configuration of Nd:YAG," *IEEE Journal of Quantum Electronics*, vol. QE-7, pp. 153-159, 1971.
[201] A. Sennaroglu, I. Kabalci, A. Kurt, U. Demirbas, and G. Ozen, "Spectroscopic properties of Tm^{3+}:TeO_2-PbF_2 glasses," *Journal of Luminescence*, vol. 116, pp. 79-86, 2006.
[202] Y. S. Han, J. Heo, and Y. B. Shin, "Cross relaxation mechanism among Tm3+ ions in Ge30Ga2As6S62 glass," *Journal of Non-Crystalline Solids*, vol. 316, pp. 302-308, 2003.
[203] M. Yamane and Y. Asahara, *Glasses for Photonics*, First ed. Cambridge: Cambridge University Press, 2000.
[204] J. S. Wang, E. M. Vogel, and E. Snitzer, "Tellurite glass: a new candidate for fiber devices," *Optical Materials*, vol. 3, pp. 187-203, 1994.
[205] J. S. Wang, E. Snitzer, E. M. Vogel, and J. G.H. Sigel, "1.47, 1.88, and 2.8 μm emission of Tm^{3+} and Tm^{3+}-Ho^{3+} -codoped tellurite glasses," *Journal of Luminescence*, vol. 60-61, pp. 145-149, 1994.
[206] M. Naftaly, S. X. Shen, and A. Jha, "Tm3+-doped tellurite glass for a broadband amplifier at 1.47 mu m," *Applied Optics*, vol. 39, pp. 4979-4984, 2000.

[207] D. B. Hollis, F. R. Cruickshank, and M. J. P. Payne, "Structural influence of tellurite glasses on fluorescence of thulium near 1.86μm," *J. Non-Cryst. Solids*, vol. 293-295, pp. 422-429, 2001.

[208] M. R. Ozalp, G. Ozen, A. Sennaroglu, and A. Kurt, "Stimulated and spontaneous emission probabilities of Tm^{3+} in TeO_2-$CdCl_2$ glass: the role of the local structure," *Optics Communications*, vol. 217, pp. 281-289, 2002.

[209] G. Ozen, A. Aydinli, S. Cenk, and A. Sennaroglu, "Effect of composition on the spontaneous emission probabilities, stimulated emission cross-sections and local environment of Tm3+ in TeO2-WO3 glass," *Journal of Luminescence*, vol. 101, pp. 293-306, 2003.

[210] E. R. Taylor, L. N. Ng, N. P. Sessions, and H. Buerger, "Spectroscopy of Tm^{3+} - doped tellurite glasses for 1470 nm fiber amplifier," *Journal of Applied Physics*, vol. 92, pp. 112-117, 2002.

[211] H. Kalaycioglu, H. Cankaya, N. M. Cizmeciyan, A. Sennaroglu, and G. Ozen, "Spectroscopic Investigation of Tm^{3+}:TeO_2-WO_3 glass," *Jorunal of Luminescence*, vol. 128, pp. 1501-1506, 2008.

[212] M. L. Ovecoglu, G. Ozen, B. Demirata, and A. Genc, "Microstructural characterization and crystallization kinetics of (1-x)TeO_2-xLiCl (x=0.6-0.4 mol) glasses," *Journal of the European Ceramic Society*, vol. 21, pp. 177-183, 2001.

[213] E. Snitzer, "Optical Maser Action of Nd^{+3} in A Barium Crown Glass," *Physical Review Letters*, vol. 7, pp. 444-446, 1961.

[214] M. J. Weber, J. D. Myers, and D. H. Blackburn, "Optical-Properties of Nd-3+ in Tellurite and Phosphotellurite Glasses," *Journal of Applied Physics*, vol. 52, pp. 2944-2949, 1981.

[215] B. Richards, Y. Tsang, D. Binks, J. Lousteau, and A. Jha, "Efficient ~2 μm Tm3+-doped tellurite fiber laser," *Optics Letters*, vol. 33, pp. 402-404, 2008.

[216] H. Kalaycioglu, H. Cankaya, G. Ozen, M. L. Ovecoglu, and A. Sennaroglu, "Lasing at 1065 nm in bulk Nd^{3+}-doped telluride-tungstate glass," *Opt. Commun.*, vol. (in press), 2008.

[217] R. R. Petrin, M. L. Kliewer, J. T. Beasley, R. C. Powell, I. D. Aggarwal, and R. C. Ginther, "Spectroscopy and Laser Operation of Nd-Zban Glass," *IEEE Journal of Quantum Electronics*, vol. 27, pp. 1031-1038, 1991.

[218] A. S. S. De Camargo, C. Jacinto, T. Catunda, and L. A. O. Nunes, "Auger upconversion energy transfer losses and efficient 1.06 mu m laser emission in Nd3+ supercript stop doped fluoroindogallate glass," *Applied Physics B-Lasers and Optics*, vol. 83, pp. 565-569, 2006.

[219] T. Schweizer, D. W. Hewak, D. N. Payne, T. Jensen, and G. Huber, "Rare-earth doped chalcogenide glass laser," *Electronics Letters*, vol. 32, pp. 666-667, 1996.

[220] D. F. De Sousa, L. A. O. Nunes, J. H. Rohling, and M. L. Baesso, "Laser emission at 1077 nm in Nd3+-doped calcium aluminosilicate glass," *Applied Physics B-Lasers and Optics*, vol. 77, pp. 59-63, 2003.
[221] J. Fernandez, I. Iparraguirre, R. Balda, J. Azkargorta, M. Voda, and J. M. Fernandez-Navarro, "Laser action and upconversion of Nd3+ in lead-niobium-germanate bulk glass," *Optical Materials*, vol. 25, pp. 185-191, 2004.
[222] J. C. Michel, D. Morin, and F. Auzel, "Proprietes spectroscopiques et effet laser d'un verre tellurite et d'un verre phosphate fortement dopes en neodyme," *Rev. Phys. Appl.*, vol. 13, pp. 859-866, 1978.
[223] N. Lei, B. Xu, and Z. H. Jiang, "Ti:sapphire laser pumped Nd:tellurite glass laser," *Optics Communications*, vol. 127, pp. 263-265, 1996.
[224] I. Iparraguirre, J. Azkargorta, J. M. Fernandez-Navarro, M. Al-Saleh, J. Fernandez, and R. Balda, "Laser action and upconversion of Nd3+ in tellurite bulk glass," *Journal of Non-Crystalline Solids*, vol. 353, pp. 990-992, 2007.
[225] J. S. Wang, D. P. Machewirth, F. Wu, E. Snitzer, and E. M. Vogel, "Neodymium-Doped Tellurite Single-Mode Fiber Laser," *Optics Letters*, vol. 19, pp. 1448-1449, 1994.
[226] A. Mori, Y. Ohishi, and S. Sudo, "Erbium-doped tellurite glass fibre laser and amplifier," *Electronics Letters*, vol. 33, pp. 863-864, 1997.
[227] B. Richards, S. X. Shen, A. Jha, Y. Tsang, and D. Binks, "Infrared emission and energy transfer in Tm3+, Tm3+-Ho3+ and Tm3+-Yb3+-doped tellurite fibre," *Optics Express*, vol. 15, pp. 6546-6551, 2007.
[228] Z. H. Jiang, J. H. Yang, and S. X. Dai, "Optical spectroscopy and gain properties of Nd3+-doped oxide glasses," *Journal of the Optical Society of America B-Optical Physics*, vol. 21, pp. 739-743, 2004.
[229] K. U. Kumar, V. A. Prathyusha, P. Babu, C. K. Jayasankar, A. S. Joshi, A. Speghini, and M. Bettinelli, "Fluorescence properties of Nd3+-doped tellurite glasses," *Spectrochimica Acta Part a-Molecular and Biomolecular Spectroscopy*, vol. 67, pp. 702-708, 2007.